

# High Strain Rate Mechanical Characterization of Trabecular Bone Utilizing the Split-Hopkinson Pressure Bar Technique

by

Timothy Paul Mahal Johnson

Bachelor of Science in Mechanical Engineering  
University of California - Berkeley (2003)

Submitted to the Department of Mechanical Engineering  
in partial fulfillment of the requirements for the degree of

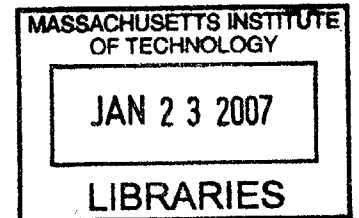
MASTER OF SCIENCE IN MECHANICAL ENGINEERING

at the

MASSACHUSETTS INSTITUTE OF TECHNOLOGY

September 2005

© 2005 Massachusetts Institute of Technology  
All Rights Reserved



The author hereby grants to Massachusetts Institute of Technology permission to reproduce and to distribute copies of this thesis document in whole or in part.

Signature of Author .....

.....  
Department of Mechanical Engineering  
19 August 2005

Certified by .....

.....  
Simona Socrate  
Assistant Professor of Mechanical Engineering  
Thesis Supervisor

Accepted by .....

.....  
Rohan Abeyaratne  
Chairman, Department Committee on Graduate Students

**BARKER**



# High Strain Rate Mechanical Characterization of Trabecular Bone Utilizing the Split-Hopkinson Pressure Bar Technique

by

Timothy Paul Mahal Johnson

Submitted to the Department of Mechanical Engineering  
on 19 August 2005, in partial fulfillment of the  
requirements for the degree of  
MASTER OF SCIENCE IN MECHANICAL ENGINEERING

## Abstract

The split-Hopkinson pressure bar (SHPB) technique has been in use in one form or another for more than fifty years and has recently gained a great deal of attention for its ability to characterize materials such as metals, plastics, and even stiff foams at strain rates of up to  $10^5 \text{ sec}^{-1}$ . Historically, however, numerous obstacles have stood in the way of applying this technique to softer biological tissues. This study is aimed at bridging this gap by employing various innovations in the field of split-Hopkinson pressure bar techniques (including hollow aluminum and solid polymeric pressure bars) to the characterization of trabecular bone. A preliminary study is conducted on a polyurea (PU) blend to assess the advantages and shortcomings of these approaches, as well as to validate the results obtained with each. Bovine trabecular bone with marrow in-situ, which was chosen for its ability to be tested with a wide spectrum of techniques, is then characterized with the selected techniques at rates of up to  $1300 \text{ s}^{-1}$  and strains of 0.07. The results are presented for each technique in the form of engineering stress vs. engineering strain curves. Average trend curves are also provided. Unfortunately, many of the samples were too damaged to allow for accurate measurement of apparent density. Consequently, a study into the effect of density on high strain rate responses is left as future work. Recommendations are made for increasing the strain imposed on the samples and suggestions for future studies on both trabecular bone and softer biological tissues are put forward.

Thesis Supervisor: Simona Socrate

Title: Assistant Professor of Mechanical Engineering





## Acknowledgements

First and foremost I would like to thank my advisor, Professor Simona Socrate, for her unwavering support and guidance over the last two years. I am continually awed by her commitment to both the field of engineering and the development of her students. In an environment as competitive and driven as MIT's, it is refreshing to find a professor who genuinely cares. I am extremely grateful for her continued support and insightful guidance. I can only hope that this work provides a reasonable return on her investment in me.

I would also like to express my gratitude to Dr. Sai Sarva, whose commitment to excellence, invaluable experimental insights, and long hours in the basement of NE-47 enabled me to complete this ambitious study and laid the foundations for what I hope will be a long and enduring friendship. Similarly, I would like to thank Adam Mulliken, of the Institute for Soldier Nanotechnologies (ISN), and Kristin Myers, Anastassia Paskaleva, Asha Balakrishnan, Petch Jearanaisilawong, and Michael King of the Mechanics and Materials group for patiently answering my questions and making sure I got the most out of my time at MIT.

I am also greatly indebted to both the DuPont-MIT Alliance and the Institute for Soldier Nanotechnologies for their generous financial support. Receiving the DuPont Fellowship was a wonderful opportunity to explore my interest without being asked for anything in return, and working within the framework of ISN's generous financial support and world class research facility was truly a unique and rememberable experience.

I would also like to offer my gratitude to Dr. Ron Alkalay and Mr. John Muller of the Beth Israel Deaconess Medical Center's Orthopedic Biomechanics Laboratory for allowing me access to their facilities and their invaluable guidance in the preparation of samples. Thanks also to Dr. Christophe Bacon, who generously took time out of his busy schedule to answer my questions and offer advice on implementation of his technique in MATLAB.

Last, but certainly not least, I would like to acknowledge my parents. Their unconditional support and love has been the safety net which allows me to reach for and achieve my goals. Perhaps more importantly though, they've provided me with a sense of perspective and instilled in me the understanding that success in and of its own is meaningless unless it brings with it happiness and a sense of personal fulfillment.



# Contents

<b>1</b>	<b>Introduction</b>	<b>17</b>
<b>2</b>	<b>Background</b>	<b>21</b>
2.1	Bone Structure . . . . .	21
2.2	Mechanical Characterization of Bone . . . . .	23
2.3	Development of the Hopkinson Pressure Bar Technique . . . . .	34
2.4	Linear Elastic Split-Hopkinson Pressure Bar Theory . . . . .	37
2.5	Viscoelastic Split-Hopkinson Pressure Bar Theory . . . . .	42
<b>3</b>	<b>Experimental Methods</b>	<b>47</b>
3.1	The Aluminum Split-Hopkinson Pressure Bars . . . . .	48
3.2	The PMMA Split-Hopkinson Pressure Bars . . . . .	51
3.3	Sample Preparation . . . . .	52
<b>4</b>	<b>Results and Discussion</b>	<b>57</b>
4.1	Polyurea (PU) . . . . .	58
4.1.1	Solid Aluminum Pressure Bars . . . . .	58
4.1.2	Hollow Aluminum Transmission Bar . . . . .	61
4.1.3	PMMA Pressure Bars . . . . .	70
4.1.4	Polyurea (PU) Analysis Summary . . . . .	73
4.2	Trabecular Bone . . . . .	73
4.2.1	Solid Aluminum Pressure Bars . . . . .	74
4.2.2	Hollow Aluminum Transmission Bar . . . . .	78

4.2.3	PMMA Pressure Bars (6" Striker)	81
4.2.4	PMMA Pressure Bars (8" Striker)	85
4.2.5	Trabecular Bone Analysis Summary	88
<b>5</b>	<b>Conclusions and Recommendations for Future Work</b>	<b>89</b>
<b>A</b>	<b>ALSHPB.m Procedure</b>	<b>93</b>
<b>B</b>	<b>ALSHPB.m Code</b>	<b>103</b>
<b>C</b>	<b>CHARACTERIZE.m Procedure</b>	<b>121</b>
<b>D</b>	<b>CHARACTERIZE.m Code</b>	<b>133</b>
<b>E</b>	<b>PMMASHPB.m Procedure</b>	<b>145</b>
<b>F</b>	<b>PMMASHPB.m Code</b>	<b>153</b>
<b>G</b>	<b>Functions Furnished by C. Bacon</b>	<b>172</b>
G.1	ValAtTime.m	172
G.2	MakeEven.m	173
G.3	MakeOdd.m	173
<b>H</b>	<b>Finding a Benchmark Synthetic Material</b>	<b>174</b>
<b>I</b>	<b>Model Validation with Gas Gun Trials</b>	<b>178</b>

# List of Figures

2-1	Scanning electron micrographs of cancellous bone. . . . .	22
2-2	Microstructure of compact bone (Adapted from <a href="http://training.seer.cancer.gov">http://training.seer.cancer.gov</a> ). . . . .	23
2-3	Stress strain curves for wet compact bone [15]. . . . .	24
2-4	Table of trabecular Young's moduli compiled by Gibson and Ashby [15]. . . . .	25
2-5	Trabecular bone compressive stress vs. strain curves for various relative densities. . . . .	26
2-6	Trabecular bone Young's moduli data of unspecified orientation [15]. . . . .	27
2-7	Strength vs. relative density plots show a large amount of scatter when trabecular orientation is not taken into account. . . . .	28
2-8	Scatter in the data is greatly reduced when trabecular orientation is taken into account. . . . .	29
2-9	Stress vs. strain plots generated by McElhaney for human bone at various strain rates [24]. . . . .	33
2-10	Schematic of pressure vs. position along cylindrical bar [18]. . . . .	34
2-11	Reflection of a compressive wave as a tensile wave at the free end of a cylindrical rod [18]. . . . .	36
2-12	Pressure produced from detonation of one ounce of dry primer as calculated by Bertram Hopkinson [18]. . . . .	36
2-13	Schematic diagram of the modern split-Hopkinson pressure bar configuration. . . . .	37
2-14	Representative incident and transmission bar pulses [26]. . . . .	38
2-15	Example of a pulse's dispersion and attenuation as it travels back and forth within a PMMA incident bar. . . . .	45
3-1	Schematic diagram of MIT's split Hopkinson pressure bar facility. . . . .	48

3-2	A Cordin 550 high speed digital camera is used to record the compression of the SHPB samples. . . . .	50
3-3	Intact bovine femurs are transported to the Orthopedic Biomechanics Laboratory at Beth Isreal Deaconess Medical Center for machining. . . . .	53
3-4	The distal end of the femur is clamped in place to be cored with an 8mm diameter diamond masonry bit. . . . .	54
3-5	A cut is made perpendicular to the knee to release the trabecular cores. . . . .	55
3-6	A trabecular bone core prior to sectioning. . . . .	55
3-7	An irrigated diamond encrusted wafering saw is used to section the cores into orthogonal right cylinders. . . . .	56
4-1	Polyurea specimens tested at 30 psi with the solid aluminum SHPB set-up. . . .	59
4-2	Polyurea specimens tested at 60 psi with the solid aluminum SHPB set-up. . . .	59
4-3	Polyurea specimens tested at 90 psi with the solid aluminum SHPB set-up. . . .	60
4-4	Average trends for polyurea tested with the solid aluminum SHPB set-up. . . .	60
4-5	Polyurea specimens tested at 30 psi with the hollow aluminum SHPB set-up and no pulse shaper. . . . .	62
4-6	Polyurea specimens tested at 60 psi with the hollow aluminum SHPB set-up and no pulse shaper. . . . .	62
4-7	Average trends for polyurea tested with the hollow aluminum SHPB set-up and no pulse shaper. . . . .	63
4-8	Polyurea specimens tested at 30 psi with the hollow aluminum SHPB set-up and a copper pulse shaper. . . . .	65
4-9	Polyurea specimens tested at 60 psi with the hollow aluminum SHPB set-up and a copper pulse shaper. . . . .	65
4-10	Average trends for polyurea tested with the hollow aluminum SHPB set-up and a copper pulse shaper. . . . .	66
4-11	Polyurea specimens tested at 30 psi with the hollow aluminum SHPB set-up and a paper pulse shaper. . . . .	68
4-12	Polyurea specimens tested at 60 psi with the hollow aluminum SHPB set-up and a paper pulse shaper. . . . .	68

4-13 Average trends for polyurea tested with the hollow aluminum SHPB set-up and a paper pulse shaper. . . . .	69
4-14 Polyurea specimens tested at 30 psi with the PMMA SHPB set-up and either a 6" or 10" striker. . . . .	71
4-15 Polyurea specimens tested at 60 psi with the PMMA SHPB set-up and either a 6" or 10" striker. . . . .	71
4-16 Average trends for polyurea tested with the PMMA SHPB set-up. . . . .	72
4-17 Summary of all polyurea results. . . . .	73
4-18 High speed photography of bone specimen being tested on the SHPB. . . . .	75
4-19 Bovine trabecular bone specimens tested at 20 psi with the solid aluminum SHPB set-up. . . . .	75
4-20 Bovine trabecular bone specimens tested at 40 psi with the solid aluminum SHPB set-up. . . . .	76
4-21 Bovine trabecular bone specimens tested at 60 psi with the solid aluminum SHPB set-up. . . . .	76
4-22 Average trends for bovine trabecular bone samples tested with the solid aluminum SHPB set-up. . . . .	77
4-23 Bovine trabecular bone specimens tested at 20 psi with the hollow aluminum SHPB set-up. . . . .	79
4-24 Bovine trabecular bone specimens tested at 40 psi with the hollow aluminum SHPB set-up. . . . .	79
4-25 Bovine trabecular bone specimens tested at 60 psi with the hollow aluminum SHPB set-up. . . . .	80
4-26 Average trends for bovine trabecular bone samples tested with the hollow aluminum SHPB set-up. . . . .	80
4-27 Bovine trabecular bone specimens tested at 20 psi with the PMMA SHPB set-up and a 6" striker. . . . .	82
4-28 Bovine trabecular bone specimens tested at 40 psi with the PMMA SHPB set-up and a 6" striker. . . . .	82

4-29	Bovine trabecular bone specimens tested at 60 psi with the PMMA SHPB set-up and a 6" striker. . . . .	83
4-30	Average trends for bovine trabecular bone specimens tested with the PMMA SHPB set-up and a 6" striker. . . . .	83
4-31	Bovine trabecular bone specimens tested at 20 psi with the PMMA SHPB set-up and an 8" striker. . . . .	86
4-32	Bovine trabecular bone specimens tested at 40 psi with the PMMA SHPB set-up and an 8" striker. . . . .	86
4-33	Bovine trabecular bone specimens tested at 60 psi with the PMMA SHPB set-up and an 8" striker. . . . .	87
4-34	Average trends for bovine trabecular bone specimens tested with the PMMA SHPB set-up and an 8" striker. . . . .	87
4-35	Summary of all trabecular bone results. . . . .	88
A-1	Establishing a reliable baseline is essential to accurately isolating pulses. . . . .	94
A-2	A smoothing function is used to assist in finding the start of the transmission pulse. . . . .	96
A-3	Overlapping pulse plots with visual markers allow the user to verify the selection of starting and ending points. . . . .	96
A-4	Good force balance obtained for a PU specimen tested on the solid aluminum bar by manually adjusting the selection time. . . . .	97
A-5	The force balance for the same solid aluminum PU trial prior to manual adjustment. . . . .	98
A-6	Examples of the stress plots generated for a PU sample tested on the hollow aluminum bars. . . . .	100
A-7	Examples of the strain plots for a PU sample tested on the hollow aluminum bars. . . . .	100
A-8	Examples of the strain rate plots for a PU sample tested on the hollow aluminum bars. . . . .	101
A-9	Examples of the stress vs. strain plots for a PU sample tested on the hollow aluminum bars. . . . .	101
C-1	Shorter striker bars allow for a more complete frequency spectrum. . . . .	122



C-2	A more complete frequency spectrum allows for more accurate calculation of the propagation coefficient gamma. . . . .	122
C-3	The original and resampled signals are plotted side-by-side to assure they match.	123
C-4	Pulse overlays are plotted for the user to check visually. . . . .	124
C-5	The phase angle of the transfer function after numerical unwrapping. . . . .	126
C-6	The calculated components of gamma become extremely unreliable at high frequencies. . . . .	126
C-7	Amendment of the high frequency phase velocities. . . . .	127
C-8	Amendment of the high frequency attenuation coefficients. . . . .	128
C-9	The wave number is also updated in accordance with the amended phase velocities. . . . .	128
C-10	Coefficients for frequencies below the threshold frequency of 25 kHz. . . . .	129
C-11	Employing a threshold frequency dramatically increases accuracy of the propagation predictions. . . . .	129
C-12	A characterization trial prediction utilizing the 2" striker bar. . . . .	130
E-1	The frequency vector is plotted for the user to visually check. . . . .	147
E-2	The omega squared values are also plotted for the user to visually check. . . . .	147
E-3	The calculated front and rear forces on the specimen are plotted for the user to verify dynamic equilibrium. . . . .	149
E-4	The calculated front and rear face velocities are plotted for inspection. . . . .	150
E-5	The engineering and true strains are plotted side by side against time. . . . .	150
E-6	The engineering and true strain rates are plotted side by side against time. . . . .	151
E-7	The engineering and approximated true stresses are plotted side by side against time. . . . .	151
E-8	Engineering stress vs. engineering strain as calculated by PMMASHPB.m for a trial on a PU specimen. . . . .	152
E-9	Approximated true stress vs. true strain as calculated by PMMASHPB.m for the same PU trial. . . . .	152

H-1	Ordinance 250A Ballistic Gelatine, the current industry standard, is highly temperature dependent. . . . .	175
H-2	Images of a PMMA SHPB test on RTV 6166. . . . .	176
I-1	Schematic representation of the gas gun facility used to evaluate the accuracy of predictions made by the computational models. . . . .	179
I-2	CAD drawing of the gel clamp's support side. . . . .	180
I-3	CAD drawing of the gel clamp's view side. . . . .	180
I-4	CAD drawing of the gel clamp's platform. . . . .	181
I-5	CAD drawing of the gel clamp's supports. . . . .	181
I-6	CAD drawing of the assembled gel clamp. . . . .	182
I-7	Penetration of Ordinance 250A Ballistic Gellatin block with a 1/2" diameter polycarbonate projectile fired at approximately 500 m/s. . . . .	182
I-8	Example of the image correlation technique applied a low rate mechanical test of Ordinance 250A Ballistic Gelatin. . . . .	183

# List of Tables

- 4.1 Polyurea samples tested with the solid aluminum SHPB set-up. . . . . 58
- 4.2 Polyurea samples tested with the hollow aluminum SHPB set-up and no pulse shaper. . . . . 63
- 4.3 Polyurea samples tested with the solid aluminum SHPB set-up and a copper pulse shaper. . . . . 64
- 4.4 Polyurea samples tested with the solid aluminum SHPB set-up and a paper pulse shaper. . . . . 69
- 4.5 Polyurea samples tested with the PMMA SHPB set-up. . . . . 72
- 4.6 Bovine trabecular bone samples tested with the solid aluminum SHPB. . . . . 77
- 4.7 Bovine trabecular bone samples tested with hollow aluminum SHPB. . . . . 78
- 4.8 Bovine trabecular bone samples tested with the PMMA SHPB set-up and a 6" striker. . . . . 84
- 4.9 Bovine trabecular bone samples tested with the PMMA SHPB set-up and an 8" striker. . . . . 85



# Chapter 1

## Introduction

The work presented in this thesis is part of an ongoing investigation at MIT's Institute for Soldier Nanotechnologies focusing on the simulation of behind-armor effects of ballistic threats (Project 6.9). This study is aimed at developing numerical models that can accurately predict the effects of ballistic events on the human body, particularly one that is protected by a ballistic armor system. It is well understood that the ability of such an armor system to neutralize a threat is greatly affected by the coupled response of the armor and the backing material. In the case of our study, the backing material is composed of the various biological tissues of the human body. By accurately modeling each of these individual tissues, we hope to be able to accurately capture the complex interactions between the armor and the user's body. The insight gained through this modelling technique will help guide the design of future armor architecture; allowing us to maximize personal protection while minimizing the weight of the system and maximizing the mobility of its user.

This wide reaching project has three distinct phases, the first of which is the improved characterization of the high rate properties of biological tissues and tissue simulants necessary to obtain accurate models. This thesis is a first step towards achieving that characterization *ex-vivo*. Because of its structural importance within the head and body, and also because its material properties are such that it can be characterized using both the aluminum and PMMA split-Hopkinson pressure bar (SHPB) techniques, trabecular bone was chosen as the first tissue to characterize, and is the main focus of this thesis. Chapter 2 of this work provides a brief overview of the current knowledge pertaining trabecular bone's mechanical properties, as well

as the history and theory of the SHPB technique employed in this study. Chapter 3 discusses the specific experimental methods and analysis procedures. Finally, Chapter 4 presents the results of the study and Chapter 5 provides conclusions and recommendations for future work pertaining to trabecular bone. Future work is also planned to apply the high rate ex-vivo characterization techniques employed in this thesis to softer tissues such as brain, muscle, and fat. Also, concurrent work is being conducted to characterize these same materials in-vivo. It is hoped that the combination of these two approaches will elucidate not only the mechanical characteristics of these tissues, but also the nature of the changes in tissue properties associated with ex-vivo testing protocols, thereby reducing the need for in-vivo testing procedures in the future.

The second phase of Project 6.9 is the development of constitutive models for biological tissues and tissue simulants under high rate loading. Unlike other approaches often taken in the modeling of biological tissues, our constitutive model incorporates specific features which reflect the tissue's molecular structure at the nano- and micro- scales, thereby relating the tissues' mechanical properties directly to its biochemistry. This hierarchical approach to modeling is naturally suited to allowing a singular constitutive framework to be specialized into differentiated models by varying the appropriate biochemical parameters to capture the response of different classes of tissues and organs. The supplemental task of modeling tissue simulants was incorporated into our study because of its importance in assessing the validity of the currently employed techniques for evaluating ballistic protection. Also, it is hoped that by concurrently studying both biological tissues and tissue simulants, we will be able evaluate each simulant's biofidelity, thereby aiding in the development of more accurate physical models of the both the head and torso. Information pertaining to the work on tissue simulants can be found in Appendix H.

The third and final phase of Project 6.9 will be the development and evaluation of three dimensional finite element models capable of predicting injury levels from non-penetrating bullets and fragments. The development of these accurate numerical models will allow us to correctly capture the complex interactions between the armor system and the biological backing material it is meant to protect, guiding the refinement and optimization of future armor systems. As a supplement to these models, and to check the accuracy of their predictions under realistic

impact scenarios, we are currently developing an experimental set-up in our gas gun facility that will allow us to impact a coupled armor-tissue stimulant system and map the resulting strain waves as they travel through a tissue stimulant backing. This work is presented in Appendix I.





## Chapter 2

# Background

### 2.1 Bone Structure

By simply looking at several intact bones, one can easily see that they come in wide variety of complex shapes and sizes. What might not be as apparent, however, is that each bone is not a homogeneous structure, but rather a complex system - optimally designed to fulfill its individual role within the body.

In general, most bones have a two phase construction. The outer part is a shell of solid, compact bone (also called cortical bone) which behaves as the loading surface and encloses a core of porous cellular bone, known as either cancellous or trabecular bone. This two phase construction allows the body to optimize bone strength while minimizing weight by adjusting the density and composition of the internal trabecular core. In fact, it has been recognized for well over a century that bone's growth increases in response to stress [33]. Perhaps even more interesting is that this growth occurs preferentially in the directions of principal stress [30], [9]. Areas within the bone where stress is low develop an open cellular framework with a relatively low density of thin rod-like trabeculae [15]. Areas within the bone that experience high levels of stress, however, develop a high density of thick plate-like trabeculae that result in a nearly closed cell composition. Furthermore, areas which experience high stresses in one direction and low stresses in others develop an anisotropic framework to match the stress fields; these regions have plate-like trabeculae parallel to the high stress concentrations and rod-like trabeculae along the lower stress orientations (Fig. 2-1).

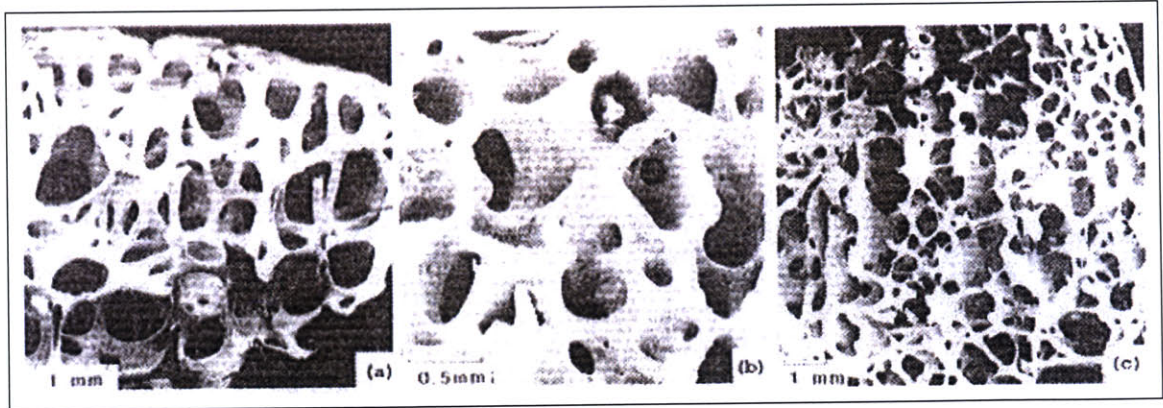


Figure 2-1: Scanning electron micrographs of cancellous bone. (a) Femoral head specimen demonstrating a low-density, open-cell structure with rod-like trabeculae. (b) Femoral head specimen demonstrating a higher-density composition with thick plate-like trabeculae. (c) Femoral condyle specimen demonstrating intermediate density with plate-like trabeculae parallel to stress orientation and rod-like trabeculae perpendicular. [14]

At an even smaller scale, on the order of nanometers, all bone can be seen as a composite structure: a fibrous, organic matrix of collagen and other proteins intertwined with inorganic molecules such as crystalline hydroxyapatite and amorphous calcium phosphate [15]. It is the inorganic calcium compounds that gives bones their stiffness and the organic components that bind everything together and give the system its strength and toughness.

Within cortical bone this collagen-calcium matrix forms osteons: hollow Haversian canals carrying blood vessels and nerves surrounded by concentric rings of hard lamellae and interconnected by a series of canaliculi, or Volkmann's canals (Fig. 2-2). This arrangement, also known as Haversian systems, allows oxygen and nutrients to be carried to lacunae housed osteocytes deep within the otherwise impenetrable regions of the bone.

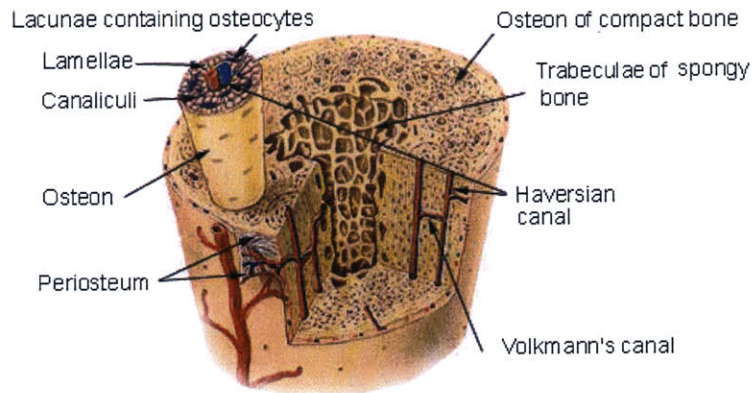


Figure 2-2: Microstructure of compact bone (Adapted from <http://training.seer.cancer.gov>).

In contrast, trabecular bone, because of its less compact structure, does not require this complex arrangement. Nutrients are able to reach its osteocytes directly from the surrounding vasculature. This open cellular structure within trabecular bone not only aids in the transport of nutrients, but as we will see, also gives it some very interesting mechanic properties, not least of which it's high strength to weight ratio.

## 2.2 Mechanical Characterization of Bone

Due to their importance in orthopedic and other medical applications, a great deal of work has been devoted to understanding the mechanical properties of both trabecular and compact bone. Compact bone, however, because of its more uniform structure on the mesoscale, is more easily characterized and has therefore historically drawn more attention within the research community [6], [10], [9], [27]. These studies have found that human compact bone ranges in density from  $1800 \text{ kg/m}^3$  to  $2000 \text{ kg/m}^3$ , possesses a longitudinal Young's modulus of approximately 17 GPa, has radial and tangential Young's moduli of about 11.5 GPa, and exhibits a Poisson's ratio of approximately 0.4 [8], [9]. In addition, widely accepted characteristic curves have been derived for compact bone (Figure 2-3).

It is only recently, however, that the scientific and medical community's understanding of trabecular bone has begun to truly advance, and even now the big picture seems to elude us. For example Lorna Gibson and Michael Ashby, in their book *Cellular Solids: Structures and*

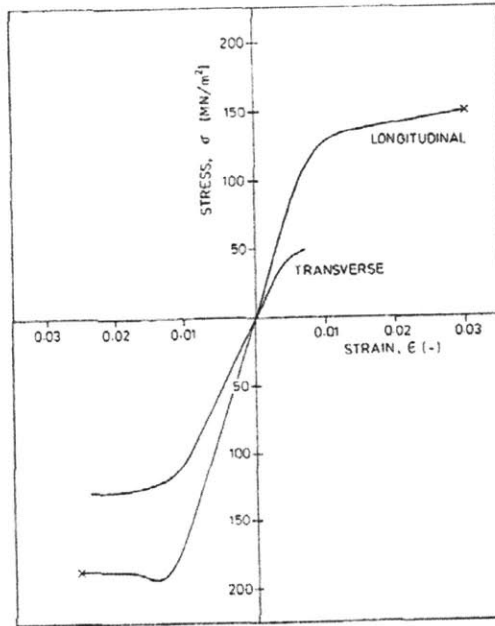


Figure 2-3: Stress strain curves for wet compact bone generated by Gibson [15] (based on data from Reilly and Burnstein [28] and Currey [9]).

*Properties*, provide a table (Figure 2-4) of the various experimental values of Young's modulus for a single trabecula as calculated over the last 30 years; the results vary widely from 0.76 GPa [29] to 14.1 GPa [31]. This variance is due in large part to the difficulty in preparing uniform specimen geometries without introducing significant surface defects, but also to the natural variance between species (usually bovine or human), anatomical locations, and individuals from which the specimens were obtained. Using linear extrapolation, Gibson surmises that the Young's modulus of fully dense trabecular bone, or in other words one trabecula, should be between 2.7 GPa and 9.0 GPa [15].

A study by Richard Ashman and Jae Yong Rho may have found a way around the dilemma of whether it is better to have an imperfect specimen geometry or to introduce surface defects by mechanical machining [1]. They employed ultrasonic testing techniques to measure the time it took for a series of waves to travel through a 5 millimeter diameter specimen of trabecular bone that was 15 millimeters long. From this Ashman and Rho were able to easily approximate the wave velocity,  $c$ , through the individual trabeculae. By also measuring the apparent density,  $\rho$ ,

Reference	Type of bone†	Method	$E_s$ (GPa)
<i>Mechanical tests</i>			
Ryan and Williams (1989)	B F	tension unmachined	0.76 (0.39)
Kuhn <i>et al.</i> (1987)	H T	3-point bend machined	3.17 (1.5)
	H cortical		3.8
Choi <i>et al.</i> (1990)	H PT	3-point bend machined	4.59 (1.60)
	H cortical		5.44 (1.25)
Townsend <i>et al.</i> (1975)	H PT	buckling unmachined	11.4 (wet)
			14.1 (dry)
Runkle and Pugh (1975)	H DF	buckling	8.69 (3.17) dry
<i>Ultrasound tests</i>			
Ashman and Rho (1988)	B F	ultrasound on	10.9 (1.6)
	H F	trabecular bone	13.0 (1.5)
<i>Finite element analysis</i>			
Pugh <i>et al.</i> (1973b)	H DF	2D FEM	$E_s < E_{compact}$
Williams and Lewis (1982)	H PT	2D FEM	1.30
Mente and Lewis (1987)	H F	2D FEM	5.3 (2.6) dry
Rietbergen <i>et al.</i> (1995)	H PT	3D FEM	2.23–10.1

†All specimens are of individual trabeculae unless stated otherwise. B = bovine; H = human; F = femur; T = tibia; P = proximal; D = distal.

Figure 2-4: Table of trabecular Young's moduli compiled by Gibson and Ashby [15].

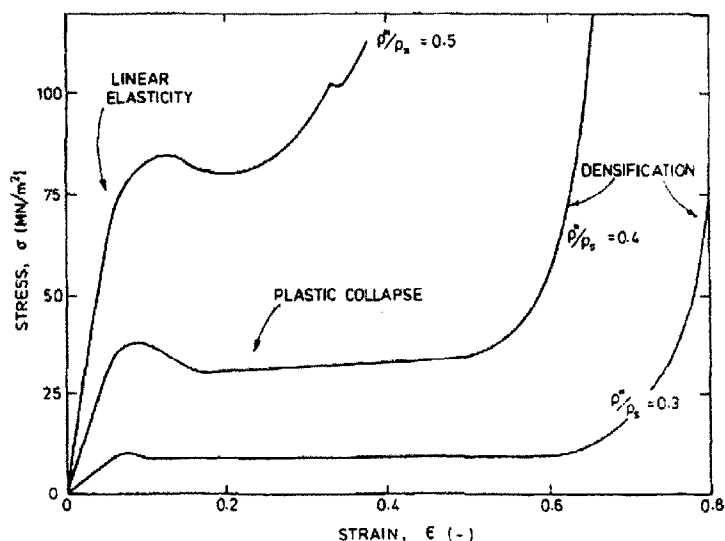


Figure 2-5: Trabecular bone compressive stress vs. strain curves for various relative densities (as generated by Hayes and Carter [17]).

they could then employ elastic wave propagation theory,  $c = \sqrt{E/\rho}$ , to estimate  $E$ , the Young's modulus of the individual trabeculae. For human and bovine trabeculae they arrived at values of 13.0 GPa and 10.9, respectively, both with a standard deviation of around 1.5 GPa.

These values, however, are only for one trabecula, whereas we are interested in how these trabeculae behave when combined together to form cancellous bone. The answer, which is most obvious in compression, is that they behave as a cellular solid (Figure 2-5). *Cellular Solids: Structures and Properties* provides an excellent in-depth review of the mechanics behind this behavior. For our purposes of background overview, however, it is sufficient to describe the compressive stress vs. strain curves for trabecular bone as starting with an initial linear elastic region, followed by a plateau in the stress representing plastic collapse and buckling of individual trabeculae within the material, and finally and sharp upshoot indicating densification of the material [15]. The values of strain bounding these regions, as well as the corresponding stress levels, shift as the density is increased, but the nature of the curves appear to remain constant at least until the relative density reaches an upper bound of about 0.5 (see again Figure 2-5).

Density also plays an important role in several other aspects of trabecular bone's behavior, but should be considered in conjunction with the internal orientation of trabeculae. Reproduced



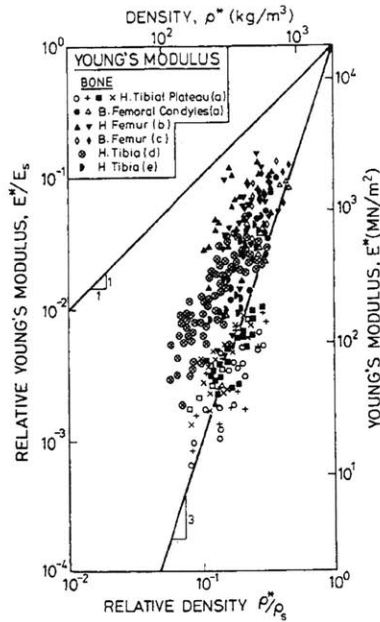
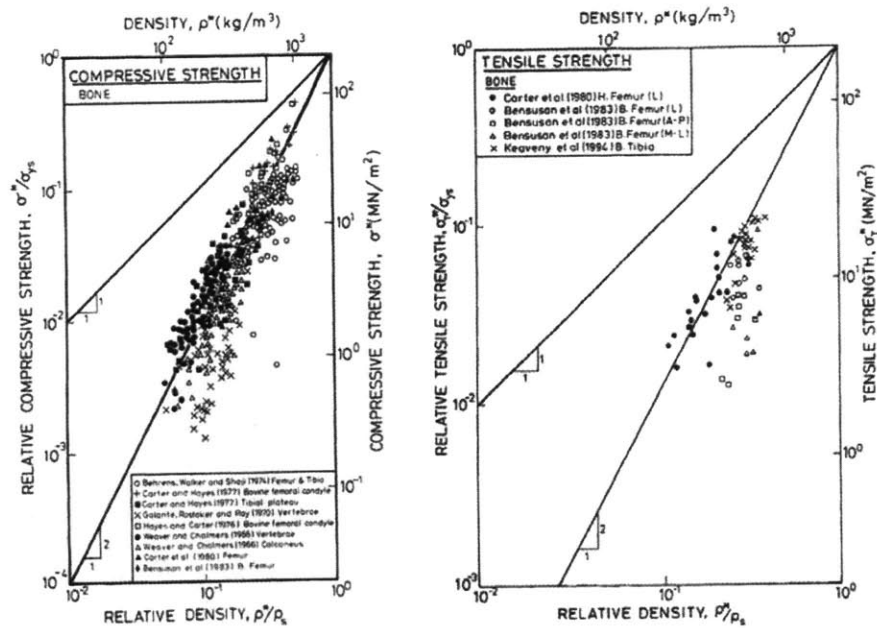


Figure 2-6: Trabecular bone Young's moduli data of unspecified orientation from various sources ((a) Carter and Hayes [4], (b) Carter et. al. [5], (c) Bensusan et. al. [2], (d) Hvid et. al. [19], and (e) Linde et. al. [23]) as gathered and plotted by L. Gibson [15].

here are three figures compiled by Gibson and Ashby which demonstrate the effect of density alone on Young's modulus (Figure 2-6), compressive strength (Figure 2-7 (a)), and tensile strength (Figure 2-7 (b)). Close examination reveals a rather large variance in the data. The principle reason for this is that these figures ignore any dependence upon trabecular orientation. In reality, bones with a preferred stress orientation are highly anisotropic and have been shown to demonstrate up to a ten fold increase in measured strength simply by changing the testing orientation [32]. Utilizing data from the 1982 Williams and Lewis study, Gibson and Ashby show that correlation with density for both Young's modulus (Figure 2-8 (a)) and compressive strength (Figure 2-8 (b)) can be notably improved by taking trabecular orientation into account. Bearing this information in mind, all samples in this study were prepared with their axis aligned to the principal stress orientation of the bone and the density of each specimen was accurately recorded for future statistical analysis (see Sample Preparation in Chapter 3).

In addition to dependence upon density and orientation, it has often been noted that trabecular bone's properties vary significantly when one varies the anatomical site from which the

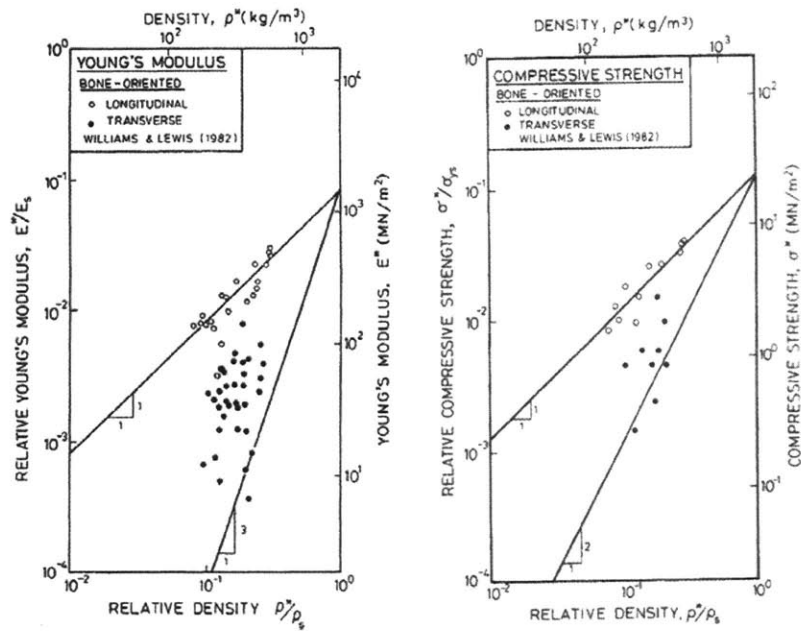


(a) Trabecular bone compressive strength vs. relative density data of unspecified orientation from various sources as gathered and plotted by Gibson.

(b) Trabecular bone tensile strength vs. relative density data of unspecified orientation from various sources as gathered and plotted by Gibson.

Figure 2-7: Strength vs. relative density plots show a large amount of scatter when trabecular orientation is not taken into account.





(a) Trabecular bone Young's modulus vs. relative density with orientation taken into account.

(b) Trabecular bone compressive strength vs. relative density with orientation taken into account.

Figure 2-8: Scatter in the data is greatly reduced when trabecular orientation is taken into account.

samples are taken. In a 2003 article published in the Journal of Biomechanics, Morgan, Keaveny, and Bayraktar cite that predicted values of modulus at a specific apparent density differ by as much as 49% and that prediction errors can increase by more than 60% if site-dependence is ignored [25]. Bearing this in mind, Morgan et. al. devised a study to investigate the site-dependence of on-axis modulus-density relationships for human trabecular bone. They tested 142 specimens of human trabecular bone from the vertebra, proximal tibia, femoral greater trochanter, and femoral neck to study if the differences with regard to anatomical site meant that each site behaved as a different material and must be treated separately, or if there was some additional underlying parameter that had been missing in earlier formulations. They found that by including an architecture term representing the type of cellular structure within the specimen, the difference in the calculated coefficients between anatomical sites was no longer statistically significant. For our study this finding has several important implications. First, it indicates that the end product of this entire project, the constitutive and finite element models, will also have to take the architecture of the cellular structure into account. Second, and on a more immediate time scale, it means that in order to reduce the number of variables in the data analysis, the samples employed in our study have to be harvested from the same animal model and anatomical site.

Finally, the last major factor affecting the mechanical response of trabecular bone, in addition to density, orientation, and anatomical site, is the rate at which it is strained. Dennis Carter and Wilson Hayes were the first two researchers to explore this relationship in depth and were able to greatly increase our understanding of these materials by quantifying how their compressive strength changes as we increase the rate at which we deform them, i.e. the strain rate. Employing a confined cylindrical compression fixture to test both human and bovine trabecular samples to a minimum of 50% compressive strain at strain rates ranging from 0.001 s<sup>-1</sup> to 10 s<sup>-1</sup>, they surmised that the longitudinal compressive strength of trabecular bone can be related to the that of the better understood compact bone with the following empirical relationship:

$$S = S_c \left( \frac{d\varepsilon}{dt} \right)^{0.06} \left( \frac{\rho}{\rho_c} \right)^2 \quad (2.1)$$

where  $\rho$  is apparent density of the sample being tested at a strain rate of  $\frac{d\varepsilon}{dt}$ , and  $S_c$  is the

compressive strength of a compact bone sample with density  $\rho_c$ , tested at a strain rate of  $1.0 \text{ s}^{-1}$  [3]. The apparent densities of the samples tested, being 5mm thick and 10.3 mm in radius, varied greatly from 0.07 to  $0.97 \text{ g/cm}^3$  and gave excellent insight into the role of density in this equation. In addition, they noted that viscous flow of marrow out of the pores led to a strengthening of the marrow in situ specimens tested, but only at the highest rate strain rate of  $10 \text{ s}^{-1}$ . Unfortunately, Carter and Hayes did not follow up this observation with future studies at rates higher than  $10 \text{ s}^{-1}$ . Also, while the relationship of compressive strength to that of strain rate and apparent density was carefully quantified, many of the other important mechanical properties were not addressed.

More recently, work has been conducted by Linde, Norgaard, Hvid, Odgaard and Soballe to study how strain rate and apparent density might effect the measurement of some of these additional mechanical properties; namely stiffness, strength and ultimate strain. Six decades of strain rate, ranging from  $0.0001 \text{ s}^{-1}$  to  $10 \text{ s}^{-1}$ , were imposed in 60 specimens of trabecular bone taken from a human proximal tibia [23]. The samples ranged in apparent density from  $0.23 \text{ g/cm}^3$  to  $0.59 \text{ g/cm}^3$ , not as diverse as those employed in the Carter and Hayes study, but still significant. They employed numerous linear and non-linear regression analysis models with strain rate and apparent density as the independent variable to find quantitative models for their dependant variables of strength, stiffness, and ultimate strain. Ultimately, they found that ultimate strain varied independently of apparent density, but showed a power function dependence upon strain rate. The exponent they calculated for this relationship was 0.03. Additionally, they found the variations in strength and stiffness with strain rate could be captured equally well with linear or power function relationships. The power function relationship between strength and strain rate had an exponent of 0.07, and that between stiffness and strain rate an exponent of 0.05. Both of these values show a good correspondence with the values derived in the previously discussed Carter and Hayes study.

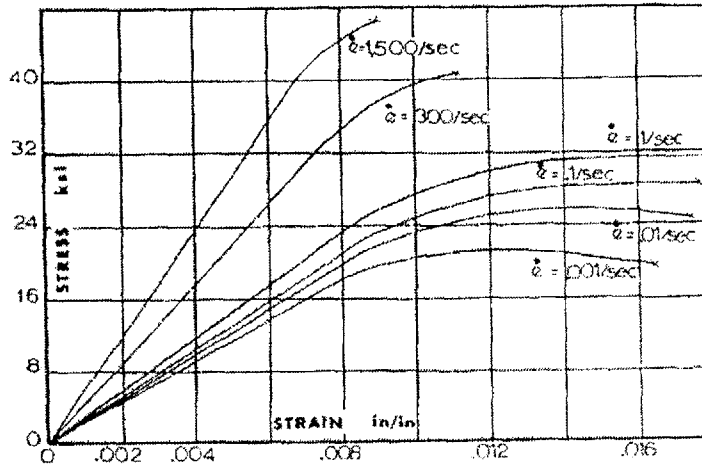
While a significant amount work has been directed towards characterizing and understanding both cortical and trabecular at low strain rates, very little is known about these materials at strain rates of more than  $10 \text{ s}^{-1}$ . In fact, during our extensive literature search we found only one item that specifically addressed the high strain rate characterization of bone: James McElhaney's 1966 article, "Dynamic Response of Bone and Muscle Tissue" [24]. In this

article, McElhaney describes how he constructed a novel air gun testing apparatus capable of conducting constant velocity compression tests at strain rates of up to  $4000 \text{ s}^{-1}$ . He utilized this apparatus, in conjunction with a Tinius Olsen electromatic testing machine for static and low rate tests, to characterize bovine and human femora samples at rates of  $0.001 \text{ s}^{-1}$ ,  $0.01 \text{ s}^{-1}$ ,  $0.1 \text{ s}^{-1}$ ,  $1 \text{ s}^{-1}$ ,  $300 \text{ s}^{-1}$ , and  $1500 \text{ s}^{-1}$ .

McElhaney describes the samples tested as coming from either the right femur of a 24-year-old white male who died of acute cardiac failure or the right femur of a 3-year-old steer. He states that the middle third of the shaft of the femora was used to collect both sample types and identifies the densities of each to be  $0.068 \text{ lbs/in}^3$  ( $1880 \text{ kg/m}^3$ ) and  $0.070 \text{ lbs/in}^3$  ( $1940 \text{ kg/m}^3$ ), respectively. McElhaney does not make any explicit note of whether these specimens are cortical or cancellous, but given the density and the location from which the samples were taken, it can be surmised that they were almost certainly cortical. McElhaney also notes that, "no attempt was made to study the variation of properties with location." Perhaps more importantly, almost no information was provided regarding the type or density of each bone sample tested, parameters that are now known to be a major contributing factors to the mechanical properties of bone.

The testing specimens were machined into  $0.175''$  by  $0.175''$  by  $0.250''$  blocks prior to testing. The bovine samples were stored in water and refrigerated until the time of testing, which for the high rate trials was approximately thirty days after the animal had been sacrificed, while the human samples were embalmed with formalin, phenol, alcohol, and glycerin. This embalming may have changed the mechanical properties from those found in fresh tissue samples [21], although at the time McElhaney maintained that it should not.

The final plot generated by McElhaney is true stress vs. engineering strain (Figure 2-9), where the instantaneous area in the stress calculation was estimated by using a Poisson ratio derived from a low rate compression test conducted on dry beef bone. Overall the work is extremely insightful and the generated curves appear concise and accurate. Unfortunately for us, no subsequent high rate work appears to have been undertaken by McElhaney or his predecessors. As such, we felt it would be well worth undertaking a new high rate study, this one specifically on trabecular bone and benefitting from the numerous insights gained in the last forty decades regarding the importance of density, orientation, and proper specimen



Stress-strain curves for human bone.

Figure 2-9: Stress vs. strain plots generated by McElhaney for human bone at various strain rates [24].

preservation. To undertaken this work it was decided to employ the now widely accepted split-Hopkinson pressure bar technique (SHPB), whose history and theory we will now review.

## 2.3 Development of the Hopkinson Pressure Bar Technique

The theory underlying the modern split-Hopkinson pressure bar was first presented by Bertram Hopkinson in his famous paper of 1914 for the *Philosophical Transactions of the Royal Society of London*. At the time, Hopkinson was looking for a way to measure the pressures produced by bullet impacts and the detonation of explosives. He could have easily measured the total momentum produced by these events and divide by the time duration to calculate an average pressure transmitted to the target, but he was interested in obtaining a more detailed understanding of how these pressures varied with time [18].

Hopkinson realized that a pressure wave created by this type of impact or detonation, if transmitted in a perfectly elastic manner, would travel along a cylindrical bar in such a way that the relationship along the bar between pressure and position at any particular instant would be directly related to the pressure versus time relationship during the initial loading (Figure 2-10). He also realized that the pressure distribution within the bar was linearly related to that of the distribution of velocity within the bar. For example, in his experiments he calculated that an instantaneous pressure of one ton per square inch would linearly correspond to an instantaneous velocity of 1.3 feet per second at that same point. Furthermore, he realized that for a steel rod with a longitudinal sound velocity of 17,000 fps, every inch along the bar would be representative of approximately 1/200,000th of a second during the initial impact or detonation. Consequently, Hopkinson could easily correlate velocity to pressure and position to time.

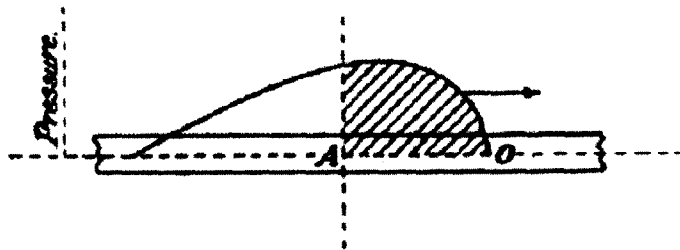


Figure 2-10: Schematic of pressure vs. position along cylindrical bar [18].

A pressure wave will travel axially through a cylindrical linearly elastic rod at the longitudinal sound velocity  $c_{el} = \sqrt{E/\rho}$ , where  $E$  is the Young's modulus of the material and  $\rho$  is its

density. As the wave passes over a section of rod it will accelerate the rod's particles to a maximum velocity and subsequently decelerate the particles to rest, leaving them at some forward displacement. For example, examining Figure 2-10, we see that section A has been acted on by the pressure wave for a time of  $AO/c_{el}$ , the distance the front of the wave has traveled divided by the velocity of the wave. At this instant, section A has experienced a momentum change equal to that of the shaded area in Figure 2-10, the time integral of that portion of the pressure wave which has already passed through section A. In the concise words of Mr. Hopkinson, "The portion of the rod to the right of the section is continually gaining momentum at the expense of the portion to the left while the wave is passing, the rate of transfer at any instant being equal to the pressure."

Since strain gauges had not yet been invented, however, Mr. Hopkinson still needed to devise a method to measure these velocity distributions with respect to position at any given instant. Hopkinson was aware that a propagating compressive wave, upon reaching the free end of a cylindrical rod, would be reflected as a tensile wave with the same velocity and profile as the original compressive wave. He also knew that at any instant the resulting stress at any one cross section of the bar would be equal to the summation of the compressive and tensile waves which were currently acting on that section. Furthermore, he realized that if he were to divide the bar at a particular cross section, creating a shorter rod at one end, a compressive wave would travel through the break unperturbed, but this new end section would separate from the whole as soon as the reflected tensile component of the wave became greater than compressive component at the division (Figure 2-11). The end section of rod would then continue moving forward with the momentum still trapped within it (represented in Figure 2-11 by the shaded region). Hopkinson then surmised that by varying the lengths of these end pieces and measuring the momentum that remained trapped in each, he could deduce the maximum pressure and total duration of the impact as well as the approximate shape of the initial pressure curve (Figure 2-12).

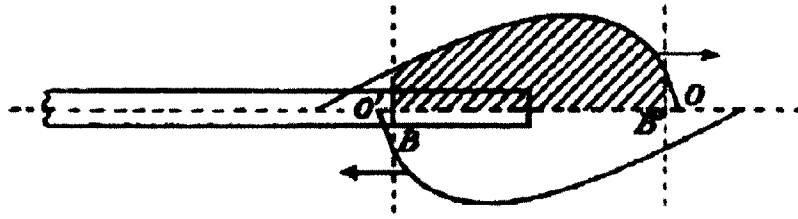


Figure 2-11: Reflection of a compressive wave as a tensile wave at the free end of a cylindrical rod [18].

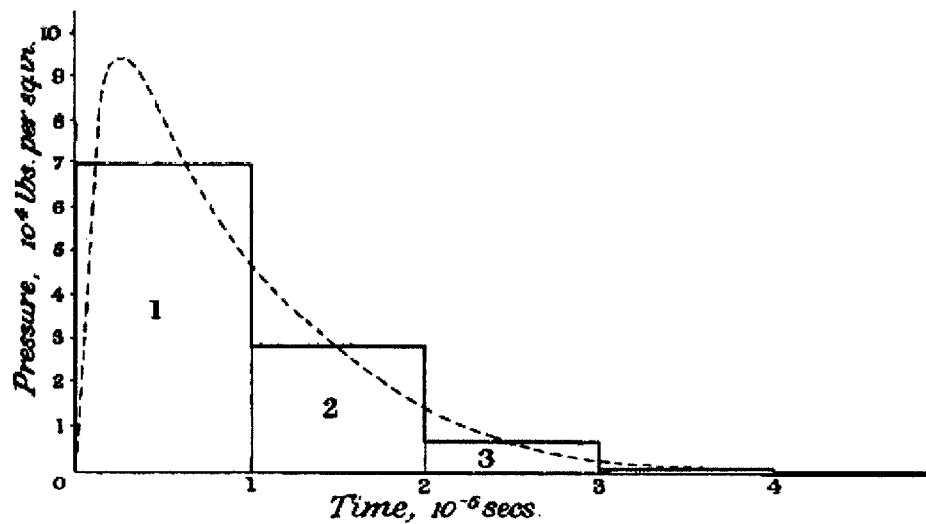


Figure 2-12: Pressure produced from detonation of one ounce of dry primer as calculated by Bertram Hopkinson [18].

Hopkinson's technique did allow better understanding of the shapes of pressure waves produced by events such as ballistic impacts and high explosive detonations, however, the wave calculations were still discretized approximations, not the continuous measurement that Hopkinson would have liked. This level of accuracy was not achieved until 1948 when Davies refined Hopkinson's technique by incorporating electronic condensers along the bar, allowing continuous measurement of bar displacement [12]. A year later Kolsky, also using electronic condensers, further refined the technique by divided the pressure bar into two sections and



sandwiching a material specimen in between. The result was the incident and transmission bar set-up that is most common today (Figure 2-13). This new configuration utilized the principles developed by Hopkinson, but enabled the measurement of both stress and strain within the sandwiched specimen. Kolsky utilized this technique to characterize various rubbers, plastics, and metals. On the softer specimens, he found that he was able to produce compressions of up to 20% over a period of just 20 microseconds [22].

## 2.4 Linear Elastic Split-Hopkinson Pressure Bar Theory

In the split-Hopkinson bar configuration, a striker bar is forced at high speed towards an axially aligned incident bar. This impact induces a compressive stress wave in the incident bar that is twice as long as the length of the striker bar. The wave then travels down the length of the incident bar until it reaches the incident bar-specimen interface. Because of an impedance mismatch with the softer specimen, part of the wave is transmitted through the specimen into the transmission bar, and part of the wave is reflected back along the original incident bar (Figure 2-14). By measuring these signals one can consequently deduce the corresponding stress, which is a function of the transmission signal, and strain, which is a function of the reflected signal, to plot the material's stress vs. strain curves at rates of up to 10,000 strain-per-second.

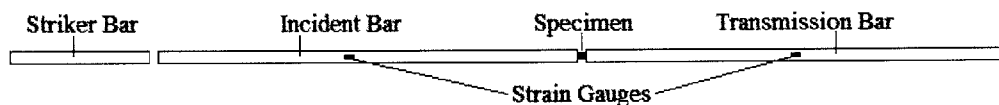


Figure 2-13: Schematic diagram of the modern split-Hopkinson pressure bar configuration.

To see how these calculations are carried out, we will now step through the underlying principles of linear elastic split-Hopkinson pressure bar theory. Two basic assumptions are necessary for this approach: first, wave propagation within the bars must be one dimensional (a condition which is satisfied by having axially aligned bars which are much longer than their diameter); second, the specimen must deform uniformly (a condition which can be verified after the test by comparing the forces on the front and the rear of the sample or by recording the

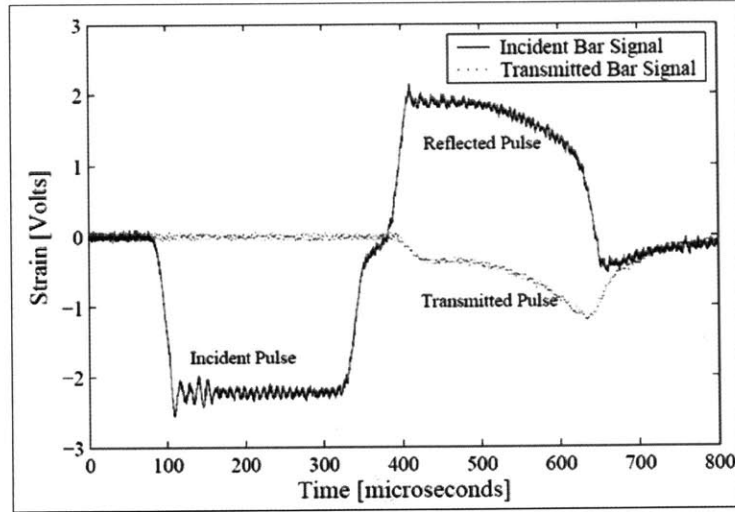


Figure 2-14: As shown here for a polycarbonate sample, part of the initial wave is reflected back through the incident bar and part of the wave is transmitted through the sample into the transmission bar [26].

specimen's deformation with high speed photography). Bearing these requirements in mind, we begin our formulation by defining the strain in the sample as:

$$\varepsilon(t) = \frac{u_i - u_t}{L_s} \quad (2.2)$$

where  $u_i$  is the displacement of the front, or incident interface;  $u_t$  is the displacement of the rear, or transmission interface; and  $L_s$  is the initial length of the specimen in the axial direction. Note that in this sign convention compression is taken to be positive. By differentiating this expression with respect to time, one can arrive at the following expression for strain rate:

$$\frac{d\varepsilon(t)}{dt} = \frac{v_i(t) - v_t(t)}{L_s} \quad (2.3)$$

where  $v_i(t)$  is the velocity of the specimen at the incident interface at time  $t$ , and  $v_t(t)$  is that of the specimen at the transmission interface. To calculate these velocities in the elastic case one can take the product of the longitudinal sound velocity in the bar,  $c_{el}$ , and the total strain at the interface of interest. For the transmission bar, the total strain at the interface is simply  $\varepsilon_t(t)$ , the signal measured by the transmission bar strain gauge; so the velocity at the transmission

face is  $c_{el} * \varepsilon_t(t)$ . For the incident interface, however, the total strain is  $\varepsilon_i(t) - \varepsilon_r(t)$ , the difference between the incident and reflected signals as measured by the incident bar strain gauge; so the velocity at the incident face is  $c_{el} * (\varepsilon_i(t) - \varepsilon_r(t))$ . Combining these new expressions for velocity with (2.3), one can obtain a new formula for the strain rate in terms of the measured strain waves:

$$\frac{d\varepsilon(t)}{dt} = \frac{c_{el}}{L_s}(\varepsilon_i(t) - \varepsilon_r(t) - \varepsilon_t(t)) \quad (2.4)$$

Next, by simple force balance, we can describe the average stress in the specimen as:

$$\sigma(t) = \frac{F_1(t) + F_2(t)}{2A_s} \quad (2.5)$$

where  $F_1(t)$  is the force at the incident bar-sample interface,  $F_2(t)$  is the force at the sample-transmission bar interface, and  $A_s$  is the initial cross section of the specimen. For the elastic case, the forces  $F_1(t)$  and  $F_2(t)$  can be calculated as follows:

$$F_1(t) = EA_0(\varepsilon_i(t) + \varepsilon_r(t)) \quad (2.6)$$

$$F_2(t) = EA_0\varepsilon_t(t) \quad (2.7)$$

where  $E$  is once again the Young's modulus of the material composing the bar, and  $A_0$  is the cross sectional area of the bar. Combining equations (2.6) and (2.7) with equation (2.5), one can obtain the three wave formulation of stress (so called because it is in terms of the measured incident, reflected, and transmitted pulses):

$$\sigma(t) = \frac{EA_0}{2A_s}(\varepsilon_i(t) + \varepsilon_r(t) + \varepsilon_t(t)) \quad (2.8)$$

However, when the sample has reached dynamic equilibrium, and is therefore experiencing uniform deformation, the forces at the front of the specimen will necessarily be equal to the forces at the rear of the specimen. Setting equations (2.6) and (2.7) equal:

$$\varepsilon_i(t) + \varepsilon_r(t) = \varepsilon_t(t) \quad (2.9)$$

Utilizing this assumption, the equations for stress (2.8) and strain rate (2.4) can be simplified to:

$$\sigma(t) = \frac{EA_0}{A_s} \varepsilon_t(t) \quad (2.10)$$

$$\frac{d\varepsilon(t)}{dt} = -\frac{2c_{el}}{L_s} \varepsilon_r(t) \quad (2.11)$$

This formulation is known as the one wave approach (so called because each calculation depends on only one pulse), and while it is advantageous because of its simplicity and decreased sensitivity to noise and timing, its validity should always be checked by examining the force balance to assure that the sample is in dynamic equilibrium during the analysis. When planning an experiment, a widely used rule of thumb is that the pulse must reflect three times within the sample before dynamic equilibrium can be assumed. In addition, local failure at the incident bar end of the sample is often indicative of a violation of the dynamic equilibrium requirement. To avoid this problem, the magnitude of transient stress associated with the sudden application of a velocity  $v_0$  can be calculated as  $\sigma_m = \rho cv_0$ . This stress should not exceed the yield stress of the specimen. Furthermore, high speed photography can be used for certain materials to make sure failure of the specimen is uniform and does not start at either the incident or transmission interfaces.

While the overall linear elastic SHPB technique is widely accepted and works well for samples having impedances only slightly less than the bar, it loses its accuracy when the sample becomes too soft. This is due to the fact that the signal-to-noise ratio in the transmission bar becomes smaller as the specimens examined become softer. To overcome this shortcoming, numerous approaches to refining the split-Hopkinson pressure bar technique have been introduced.

The first approach is simply to use a more sensitive quartz force gauge in place of the standard strain gauges to measure the weak transmission pulse. For this investigation, it was decided that the quartz gauges are too fragile and difficult to calibrate and maintain. Their use in future studies, however, cannot be ruled out.

A second approach, and one employed in this study, is to simply use a hollow linear elastic transmission bar [7]. This method, initially proposed by Chen, Zhang, and Forrestal, enables a larger strain in the transmission bar with the same transmitted force by reducing the effective impedance of the bar. This technique is advantageous in that it requires only slight modification

of the linear elastic equations which were just derived for a solid cylindrical rod. Equations (2.4) and (2.5) for strain rate and stress remain the same, as does equation (2.6) for the front force calculation, but the rear force equation must be updated to reflect the changed area of the transmission bar:

$$F_2(t) = EA_t \varepsilon_t(t) \quad (2.12)$$

where  $A_t$  is the area of the transmission bar. Now substituting equations (2.6) and (2.12) into equation (2.5), we arrive at our new equation for stress:

$$\sigma(t) = \frac{E}{2A_s} (A_0 * (\varepsilon_i(t) + \varepsilon_r(t)) + A_t * \varepsilon_t(t)) \quad (2.13)$$

In addition, when dynamic equilibrium is reached, the force balance previously represented by equation (2.9) is replaced by:

$$A_0 * (\varepsilon_i(t) + \varepsilon_r(t)) = A_t * \varepsilon_t(t) \quad (2.14)$$

As a result equations (2.10) and (2.11) of the one wave approach must be revised as follows:

$$\sigma(t) = \frac{EA_t}{A_s} \varepsilon_t(t) \quad (2.15)$$

$$\frac{d\varepsilon(t)}{dt} = \frac{c_{el}}{L_s} \left[ \varepsilon_i(t) \left( 1 - \frac{A_o}{A_t} \right) - \varepsilon_r(t) \left( 1 + \frac{A_o}{A_t} \right) \right] \quad (2.16)$$

As a final check we note that when  $A_t$  is set equal to  $A_0$ , as in the case of a solid linear elastic transmission bar, all of the above equations reduce to their original form. It should also be noted that this technique still requires a solid specimen interface on the transmission bar. This change in bar geometry raises some concerns over the transmission behavior of high frequency wave components. This concern is often addressed by utilizing pulse shapers to reduce the magnitude of the higher frequency components [7].

The final approach widely used to overcome low signal strength in the transmission bar is to utilize polymer bars. This technique is advantageous in that it produces a larger strain for an equal amount of stress when compared to the softer metals, such as aluminum; however, it

introduces the added complication that the pulse does not travel in a linear elastic manner between the strain gauge and the specimen. The theory and consequences of utilizing viscoelastic pressure bars are discussed in the following section.

## 2.5 Viscoelastic Split-Hopkinson Pressure Bar Theory

Even while developing the fundamental theories employed in his 1914 paper, Bertram Hopkinson recognized that the various harmonic components of a wave would travel down a cylindrical rod at different velocities, and that as a consequence, the overall wave form would change slightly as it propagated down the bar. He calculated, and experimentally verified, that for the materials and length scales used in his particular experiment these effects would be negligible. Using polymer pressure bars to test specimens of soft biological tissue, however, involves length scales on which dispersion and attenuation cannot be neglected. Numerous theories and techniques have been proposed to account for these effects experimentally. For our purposes, however, we chose to employ the method presented by Bacon in his 1998 paper "An Experimental Method for Considering Dispersion and Attenuation in a Viscoelastic Hopkinson Bar," because it accounts not only for the viscoelastic effects of the polymer, but also for the geometric effects of the individual testing system. Furthermore, this method incorporates experimental calculations of the attenuation and dispersion characteristics that can easily be updated as the bars age or as the system is updated with new polymer bars.

Bacon's method is based on the assumption that lateral motion of the bars can be neglected. Using this assumption one can then relate normal stress and longitudinal strain to axial displacement in the following manner:

$$\frac{\partial \sigma(x, t)}{\partial x} = \rho \frac{\partial^2 u(x, t)}{\partial t^2} \quad (2.17)$$

$$\varepsilon(x, t) = \frac{\partial u(x, t)}{\partial x} \quad (2.18)$$

Where  $\sigma$  is stress,  $\varepsilon$  is strain,  $x$  is longitudinal position,  $t$  is time,  $\rho$  is density, and  $u$  is displacement. Equations (2.17) and (2.18) can then be combined and the result described in

the Fourier domain:

$$\frac{\partial^2}{\partial x^2} \bar{\sigma}(x, \omega) = -\rho\omega^2 \bar{\varepsilon}(x, \omega) \quad (2.19)$$

where  $\bar{\sigma}(x, \omega)$  is the Fourier transform of stress and  $\bar{\varepsilon}(x, \omega)$  is the Fourier transform of strain.

Next, employing the concept of a complex Young's modulus,  $E^*(\omega)$ , for the polymer composing the bar, the linear viscoelastic behavior is described in the following manner:

$$\bar{\sigma}(x, \omega) = E^*(\omega) \bar{\varepsilon}(x, \omega) \quad (2.20)$$

Based on  $E^*$ , we can also define a propagation coefficient,  $\gamma(\omega)$ , for the bar:

$$\gamma^2 = -\frac{\rho\omega^2}{E^*} \quad (2.21)$$

In addition, this propagation coefficient can be written in terms of the attenuation coefficient,  $\alpha(\omega)$ ; the wave number,  $k(\omega)$ ; and the phase velocity,  $c(\omega)$ :

$$\gamma(\omega) = \alpha(\omega) + ik(\omega) = \alpha(\omega) + i\frac{\omega}{c(\omega)} \quad (2.22)$$

where both  $\alpha(\omega)$  and  $k(\omega)$  are continuous functions;  $\alpha(\omega)$  being a positive even function and  $k(\omega)$  being an odd function.

Now, combining equations (2.19), (2.20), and (2.21), one can rewrite the one-dimensional equation of axial motion to be:

$$\left(\frac{\partial^2}{\partial x^2} - \gamma^2\right) \bar{\varepsilon}(x, \omega) = 0 \quad (2.23)$$

The general solution of which is:

$$\bar{\varepsilon}(x, \omega) = \tilde{P}(\omega)e^{-\gamma x} + \tilde{N}(\omega)e^{\gamma x} \quad (2.24)$$

where  $\tilde{P}(\omega)$  is the Fourier transform of strain due to waves moving in the positive direction at  $x = 0$ , and  $\tilde{N}(\omega)$  is the Fourier transforms of the strain due to waves moving in the negative direction at  $x = 0$ .

From equation (2.24), we can now calculate the Fourier transforms of axial particle velocity,

$\tilde{v}(x, \omega)$ , and the normal force,  $\tilde{F}(x, \omega)$ , at a cross section  $x$  to be:

$$\tilde{v}(x, \omega) = -\frac{i\omega}{\gamma} [\tilde{P}(\omega)e^{-\gamma x} - \tilde{N}(\omega)e^{\gamma x}] \quad (2.25)$$

$$\tilde{F}(x, \omega) = -\frac{\rho A \omega^2}{\gamma^2} [\tilde{P}(\omega)e^{-\gamma x} + \tilde{N}(\omega)e^{\gamma x}] \quad (2.26)$$

These are the equations can then be employed in calculating the stress and strain of the specimens tested on the viscoelastic pressure bars. By setting  $x$  equal to  $d$ , the distance from the strain gauge to the specimen, and taking the inverse transforms of equation (2.25) once for both the incident bar and transmission bar signals, we can calculate both the velocity of the front face,  $v_1$ , and rear face,  $v_2$ . This information can then be combined with equation (2.3) to calculate the rate of strain within the specimen:

$$\frac{d\varepsilon(t)}{dt} = \frac{v_1(t) - v_2(t)}{L_s} \quad (2.27)$$

Which can finally be integrated with respect to time to calculate the strain within the specimen,  $\varepsilon(t)$ . Again setting  $x$  equal to  $d$  and taking the inverse transform of equation (2.26), one can also calculate the force on both the front face, F1, and the rear face, F2. This information can then be combined with equation (2.5) to calculate the specimen's average stress.

Before these calculations can be conducted, however, one must first experimentally determine the propagation coefficient values,  $\gamma(\omega)$ , for both the incident and transmission bars. To achieve this characterization on the incident bar, it is positioned away from the transmission bar and impacted with a striker bar (varying lengths are used to assure accurate frequency response characterization). The separation from the transmission bar makes it so that any compressive pulse travelling down the incident bar will be fully reflected as a tensile pulse. This pulse is then recorded as it travels back and forth through the bar (Figure 2-15).

A similar technique is used to characterize the transmission bar. The difference in this case being that the incident and transmission bars are initially placed in contact with one another. This allows the striker pulse to travel through the incident bar and into the transmission bar, where it becomes trapped upon the bars' subsequent separation. The pulse is again recorded as it reflects back and forth within the transmission bar.



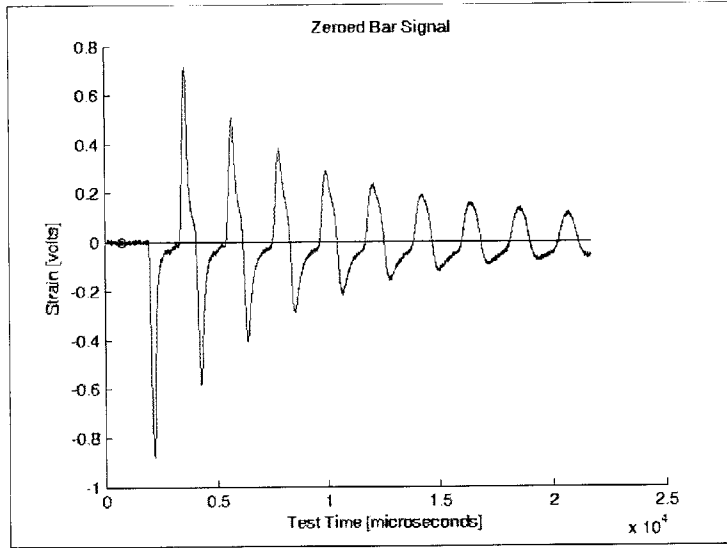


Figure 2-15: Example of a pulse's dispersion and attenuation as it travels back and forth within a PMMA incident bar.

Using the data recorded from these experimental characterization trials, and provided that there is no superpositioning of the waves at the strain gauge location, the Fourier transforms of the first compressive and reflected tensile pulses may be calculated as  $\tilde{\epsilon}_1$  and  $\tilde{\epsilon}_2$ . One may subsequently equate  $\tilde{P}(\omega)$  to  $\tilde{\epsilon}_1$  and  $\tilde{N}(\omega)$  to  $\tilde{\epsilon}_2$  within equation (2.24). Then, because there is no force at the free end of the bar, we can use equation (2.26) to obtain:

$$\tilde{P}(\omega)e^{-\gamma d} + \tilde{N}(\omega)e^{\gamma d} = 0 \quad (2.28)$$

Utilizing this result, we can then define the transfer function,  $H^*(\omega)$ , as follows:

$$H^*(\omega) = -\frac{\tilde{\epsilon}_2(\omega)}{\tilde{\epsilon}_1(\omega)} = e^{-\gamma 2d} \quad (2.29)$$

Finally, from this result it is possible to calculate the propagation coefficient values,  $\gamma(\omega)$ , which in turn enables us to complete all of the subsequent PMMA SHPB calculations of interest.



## Chapter 3

# Experimental Methods

There is still a surprising degree of dissension within the SHPB community as to what is the best method for characterizing soft materials at high strain rates. As such, one of the goals of this thesis was to run trials employing multiple techniques and approaches. It was hoped that by taking this approach we might be able to accelerate the process of establishing a standard SHPB testing procedure. To do so, however, placed some rather stringent requirements upon the materials we could test. Namely, we needed a material that was hard enough to be tested on the solid aluminum bar set-up, yet still soft enough to be tested on the PMMA bar set-up without damaging the system. One of the few biological materials that fits this qualification is trabecular bone. However, because the high rate response of trabecular bone had not yet been well characterized within the literature, and because, as with all biological tissues, its properties can be highly variable, it was decided that a second material was needed to validate the results and assure that the curves obtained on the hollow aluminum and PMMA bars matched those obtained with the more widely accepted solid aluminum bar set-up. To achieve this we chose a polyurea (PU) blend that had already been well characterized within our lab. What follows in this chapter is a description of the two aluminum pressure bar setups, a description of the PMMA pressure bar set-up, and a brief section on the preparation of the PU and trabecular bone specimens.

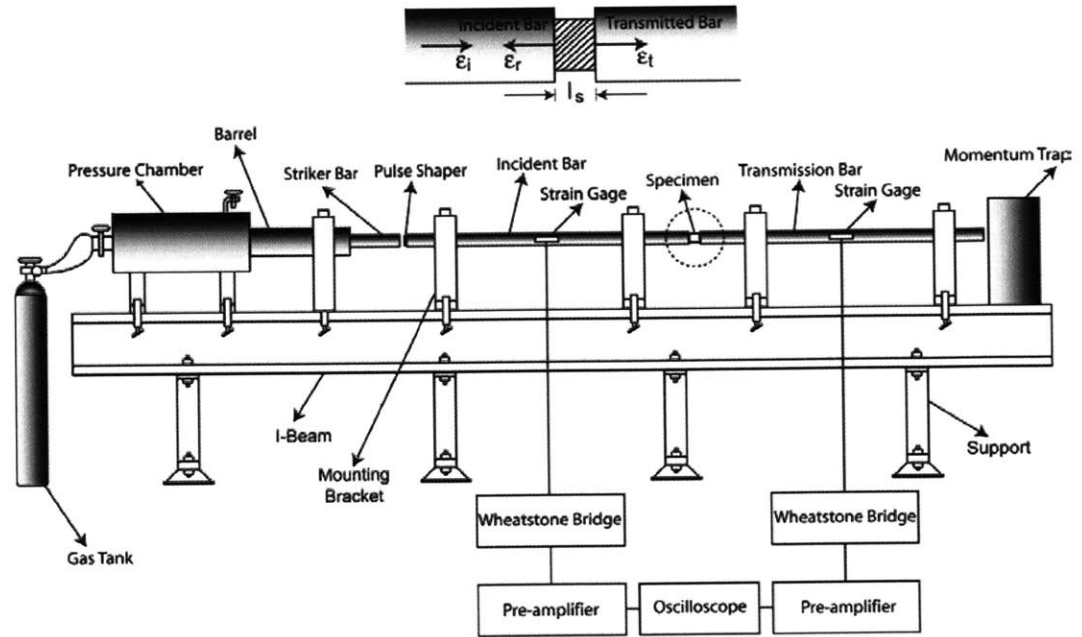


Figure 3-1: Schematic diagram of MIT's split Hopkinson pressure bar facility.

### 3.1 The Aluminum Split-Hopkinson Pressure Bars

Both the solid and the hollow aluminum split-Hopkinson pressure bars used at our facility (Figure 3-1) are composed of 7075 T640 Al, which has a Young's Modulus of 72 GPa and a wave speed of 5090 m/s. The incident and transmission bars are both 3/4" (19.05 mm) in diameter and 90" (2.286 m) in length. The hollow transmission bar has the same exterior dimensions and an internal wall thickness of 1.5 millimeters, giving it an approximately 1:3.5 area ratio with that of the solid transmission bar. The ends of this bar are capped with a solid aluminum plug so as to provide a flat, even contact surface with both the specimen and the momentum trap. Because these plugs have the potential to change the way in which higher frequency components of the stress wave travel, a study was undertaken utilizing the PU samples to see if some form of pulse shaping was necessary to obtain reliable results. Three different approaches were examined: 1) utilizing no pulse shaper, 2) utilizing a thin copper disk measuring 5/16" (7.938 mm) in diameter, and 3) utilizing three sheets of paper held together with a thin layer of Vaseline. The results of this study are presented in Chapter 4, but the

ultimate conclusion was that no pulse shaper is necessary for the frequency components found in our signals. This is most likely due to the fact that our samples have a viscoelastic nature and will therefore dampen any high frequency components before they can be transferred to the transmission bar.

Teflon bearings are used in the supports of the bars to assure the bars moved as freely as possible. The ease of the bars' axial movement is extremely important because any extra resistance from the bearings would alter the shape of the compression and tension pulses traveling along the bar. Also, to satisfy the one-dimensionality assumption, great care was taken in the set-up of the facility to assure near perfect uniaxial alignment amongst the bars. When conducting trials, care is always taken to make sure that the amplitude of the imposed stress pulse does not too closely approach the yield strength of the bars. This is important not only to ensure the longevity of the system, but also because the subsequent data analysis assumes a linear elastic response from the bars.

The strain gauges for both the incident and transmission bars are positioned 30" (0.7620 m) from the specimen interface. This placement dictates the maximum length of striker bar to also be 30" (0.7620 m), but a 19" (0.4826 m) striker bar, also composed of 7075 T640 aluminum, is utilized in this study to assure that there is no overlap between the incident and reflected pulse. In addition, the strain gauges are placed diametrically opposed to one another so as to cancel out the effects any possible bending within the bars. To assure that the strain gauges are an appropriate length to capture all relevant frequency components of the pulse the following formulation was used:

$$L \leq \frac{1}{10f_{\max}} \sqrt{\frac{E}{\rho}} \quad (3.1)$$

where  $L$  is the gauge length,  $f_{\max}$  is the highest significant frequency component,  $E$  is the Young's Modulus of the bar, and  $\rho$  is the density of the bar [13]. Finally, to assure that the electrical signal output by the strain gauges is only due to the changing resistance of the internal monofilament, a small grounding wire is attached to the bar directly in front of the gauge.

The electrical signal from the strain gauges is first transmitted to a Vishay 2100 conditioner/amplifier system, set to a gain of 1000, before it is passed to an oscilloscope to be recorded. The noise produced by activating the solenoid valve to release the striker bar at the start of the trial is approximately 150 mV. As such, the signal capture trigger is set to



Figure 3-2: A Cordin 550 high speed digital camera is used to record the compression of the SHPB samples.

approximately 200 mV. Two different systems are employed depending on the nature of the trial being conducted. Ordinarily, a 1450 CompuScope with a 50 MS/s sampling capacity is utilized because it offers the most user friendly interface and has better resolution than the alternative, a LeCroy Waverunner oscilloscope. The CompuScope model, however, does not have an output trigger, necessary when high speed photographs of the trials are desired. As such, it was decided that most trials for this study would be conducted with the more reliable CompuScope oscilloscope, but that one trial from every group (an example of a group being all PU specimens tested at 30 psi on the solid aluminum SHPB set-up) would be conducted with the LeCroy oscilloscope to enable use of the high speed camera. The camera used to capture the images of sample compression for these trials is a gas turbine drive Cordin model 550 digital camera, capable of capturing 32 frames at rates of up to 200 million frames per second. The camera is outfitted with a Nikon 100 mm / 2.8 macro lens, positioned at the same height and approximately one foot from the specimen (Figure 3-2). A single continuous flash, three milliseconds in duration, is used to illuminate the specimen.

For experiments utilizing either the standard aluminum or hollow aluminum pressure bars, the time and corresponding voltage data from both the incident and transmission bars is saved immediately after each trial in ASCII format. This data is then analyzed using a MATLAB script which implements the theory outlined in Chapter 2. This script, entitled ALSHPB.m, combines Adam Mulliken's hoppy2.m code with insights specifically pertinent to the testing of soft materials. A step by step explanation of this new code can be found in Appendix A, and the code itself can be found in Appendix B.

### 3.2 The PMMA Split-Hopkinson Pressure Bars

The PMMA SHPB set-up is very similar to that of the aluminum bars. The same support structure is used and the bars can be interchanged with the aluminum ones by simply removing the tops of the supports and disconnecting the lead wires connecting the strain gauges to the signal conditioner. The PMMA bars, like the aluminum bars, are 3/4" (0.7620 m) in diameter and 90" (2.286 m) in length. The strain gauges are placed in the same relative position and their connection to the signal conditioner and oscilloscopes are the same as for the aluminum bars. The largest difference, aside from being composed of a different material, is that the PMMA set-up has a variety of striker bars associated with it, ranging in size from just 2" (0.0508 m) to a full 24" (0.6096 m). The shorter bars are used in characterizing the propagation coefficients of the incident and transmission bars, and the longer striker bars are used to obtain varying degrees of strain within the various material specimens. The longest striker bar employed in this study, however, is only 10" (0.2540 m). This is because signal overlapping becomes a significant concern with the longer bars. The data from these trials is once again saved in ASCII format.

For experiments utilizing the aluminum pressure bars the calculations were fairly straightforward. When employing the PMMA bars, however, the analysis becomes more complicated due to polymer's viscoelastic nature. As briefly outlined in the theory section, utilization of the viscoelastic split-Hopkinson pressure bar technique breaks down into two equally important components: (1) characterizing the bars' propagation coefficients,  $\gamma(\omega)$ , and (2) employing these coefficients in the analysis of the stress-strain data collected for individual specimens. Both

tasks are accomplished with MATLAB m-files; the characterization of the bars with a script entitled CHARACTERIZE.m (see Appendix C for a step-by-step explanation and Appendix D for the actual code) and the specimen data analysis with a code designated PMMASHPB.m (see Appendix E for an explanation and Appendix F for the code).

### 3.3 Sample Preparation

Sample preparation is extremely important in this study for two reasons. First, the selection of an appropriate specimen geometry when employing SHPB technique is necessary for accurate results and requires a great deal of attention from the experimentalists. Second, the manner in which both the biological specimens and the tissue simulants are prepared and stored has the potential to greatly affect their mechanical behavior. Hence, proper attention to preparation of the samples was key to obtaining reliable results in this study. The criterion considered and the methods employed will now be reviewed.

With regard to selecting the appropriate specimen geometry for the SHPB tests, it is valuable to first consider what stress, strain, and strain rate range is acceptable or desired. Shorter specimens allow for higher strains and higher strain rates, while decreasing the area of the specimen will clearly increase the stress. In this manner, an experimentalist has some room to move when tailoring his or her experiment. For this study, however, the focus is more on obtaining accurate, reliable results than obtaining results for one specific range of experimental parameters. Bearing this in mind, it is important to remember that the assumption of dynamic equilibrium within the sample is only valid after the pulses has reverberated forward and back three times. The longer the sample, the more time it takes to reach this dynamic equilibrium. Hence, if the initial elastic portion of the specimen's curve is of interest a thinner sample should be used. In addition, samples with a large length-to-diameter (L/D) ratio are at risk for buckling. The sample's length, however, cannot be decreased indefinitely. As the L/D ratio decreases, the effects of both radial inertia and friction become greater, reducing the validity the results. Consequently, it is very important to find the proper L/D ratio; one that enables the sample to quickly reach dynamic equilibrium while also minimizing the effects of friction and radial inertia. For materials with a Poisson ratio of approximately 0.33 and machined





Figure 3-3: Intact bovine femurs are transported to the Orthopedic Biomechanics Laboratory at Beth Israel Deaconess Medical Center for machining.

into a right circular cylinder, E. Davies and S. Hunter theorized longitudinal and radial inertia effects would cancel each other out when the L/D ratio is 0.5 [11]. This ratio is collaborated by the ASM International's current recommendation that SHPB testing specimens maintain an L/D ratio of between 0.5 and 1.0 [20]. Bearing this in mind, it was decided to use a 0.5 L/D ratio for the polyurea (PU) calibration samples. These specimens were prepared utilizing a 7 mm diameter biopsy punch on an approximately 3.5 mm thick sheet of blended PU.

For the trabecular bone samples, however, it was decided to utilize slightly larger L/D ratio; still within the range recommended by the ASM handbooks, but with a diameter of 8mm diameter and a length of slightly less than 8mm. These dimensions were selected so that the samples were large enough to allow a continuum assumption [16], [21], [35].

The manner in which the biological samples are prepared is extremely important because the properties of biological materials can change drastically if not properly looked after. For our study, partially intact cow legs were purchased at Bertolino Beef Co. in Boston, MA and transported to MIT, where they are stored at  $-20^{\circ}\text{C}$  until the time of specimen preparation. The femur from each leg is subsequently removed and transported for machining to Beth Israel Deaconess Medical Center's Orthopedic Biomechanics Laboratory (Figure 3-3).

The femur is first cut through the shaft, perpendicular to the axis, and the distal end is then

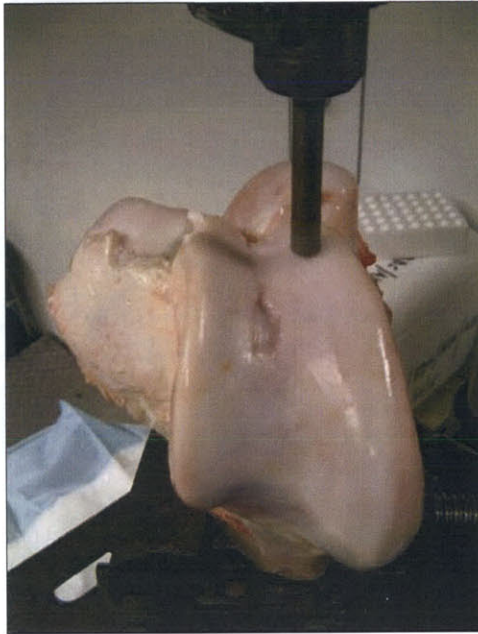


Figure 3-4: The distal end of the femur is clamped in place to be cored with an 8mm diameter diamond masonry bit.

placed vertically into a drill press outfitted with an 8mm diameter diamond coring bit (Figure 3-4). The bone is clamped vertically to reduce vibrations while coring, and to assure that the specimens are cored parallel to the axis of the bone and their principal stress orientation. While coring, the 8mm diameter diamond bit is continuously irrigated and run at a low speed to assure that the bone stays well hydrated and does not burn or fracture [21]. Once the cores are cut, a second cross-sectional cut is made through knee to release them (Figures 3-5 and 3-6). Finally, a low-speed diamond-impregnated wafering saw is used to slice the core samples into cylinders with parallel faces and an approximately 1:1 length to diameter ratio [21] (Figure 3-7). The samples are then massed (to be used later in the calculation of initial density) and frozen at  $-20^{\circ}\text{C}$  in 0.1 M saline to ensure optimal preservation of their mechanical properties [21]. They are stored for a maximum of one month prior to testing and, approximately 24 hours prior to each test, the samples are thawed and stored in a fresh 0.1 M saline solution at  $4^{\circ}\text{C}$ .



Figure 3-5: A cut is made perpendicular to the knee to release the trabecular cores.

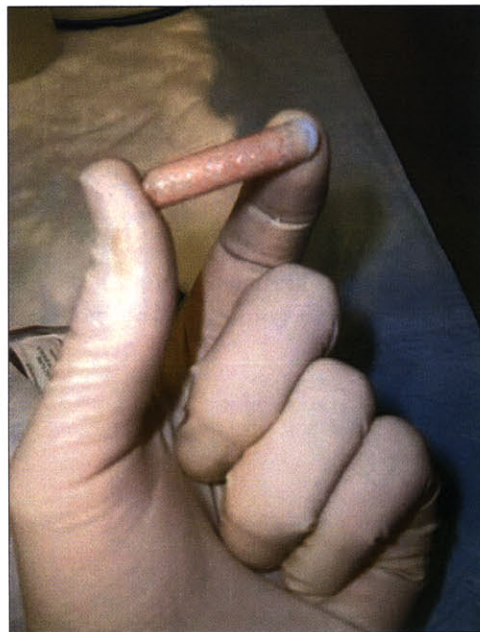


Figure 3-6: A trabecular bone core prior to sectioning.



Figure 3-7: An irrigated diamond encrusted wafering saw is used to section the cores into orthogonal right cylinders.

## Chapter 4

# Results and Discussion

In this chapter the results from the trials on both polyurea (PU) and trabecular bone are presented in graphical form as engineering stress vs. engineering strain plots. For the trials utilizing the solid or hollow aluminum pressure bar set-ups the stress presented is the one wave formulation and the strain presented is the three wave formulation. This approach was employed in order to minimize the noise in the resulting curves. For a more complete explanation of the difference between the two formulations the reader is encouraged to refer to Section 4 of Chapter 2. In addition to the stress vs. strain plots, where trials are labelled according to their respective strain rates, tables are provided to present a summary of the experimental parameters which relate to each individual trial.

The first section of this chapter presents a summary of the trials conducted on a PU blend which had been previously studied by Dr. Jin Yi [34]. The purpose of these trials was to validate the results obtained with the various SHPB techniques employed and illuminate the potential strengths and weaknesses of each technique. This particular PU blend was chosen because it is easy to machine, readily available, and can be tested with all of the techniques we wished to employ in the trabecular bone study. Furthermore, it does not demonstrate significant temperature or age dependence.

The second section in this chapter presents the results obtained on bovine trabecular bone specimens.



Trial #	Approx. Strain Rate	Striker Bar Pressure	Specimen Length	Specimen Diameter	L/D Ratio
1	900 s <sup>-1</sup>	30 psi	3.75 mm	7.50 mm	0.500
2	1000 s <sup>-1</sup>	30 psi	3.70 mm	7.60 mm	0.487
3	975 s <sup>-1</sup>	30 psi	3.70 mm	7.60 mm	0.487
4	980 s <sup>-1</sup>	30 psi	3.87 mm	7.56 mm	0.512
5	900 s <sup>-1</sup>	30 psi	3.87 mm	7.52 mm	0.515
6	1875 s <sup>-1</sup>	60 psi	3.83 mm	7.67 mm	0.499
7	1850 s <sup>-1</sup>	60 psi	3.88 mm	7.65 mm	0.507
8	1900 s <sup>-1</sup>	60 psi	3.80 mm	7.57 mm	0.502
9	1900 s <sup>-1</sup>	60 psi	3.77 mm	7.65 mm	0.493
10	1925 s <sup>-1</sup>	60 psi	3.88 mm	7.56 mm	0.513
11	2400 s <sup>-1</sup>	90 psi	3.87 mm	7.66 mm	0.505
12	2500 s <sup>-1</sup>	90 psi	3.87 mm	7.55 mm	0.513
13	2550 s <sup>-1</sup>	90 psi	3.82 mm	7.68 mm	0.497
14	2550 s <sup>-1</sup>	90 psi	3.80 mm	7.60 mm	0.500
15	2500 s <sup>-1</sup>	90 psi	3.90 mm	7.58 mm	0.515

Table 4.1: Polyurea samples tested with the solid aluminum SHPB set-up.

## 4.1 Polyurea (PU)

### 4.1.1 Solid Aluminum Pressure Bars

The first technique employed in the characterization of the PU blend was the solid aluminum SHPB set-up. This technique was chosen because solid pressure bar systems composed of linear elastic materials, i.e. metals, have been in use since Hopkinson first presented his work nearly a century ago. The technique is well understood and widely accepted, thereby making it an excellent benchmark with which to assess the validity and quality of the results obtained with the less widely accepted hollow bar and polymer bar techniques. The PU trials employing the solid aluminum bar are listed in Table 4.1 and the calculated stress vs. strain curves are presented in Figure 4-1, Figure 4-2, and Figure 4-3. The signals are clearly quite noisy, a consequence of the large impedance mismatch between the PU sample and aluminum bars, but the general shape of the curves is clear and a wide range of strain rates, dependent upon the pressure at which the striker bar was released, is achieved. Finally, a clear dependence upon strain rate can be seen when we plot the average curves from each strain rate regime in Figure 4-4. Error bars have been included at selected strain intervals to denote the standard deviation along each curve.

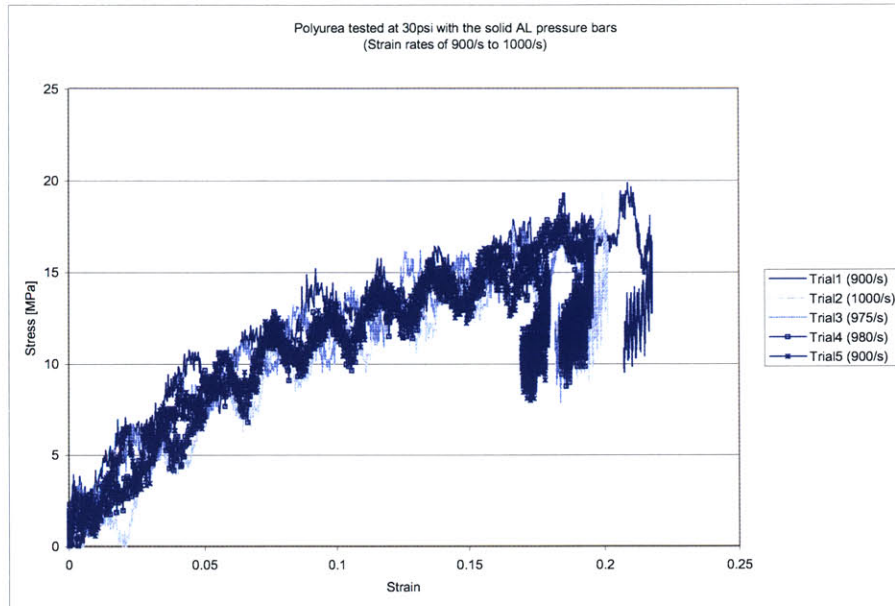


Figure 4-1: Polyurea specimens tested at 30 psi with the solid aluminum SHPB set-up.

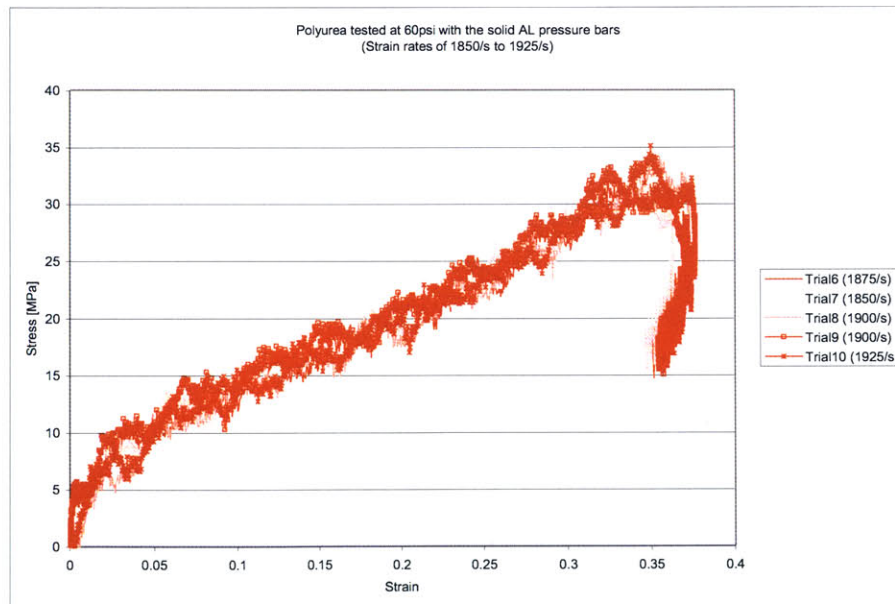


Figure 4-2: Polyurea specimens tested at 60 psi with the solid aluminum SHPB set-up.

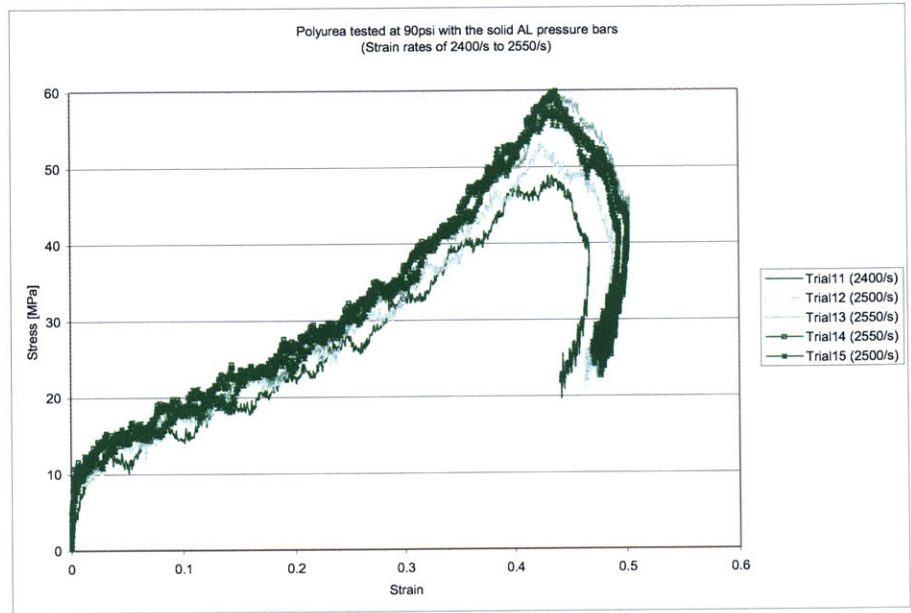


Figure 4-3: Polyurea specimens tested at 90 psi with the solid aluminum SHPB set-up.

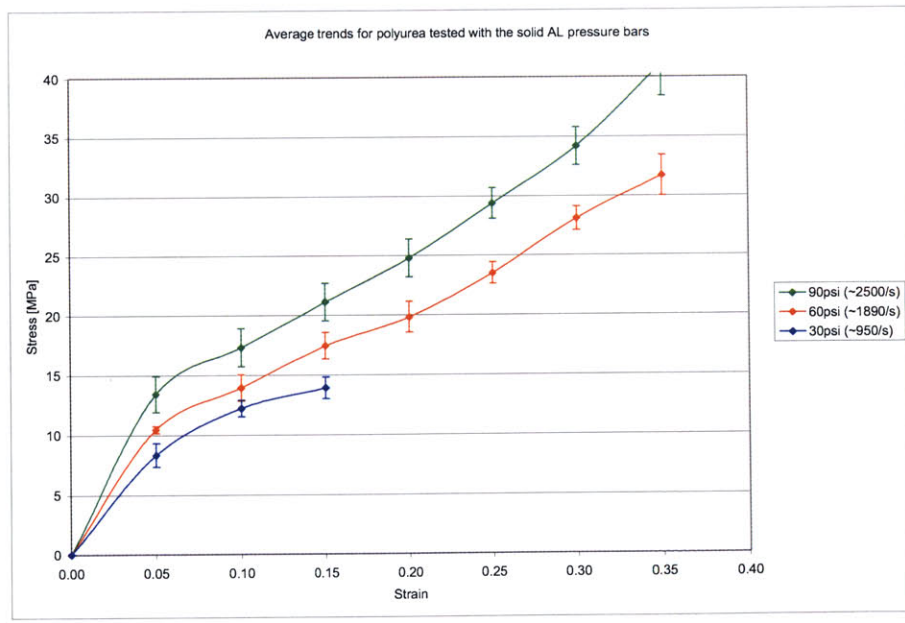


Figure 4-4: Average trends for polyurea tested with the solid aluminum SHPB set-up.



### **4.1.2 Hollow Aluminum Transmission Bar**

The next technique employed, and that which is most closely related to the solid linear elastic pressure bar approach, is the hollow aluminum pressure bar set-up. As discussed in Chapter 2, this technique employs the same basic linear elastic theory, but requires a few slight modifications in the analysis to account for the change in cross sectional area of the transmission bar. In addition, there is cause for concern that high frequency components will be lost or changed as they travel through the capped end of the hollow transmission bar. To assess the degree to which this phenomenon would effect the calculation of results, three different pulse shaping schemes were employed and evaluated: using no pulse shaper at all, utilizing a thin copper disk pulse shaper, and finally employing a series of three paper pulse shapers. The results from each technique are presented and discussed in the three subsequent subsections. Finally, it should be noted that no 90 psi trials were conducted on the hollow aluminum pressure bar set-ups because the resulting stress in the hollow transmission bar was deemed too high for the system. It was feared that the stress would result in inelastic deformation of the bars, not only invalidating the data, but destroying a valuable piece of laboratory equipment.

#### **No Pulse Shaper**

The no pulse shaper approach was the first hollow bar technique to be implemented and ultimately provided the best results. Looking at the resulting curves in Figure 4-5 and Figure 4-6, we can see that the noise is dramatically reduced from that of the trials conducted on the solid aluminum pressure bars. In addition, curve trends and obtained strain rates are nearly identical. Finally, plotting the average trends we clearly see the expected increase in stress corresponding to increasing strain rates (Figure 4-7). Furthermore, the error bars have been decreased dramatically from those encountered with the solid aluminum bar analysis.

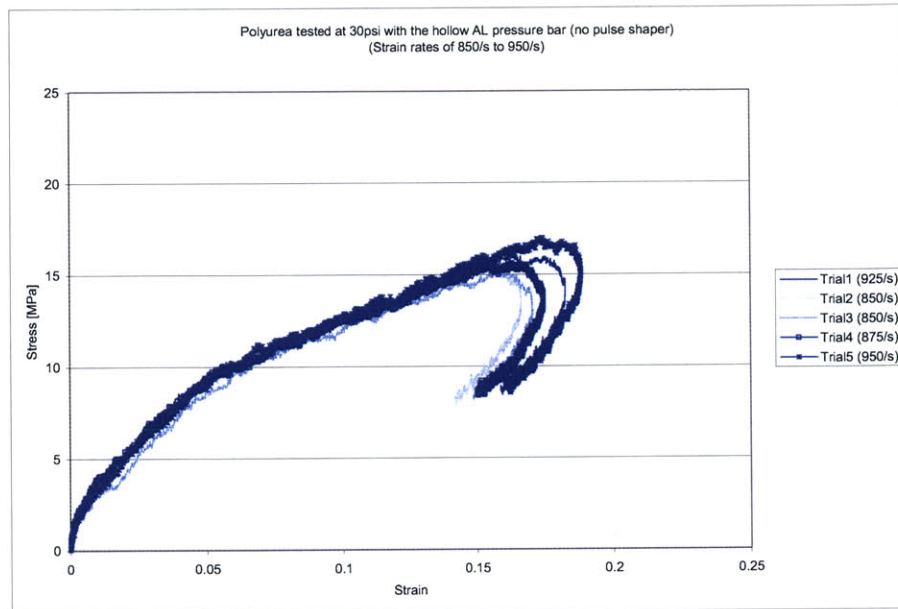


Figure 4-5: Polyurea specimens tested at 30 psi with the hollow aluminum SHPB set-up and no pulse shaper.

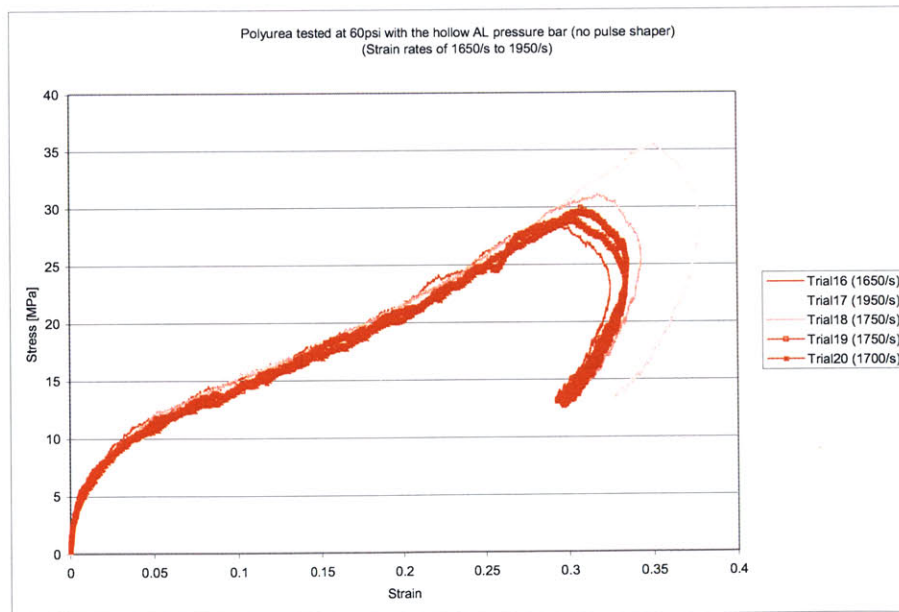


Figure 4-6: Polyurea specimens tested at 60 psi with the hollow aluminum SHPB set-up and no pulse shaper.

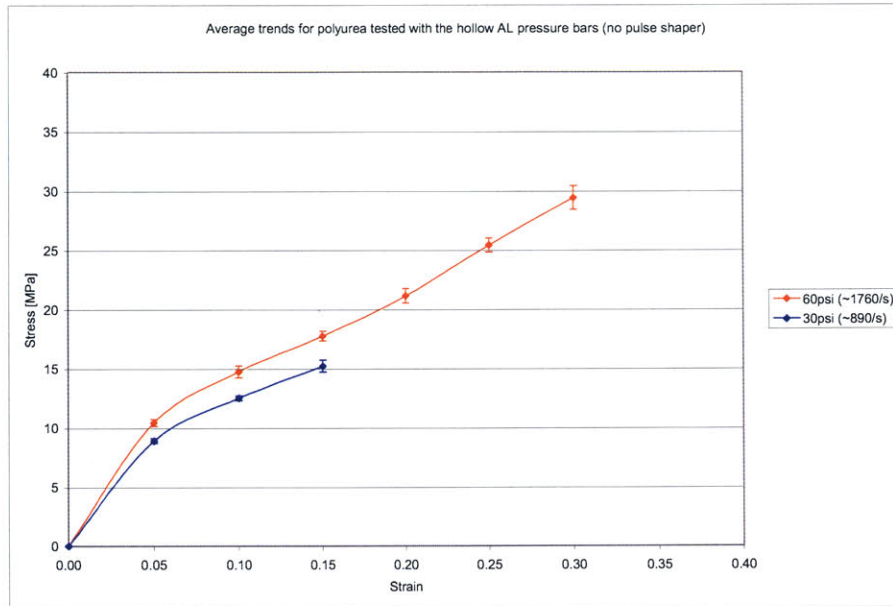


Figure 4-7: Average trends for polyurea tested with the hollow aluminum SHPB set-up and no pulse shaper.

Trial #	Approx. Strain Rate	Striker Bar Pressure	Specimen Length	Specimen Diameter	L/D Ratio
1	925 s <sup>-1</sup>	30 psi	3.75 mm	7.80 mm	0.481
2	850 s <sup>-1</sup>	30 psi	3.87 mm	7.65 mm	0.506
3	850 s <sup>-1</sup>	30 psi	3.91 mm	7.59 mm	0.515
4	875 s <sup>-1</sup>	30 psi	3.83 mm	7.71 mm	0.497
5	950 s <sup>-1</sup>	30 psi	3.45 mm	7.65 mm	0.456
16	1650 s <sup>-1</sup>	60 psi	3.91 mm	7.53 mm	0.519
17	1950 s <sup>-1</sup>	60 psi	3.29 mm	7.72 mm	0.426
18	1750 s <sup>-1</sup>	60 psi	3.89 mm	7.60 mm	0.512
19	1750 s <sup>-1</sup>	60 psi	3.67 mm	7.71 mm	0.476
20	1700 s <sup>-1</sup>	60 psi	3.81 mm	7.61 mm	0.501

Table 4.2: Polyurea samples tested with the hollow aluminum SHPB set-up and no pulse shaper.

Trial #	Approx. Strain Rate	Striker Bar Pressure	Specimen Length	Specimen Diameter	L/D Ratio
11	900 s <sup>-1</sup>	30 psi	3.87 mm	7.44 mm	0.520
12	770 s <sup>-1</sup>	30 psi	3.74 mm	7.66 mm	0.488
13	900 s <sup>-1</sup>	30 psi	3.63 mm	7.64 mm	0.474
14	725 s <sup>-1</sup>	30 psi	3.62 mm	7.61 mm	0.476
15	700 s <sup>-1</sup>	30 psi	3.84 mm	7.68 mm	0.500
26	1625 s <sup>-1</sup>	60 psi	3.87 mm	7.62 mm	0.508
27	1600 s <sup>-1</sup>	60 psi	3.89 mm	7.6 mm	0.508
28	1750 s <sup>-1</sup>	60 psi	3.54 mm	7.64 mm	0.463
29	1625 s <sup>-1</sup>	60 psi	3.83 mm	7.68 mm	0.499
30	1600 s <sup>-1</sup>	60 psi	3.89 mm	7.60 mm	0.512

Table 4.3: Polyurea samples tested with the solid aluminum SHPB set-up and a copper pulse shapper.

### Copper Pulse Shaper

The next hollow bar approach evaluated, and the second most successful, employed a thin copper disk as the pulse shaper. Examining Figure 4-8, Figure 4-9, and Figure 4-10 we can see the noise of the resulting plots is again dramatically reduced from that encountered in the solid aluminum pressure bar trials, and we are again able to achieve a wide range of strain rates. The average curves for this approach also show the same strain rate dependence trend. Utilizing this approach, however, we see that the results for the 30 psi, low pressure trials are not as consistent as those obtained without a pulse shaper; in fact, two of the trials substantially deviate from the previous obtained curves (compare Figure 4-8 to Figure 4-1 and Figure 4-5).

Also, while the rise time of the pulse was noticeable increased, the calculated frequency spectrum of the transmission pulse was not appreciably effected. The aim of pulse shaping in this approach is to eliminate additional high frequency components in the transmission signal that might be subsequently affected by the hollow bar cap. Since this aim was not achieved by the copper pulse shaper, it was deemed inferior to the technique of using no pulse shaper (which also obtained more consistent results).

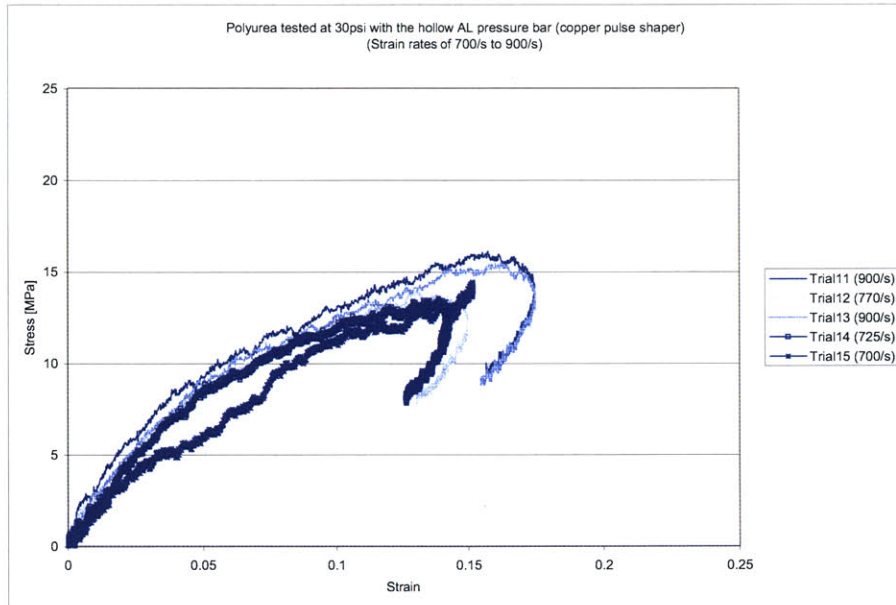


Figure 4-8: Polyurea specimens tested at 30 psi with the hollow aluminum SHPB set-up and a copper pulse shaper.

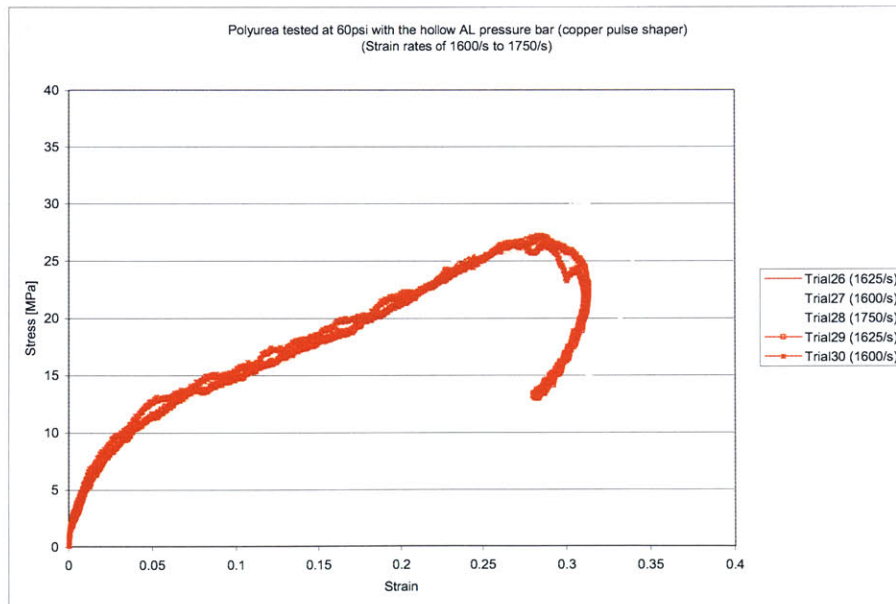


Figure 4-9: Polyurea specimens tested at 60 psi with the hollow aluminum SHPB set-up and a copper pulse shaper.

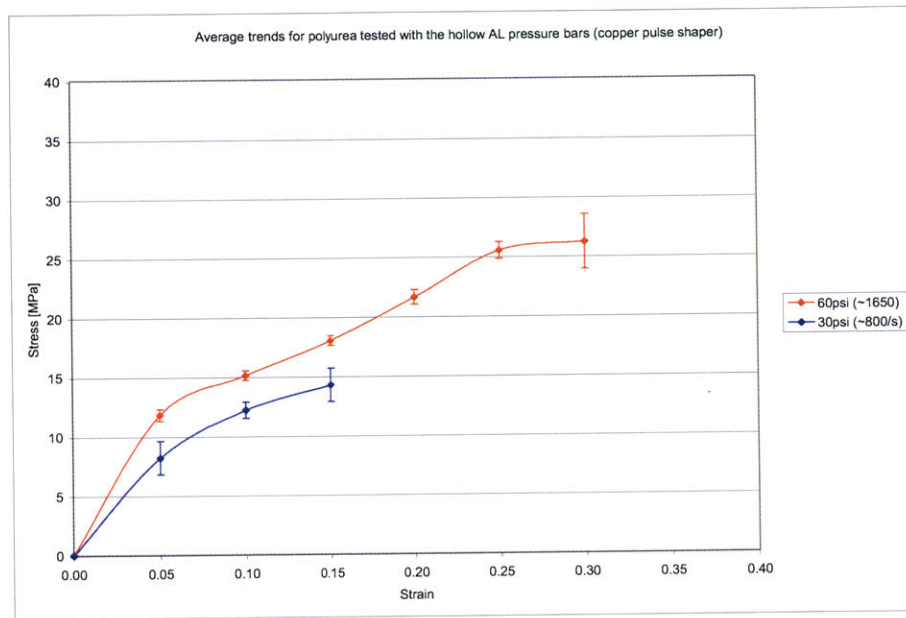


Figure 4-10: Average trends for polyurea tested with the hollow aluminum SHPB set-up and a copper pulse shaper.

## Paper Pulse Shaper

The paper pulse shaping approach was the last hollow bar technique evaluated and the least successful of the three. The resulting stress vs. strain plots, seen in Figure 4-11 and Figure 4-12, are again less noisy than the results obtained with the solid aluminum pressure bar set-up, and again provide a wide range of strain rates. Similar to the copper pulse shaper approach, however, we again see several 30psi, low pressure trials that are inconsistent and significantly deviate from the previously obtained curves. A probable explanation for this phenomenon is that the increased rise time resulting from these two pulse shaping approaches increased the difficulty in isolating the start of the incident and reflected pulses. This difficulty was certainly a factor when trying to match the force balance during the analysis of the paper pulse shaping approach. This type of error in isolating the pulses would have then carried through in the subsequent calculations of stress and strain.

Another problem with the paper pulse shaping approach was that the rise time was increased so dramatically that many trials never reached a constant strain rate. Rather, the rate slowly rose to a maximum then slowly decreased back to zero. Ideally, a constant strain rate should be obtained as quickly as possible and maintained as long as possible to ease subsequent data analysis.

Despite the difficulty in obtaining a constant strain rate, the curves for the average trends still show a recognizable dependence upon strain rate (Figure 4-13). Due to the inconsistencies at low pressures, however, and the fact that neither pulse shaping approach appreciably changed the frequency spectrum of the transmission pulse, it was decided that pulse shaping was not required to avoid attenuation due to the cap in the hollow bar. Therefore, future trials utilizing the hollow bar set-up, specifically those on trabecular bone, were conducted without the added complexity of employing pulse shaping approaches.

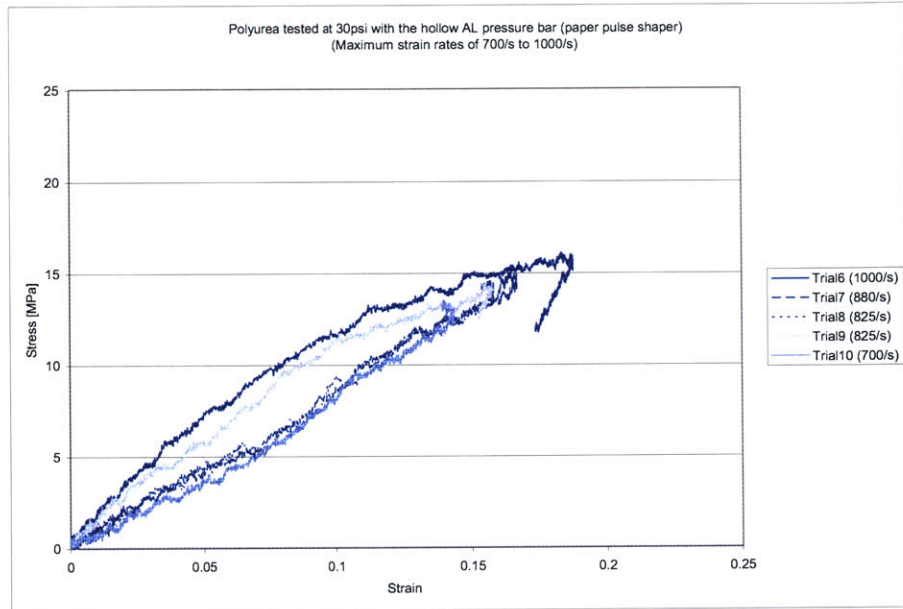


Figure 4-11: Polyurea specimens tested at 30 psi with the hollow aluminum SHPB set-up and a paper pulse shaper.

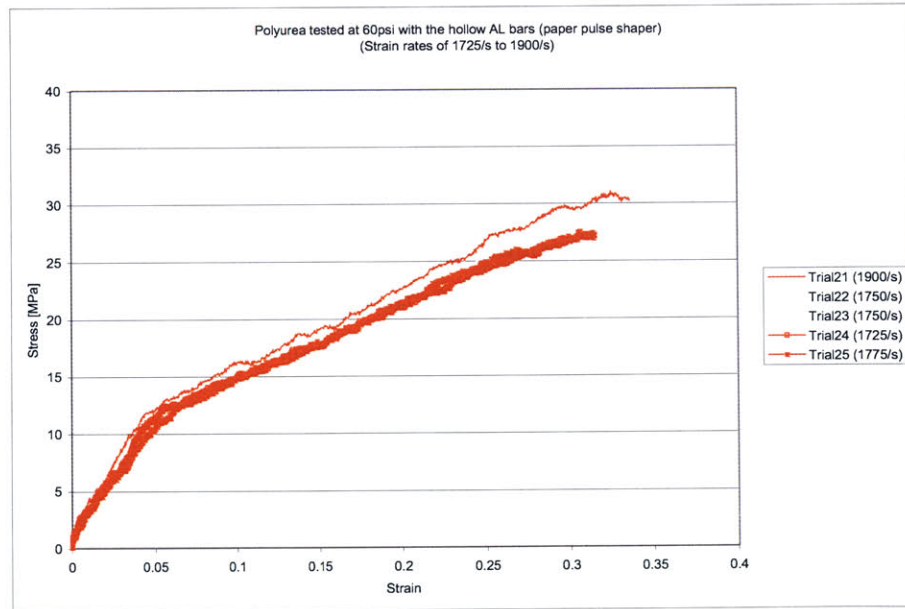


Figure 4-12: Polyurea specimens tested at 60 psi with the hollow aluminum SHPB set-up and a paper pulse shaper.



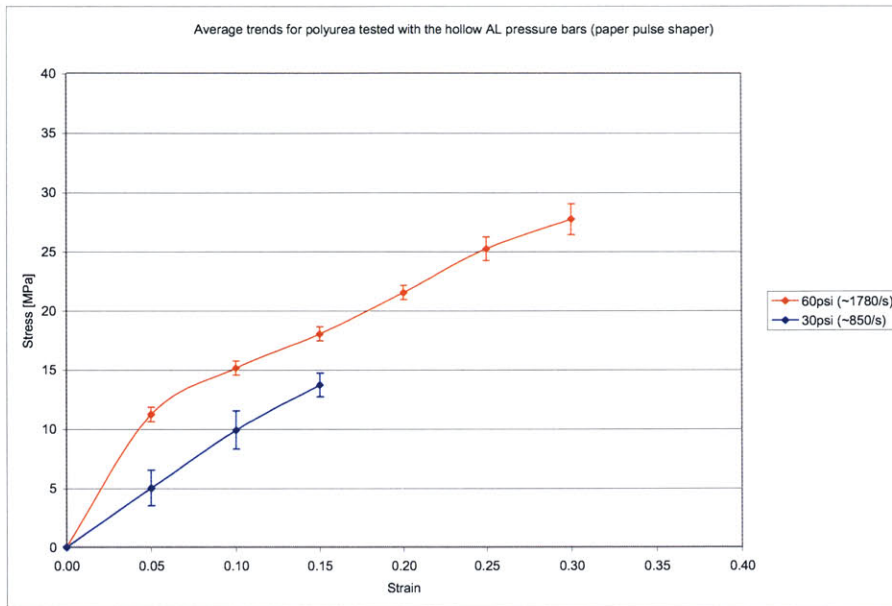


Figure 4-13: Average trends for polyurea tested with the hollow aluminum SHPB set-up and a paper pulse shaper.

Trial #	Approx. Strain Rate	Striker Bar Pressure	Specimen Length	Specimen Diameter	L/D Ratio
6	1000 s <sup>-1</sup>	30 psi	3.45 mm	7.65 mm	0.451
7	880 s <sup>-1</sup>	30 psi	3.79 mm	7.55 mm	0.502
8	825 s <sup>-1</sup>	30 psi	3.90 mm	7.65 mm	0.510
9	825 s <sup>-1</sup>	30 psi	3.90 mm	7.64 mm	0.507
10	700 s <sup>-1</sup>	30 psi	3.58 mm	7.68 mm	0.466
21	1900 s <sup>-1</sup>	60 psi	3.55 mm	7.51mm	0.473
22	1750 s <sup>-1</sup>	60 psi	3.75 mm	7.55 mm	0.497
23	1750 s <sup>-1</sup>	60 psi	3.91 mm	7.61mm	0.514
24	1725 s <sup>-1</sup>	60 psi	3.91 mm	7.65 mm	0.511
25	1775 s <sup>-1</sup>	60 psi	3.63 mm	7.58 mm	0.479

Table 4.4: Polyurea samples tested with the solid aluminum SHPB set-up and a paper pulse shaper.

### 4.1.3 PMMA Pressure Bars

The final technique employed in the investigation on PU was the use of polymeric, namely PMMA, pressure bars. For this technique two different approaches were employed. The first was with a 10" (0.2540 m) PMMA striker bar (Trials 1-6), and the second with a 6" (0.1524 m) PMMA striker bar (Trials 7-12). The 10" striker bar was chosen because preliminary calculations indicated that it would be the longest bar that could safely be employed without incurring signal overlap between the incident and reflected pulses. During the analysis, however, it became apparent that at low rates the 10" striker was too long and some degree of signal interference was noted due to dispersion within the incident bar. This difficulty explains the inconsistent results seen in Trials 1 thru 3 of Figure 4-14. A 6" striker bar was therefore subsequently employed to ensure the availability of low pressure trial data without signal overlap. With this information in mind, subsequent trials on trabecular bone, to be discussed in the next section, would employ a 6" PMMA striker and an 8" PMMA striker.

As seen in Figure 4-14 and Figure 4-15, the PMMA SHPB technique gave excellent noise reduction compared to the solid aluminum pressure bar technique and allowed for a comparable range of strain rates compared to the various hollow aluminum bar techniques. Similar to the hollow bar technique, the limit on striker bar pressure was set to 60 psi so as to avoid permanent deformation of the bars. It is worth noting that one added advantage of the PMMA bar approach was that it allowed for much more accurate and prolonged calculations of the specimens' unloading behavior. Average curves for the techniques are shown with error bars in Figure 4-16.

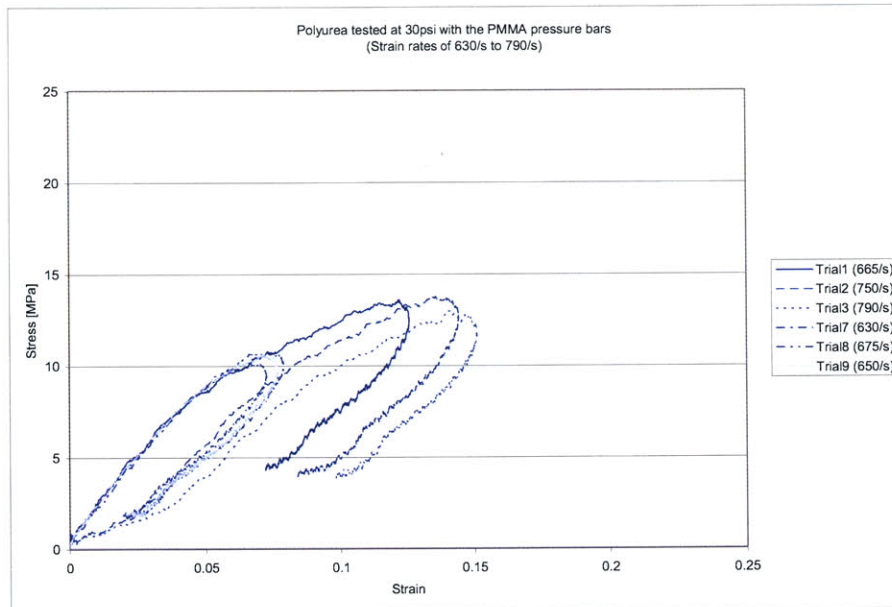


Figure 4-14: Polyurea specimens tested at 30 psi with the PMMA SHPB set-up and either a 6" or 10" striker.

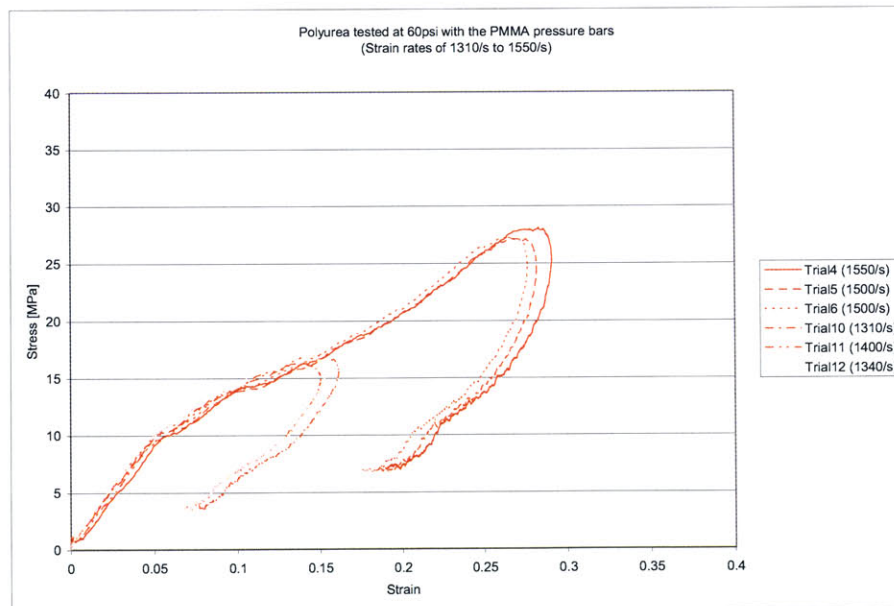


Figure 4-15: Polyurea specimens tested at 60 psi with the PMMA SHPB set-up and either a 6" or 10" striker.

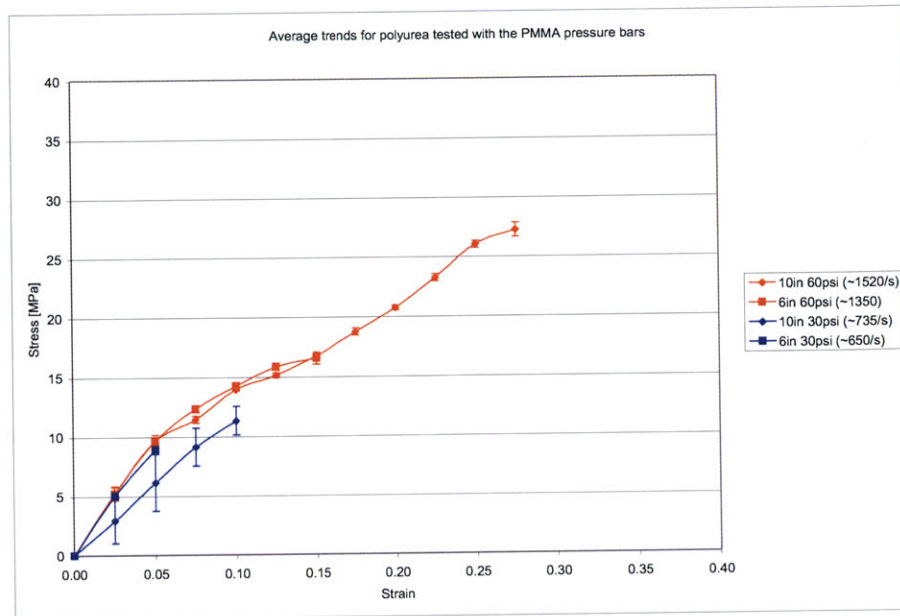


Figure 4-16: Average trends for polyurea tested with the PMMA SHPB set-up.

Trial #	Approx. Strain Rate	Striker Bar Pressure	Striker Bar Length	Specimen Length	Specimen Diameter	L/D Ratio
1	665 s <sup>-1</sup>	30 psi	0.2540 m	3.85 mm	6.85 mm	0.562
2	750 s <sup>-1</sup>	30 psi	0.2540 m	3.82 mm	6.77 mm	0.564
3	790 s <sup>-1</sup>	30 psi	0.2540 m	3.76 mm	6.85 mm	0.549
4	1500 s <sup>-1</sup>	60 psi	0.2540 m	3.71 mm	6.80 mm	0.546
5	1500 s <sup>-1</sup>	60 psi	0.2540 m	3.60 mm	6.78 mm	0.531
6	1500 s <sup>-1</sup>	60 psi	0.2540 m	3.49 mm	6.79 mm	0.514
7	630 s <sup>-1</sup>	30 psi	0.1524 m	3.87 mm	7.55 mm	0.512
8	675 s <sup>-1</sup>	30 psi	0.1524 m	3.76 mm	7.46 mm	0.504
9	650 s <sup>-1</sup>	30 psi	0.1524 m	3.83 mm	7.54 mm	0.508
10	1310 s <sup>-1</sup>	60 psi	0.1524 m	3.84 mm	7.52 mm	0.511
11	1400 s <sup>-1</sup>	60 psi	0.1524 m	3.78 mm	7.55 mm	0.501
12	1340 s <sup>-1</sup>	60 psi	0.1524 m	3.80 mm	7.60 mm	0.500

Table 4.5: Polyurea samples tested with the PMMA SHPB set-up.

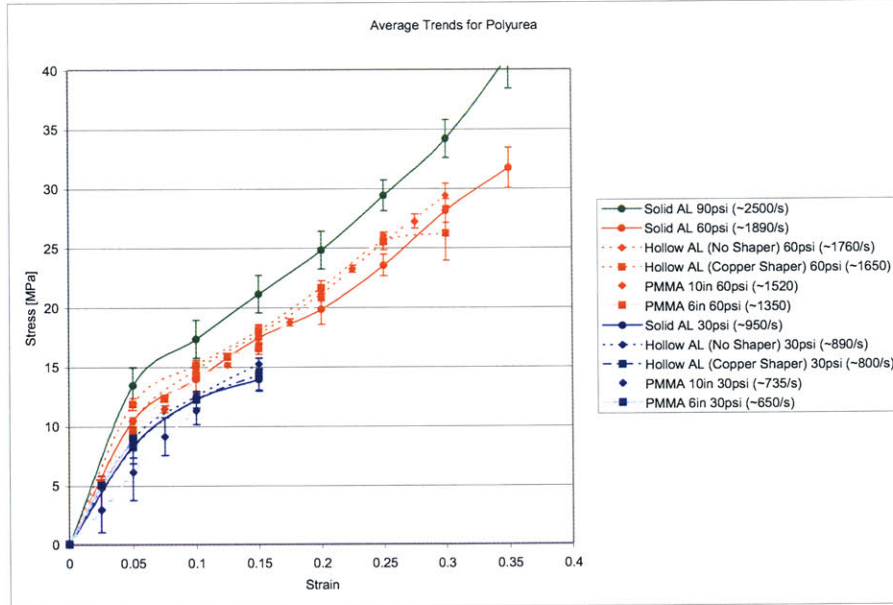


Figure 4-17: Summary of all polyurea results.

#### 4.1.4 Polyurea (PU) Analysis Summary

Finally, to show that all of the techniques employed in this study do indeed provide comparable results, the average trends for each testing configuration have been plotted overlying one another in Figure 4-17. The error bars for each curve in this figure are representative of one standard deviation.

## 4.2 Trabecular Bone

Having selected and validated the relevant SHPB techniques, we now turn our attention to applying these procedures to the characterization of trabecular bone. Provided in this section are the results, presented in the form of an engineering stress vs. engineer strain plot, for the three selected techniques: the solid aluminum pressure bar set-up, the hollow aluminum pressure bar set-up (without pulse shaping), and the PMMA pressure bar set-up (with both a 6" and an 8" striker bar configuration). For each set of plots a table is given to provide the reader with the pertinent experimental parameters. Four trials were conducted on each set-up

at striker bar pressures of 20 psi, 40 psi, and 60 psi. In order to assure that the deformation for each method and each pressure was uniform, and to check that localized failure was not occurring, one of these four trials was always conducted utilizing the high speed camera set-up described in the experimental methods section.

#### 4.2.1 Solid Aluminum Pressure Bars

Figure 4-19, Figure 4-20, and Figure 4-21 provide the results for the trials employing the solid aluminum SHPB set-up. Figure 4-22 then summarizes the average trends for each of these three different strain rate regimes. The reader should note, however, that the fourth trial from each regime, indicated by "\*" in Table 4.6 and representing the trial in which high speed photography was employed (see Figure 4-18), was excluded from the averages because of the low resolution (and consequently large amount of noise) in the signal acquisition set-up. For the purposes of consistency, this convention is maintained throughout the subsequent hollow bar and PMMA bar analyses as well.

The strain obtained in each of the solid aluminum bar trials was between 0.35 and 0.70, well beyond the strains obtained by the previous high rate study on cortical bone by McElhaney [24]. Significant also was the range of strain rates achieved, between  $250 \text{ s}^{-1}$  and  $1300 \text{ s}^{-1}$ . It is interesting to note, however, that the curves of the highest rate trials with this solid aluminum bar technique, corresponding to a 60 psi striker bar pressure, fall below the curves of both the 20 psi and 40 psi trials. This deviation seems counter-intuitive and furthermore does not correspond to the trends seen in the results of the other SHPB techniques. This may, however, simply be due to the small sample size of the group. Also, it should be noted that these curves do not take into account the effect of apparent density, and it is possible that doing so would subsequently raise the 60 psi curve relative to the others. Unfortunately, many of the samples recovered after the trials were too far damaged to allow for accurate measurement of the demarrowed mass. This is evident in Table 4.6 by the appearance of an "N/A" entry in the apparent density column (a potential solution to this problem will be discussed in Chapter 5). Finally, this unexpected deviation may simply be indicative of the problems which arise from the solid aluminum bar's low signal-to-noise ratio (further evidence of the need to employ lower impedance bars).



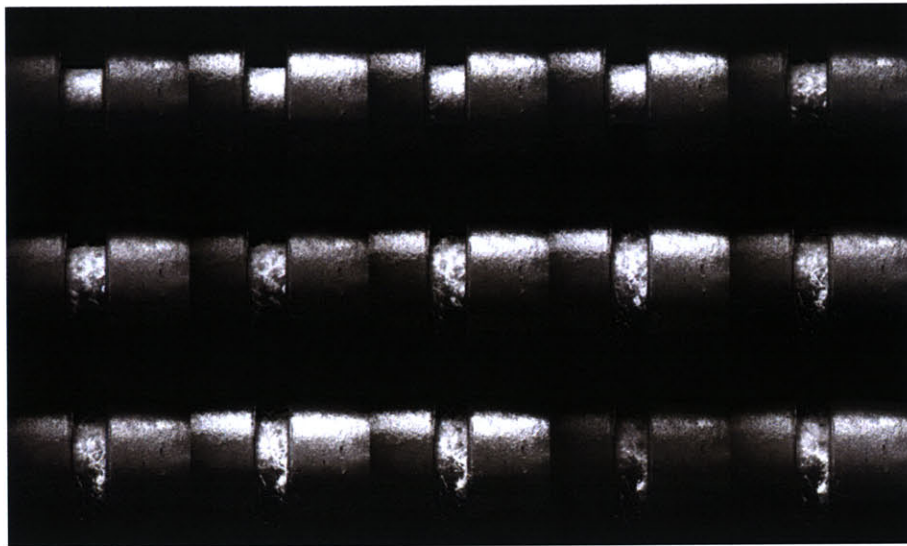


Figure 4-18: Select trials were conducted utilizing high speed photography. Seen here is a 60 psi trial on the solid aluminum SHPB in which the marrow can clearly be seen squeezing out from within the trabeculae.

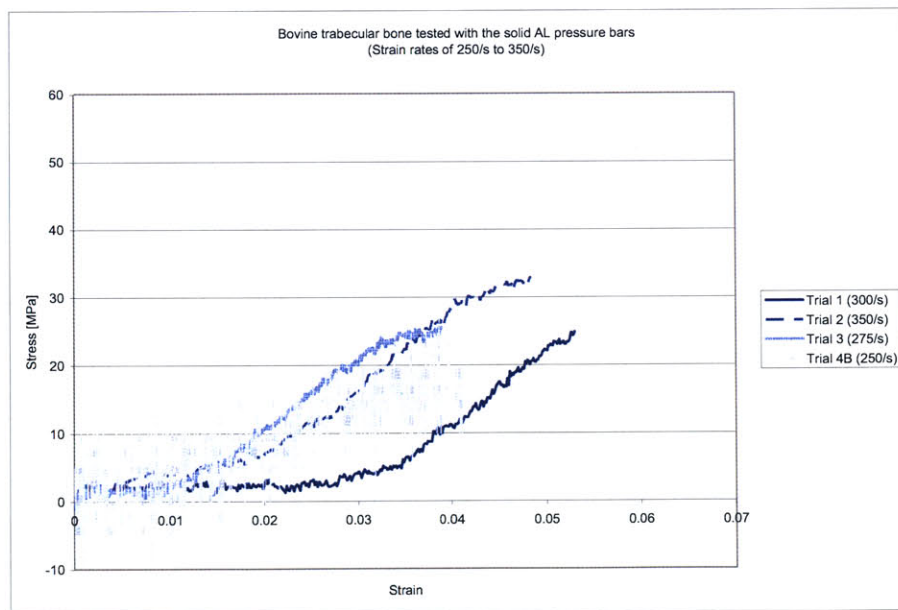


Figure 4-19: Bovine trabecular bone specimens tested at 20 psi with the solid aluminum SHPB set-up.

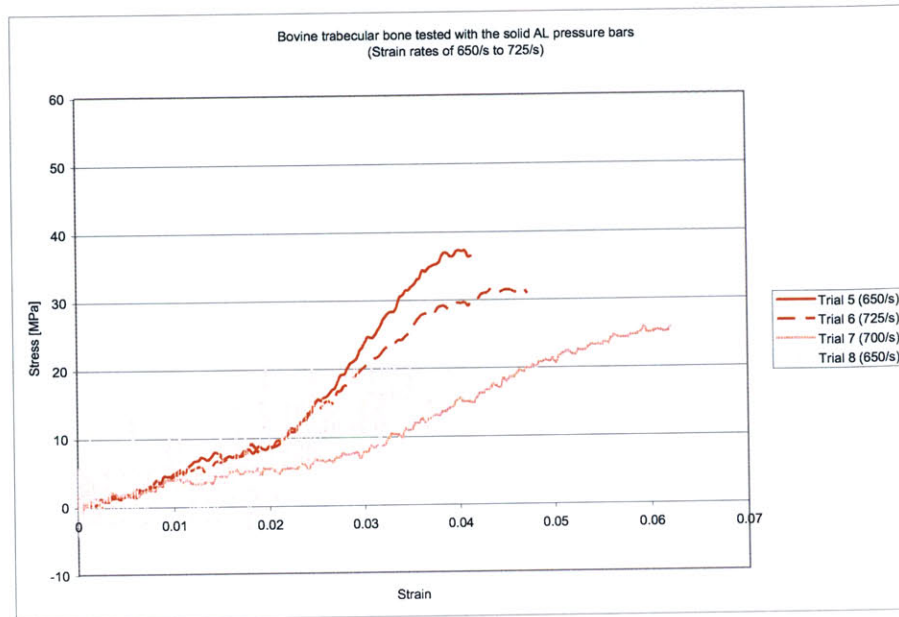


Figure 4-20: Bovine trabecular bone specimens tested at 40 psi with the solid aluminum SHPB set-up.

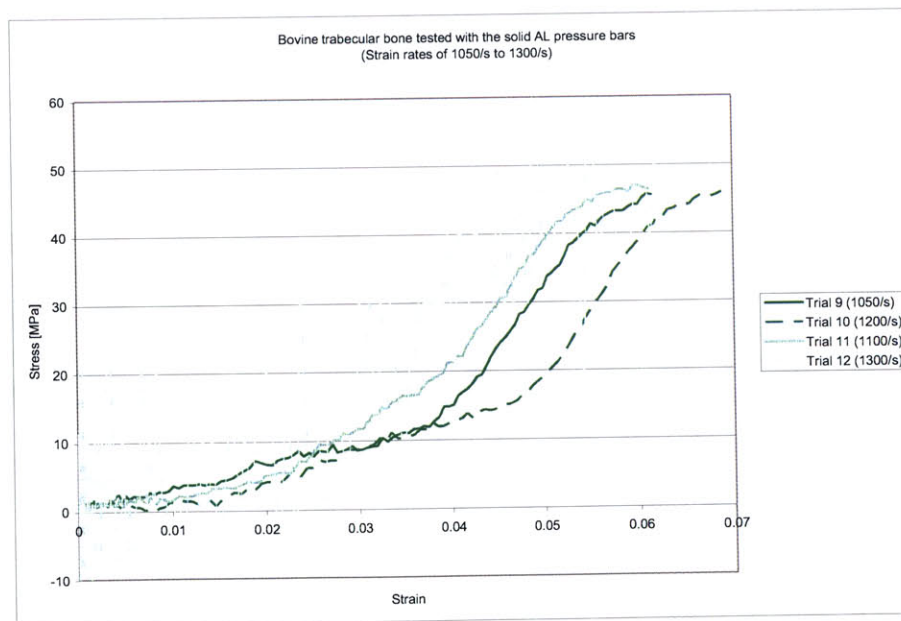


Figure 4-21: Bovine trabecular bone specimens tested at 60 psi with the solid aluminum SHPB set-up.



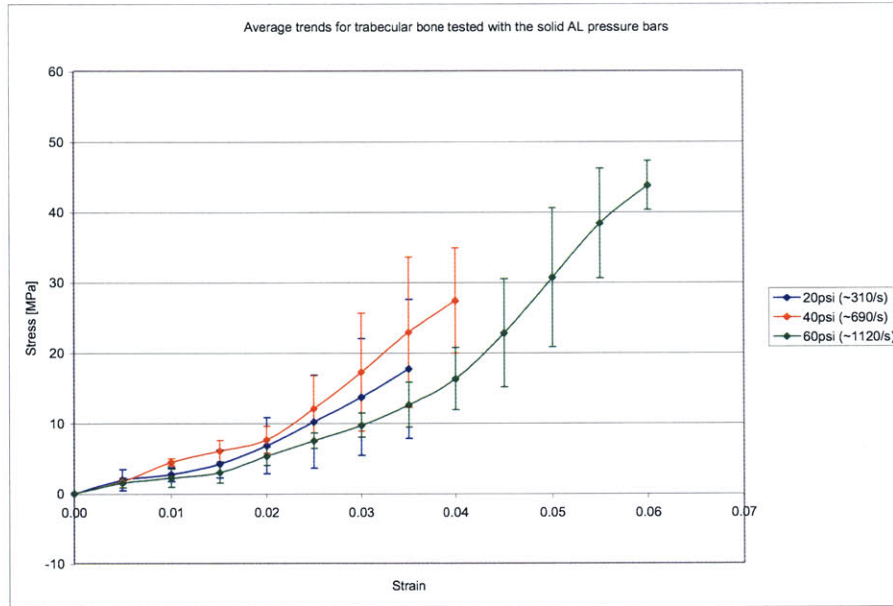


Figure 4-22: Average trends for bovine trabecular bone samples tested with the solid aluminum SHPB set-up.

Trial #	Approx. Strain Rate	Striker Bar Pressure	Specimen Length	Specimen Diameter	Initial Density	Apparent Density
1	300 s <sup>-1</sup>	20 psi	6.60 mm	8.11 mm	1339 kg/m <sup>3</sup>	898 kg/m <sup>3</sup>
2	350 s <sup>-1</sup>	20 psi	5.34 mm	8.07 mm	1386 kg/m <sup>3</sup>	1006 kg/m <sup>3</sup>
3	275 s <sup>-1</sup>	20 psi	7.73 mm	8.07 mm	1367 kg/m <sup>3</sup>	800 kg/m <sup>3</sup>
4*	N/A <sup>T</sup>	20 psi	6.45 mm	8.10 mm	1331 kg/m <sup>3</sup>	846 kg/m <sup>3</sup>
4B*	250 s <sup>-1</sup>	20 psi	7.31 mm	8.07 mm	1286 kg/m <sup>3</sup>	N/A
5	650 s <sup>-1</sup>	40 psi	7.09 mm	8.07 mm	1350 kg/m <sup>3</sup>	N/A
6	725 s <sup>-1</sup>	40 psi	6.42 mm	8.07 mm	1350 kg/m <sup>3</sup>	N/A
7	700 s <sup>-1</sup>	40 psi	6.41 mm	8.06 mm	1343 kg/m <sup>3</sup>	N/A
8*	650 s <sup>-1</sup>	40 psi	7.78 mm	8.08 mm	1281 kg/m <sup>3</sup>	N/A
9	1050 s <sup>-1</sup>	60 psi	6.56 mm	8.05 mm	1384 kg/m <sup>3</sup>	N/A
10	1200 s <sup>-1</sup>	60 psi	5.76 mm	8.11 mm	1371 kg/m <sup>3</sup>	N/A
11	1100 s <sup>-1</sup>	60 psi	5.98 mm	8.11 mm	1408 kg/m <sup>3</sup>	N/A
12*	1300 s <sup>-1</sup>	60 psi	5.60 mm	8.14 mm	1394 kg/m <sup>3</sup>	N/A
<b>Average</b>			6.54 mm	8.09 mm	1353 kg/m <sup>3</sup>	877 kg/m <sup>3</sup>
<b>Standard Deviation</b>			0.77 mm	0.03 mm	38.5 kg/m <sup>3</sup>	88.5 kg/m <sup>3</sup>
* Trial employing high speed photography (not included in the average trends).						
<sup>T</sup> No transmission signal was recorded for this trial						

Table 4.6: Bovine trabecular bone samples tested with the solid aluminum SHPB.

Trial #	Approx. Strain Rate	Striker Bar Pressure	Specimen Length	Specimen Diameter	Initial Density	Apparent Density
1	350 s <sup>-1</sup>	20 psi	5.80 mm	8.10 mm	1405 kg/m <sup>3</sup>	1090 kg/m <sup>3</sup>
2	300 s <sup>-1</sup>	20 psi	6.02 mm	8.06 mm	1392 kg/m <sup>3</sup>	824 kg/m <sup>3</sup>
3	250 s <sup>-1</sup>	20 psi	6.77 mm	8.04 mm	1325 kg/m <sup>3</sup>	731 kg/m <sup>3</sup>
4*	275 s <sup>-1</sup>	20 psi	6.77 mm	8.09 mm	1361 kg/m <sup>3</sup>	863 kg/m <sup>3</sup>
5	700 s <sup>-1</sup>	40 psi	6.01 mm	8.08 mm	1393 kg/m <sup>3</sup>	N/A
6	650 s <sup>-1</sup>	40 psi	7.19 mm	8.08 mm	1262 kg/m <sup>3</sup>	N/A
7	600 s <sup>-1</sup>	40 psi	7.16 mm	8.08 mm	1314 kg/m <sup>3</sup>	N/A
8*	550 s <sup>-1</sup>	40 psi	8.08 mm	9.09 mm	1117 kg/m <sup>3</sup>	N/A
9	700 s <sup>-1</sup>	60 psi	7.75 mm	8.10 mm	1340 kg/m <sup>3</sup>	N/A
10	1000 s <sup>-1</sup>	60 psi	6.14 mm	8.06 mm	1435 kg/m <sup>3</sup>	N/A
11	750 s <sup>-1</sup>	60 psi	7.50 mm	8.04 mm	1412 kg/m <sup>3</sup>	N/A
12*	N/A <sup>R</sup>	60 psi	6.12 mm	8.10 mm	1381 kg/m <sup>3</sup>	N/A
<b>Average</b>			6.78 mm	8.07 mm	1345 kg/m <sup>3</sup>	877 kg/m <sup>3</sup>
<b>Standard Deviation</b>			0.77 mm	0.03 mm	86.6 kg/m <sup>3</sup>	152.4 kg/m <sup>3</sup>
* Trial employing high speed photography (not included in the average trends).						
<sup>R</sup> Signal was not captured properly due to an improper trigger.						

Table 4.7: Bovine trabecular bone samples tested with hollow aluminum SHPB.

#### 4.2.2 Hollow Aluminum Transmission Bar

Figure 4-23, Figure 4-24, and Figure 4-25 of this subsection provide the results for the trials employing the hollow aluminum SHPB set-up. The strains and strain rates obtained here are comparable to those seen in the solid aluminum SHPB trials, but the standard deviation amongst the results has been reduced slightly. This trend is best seen in Figure 4-22, which summarizes the average trends for each of these three different strain rate regimes. Also, the average stress-strain curves here show the anticipated increase in stress corresponding to an increase in strain rate, which was not the case in the solid aluminum bar study. Unfortunately, because many of the samples recovered were significantly damaged, not enough apparent density data could be gathered to study its effect upon these curves.

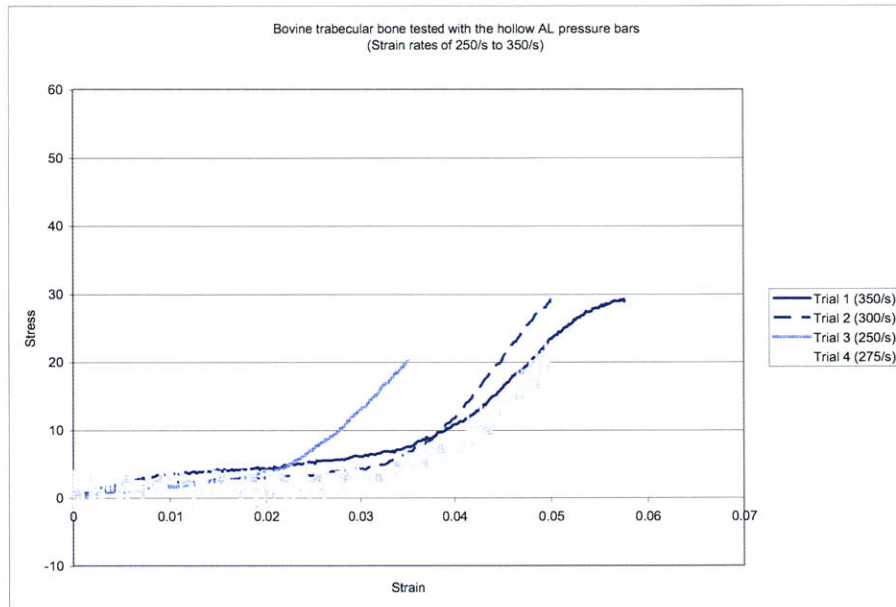


Figure 4-23: Bovine trabecular bone specimens tested at 20 psi with the hollow aluminum SHPB set-up.

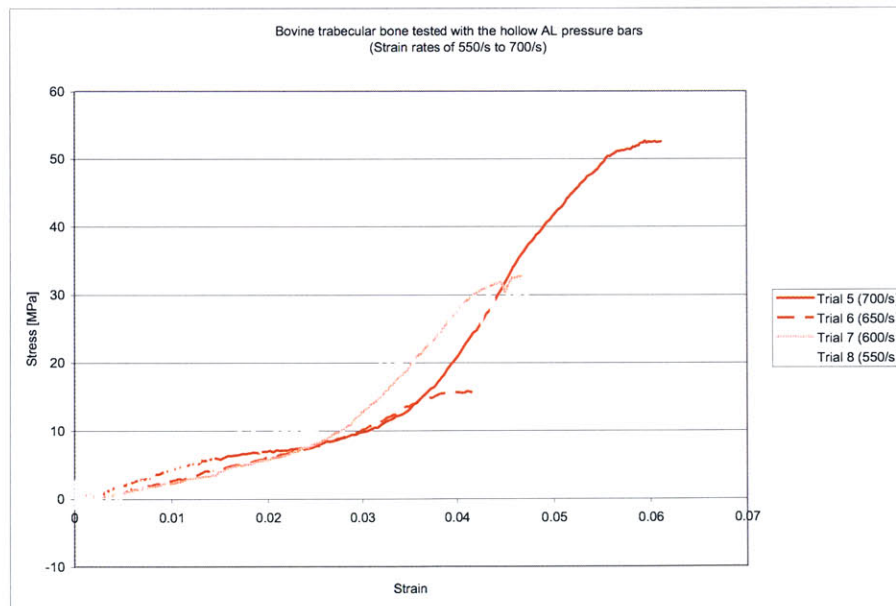


Figure 4-24: Bovine trabecular bone specimens tested at 40 psi with the hollow aluminum SHPB set-up.

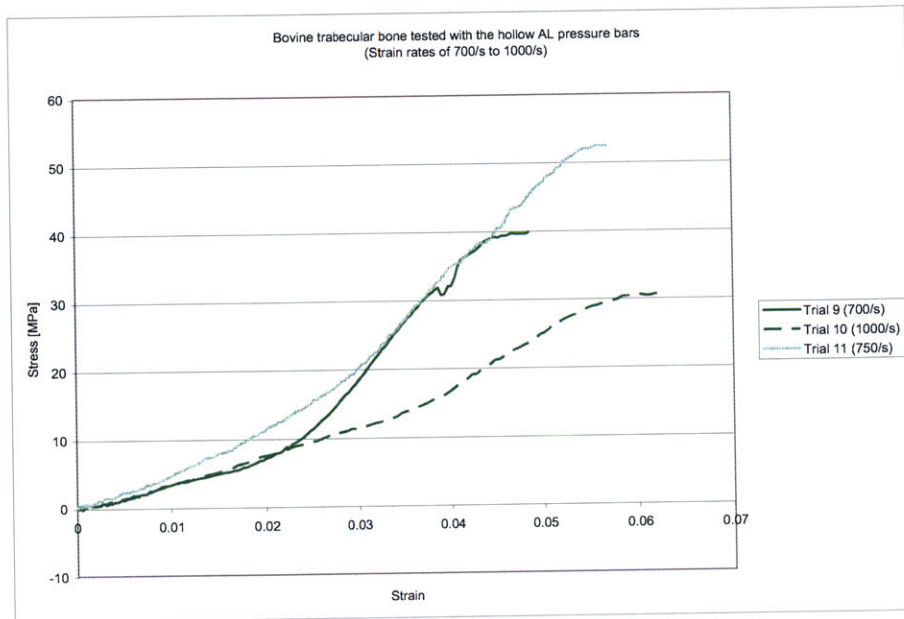


Figure 4-25: Bovine trabecular bone specimens tested at 60 psi with the hollow aluminum SHPB set-up.

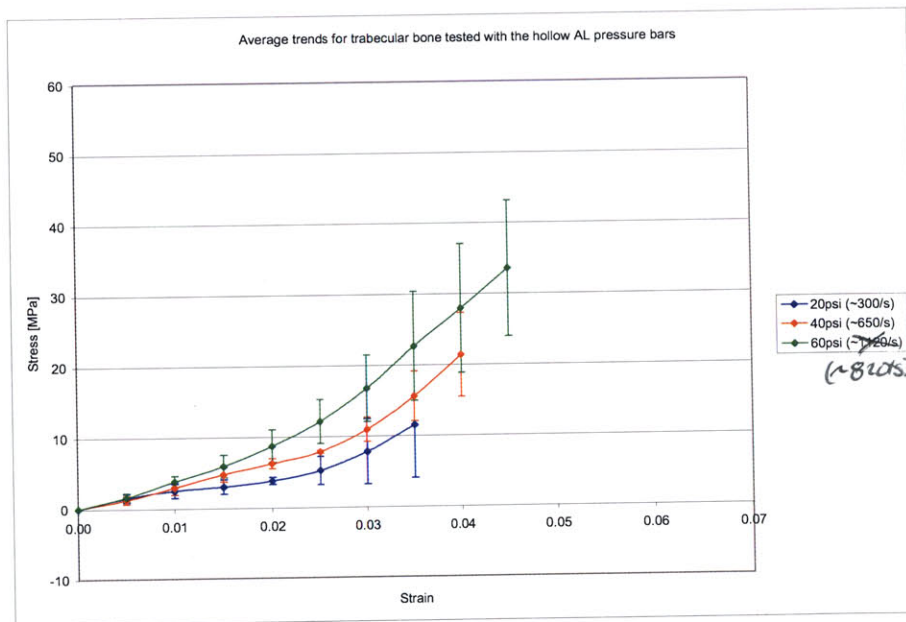


Figure 4-26: Average trends for bovine trabecular bone samples tested with the hollow aluminum SHPB set-up.

### 4.2.3 PMMA Pressure Bars (6" Striker)

The results for the PMMA SHPB trials employing a 6" striker bar are shown here in Figure 4-27, Figure 4-28, and Figure 4-29. The first thing that is apparent from examining these stress-strain curves is that the strains achieved are noticeably less than those attained earlier with either the solid or hollow aluminum SHPB techniques. Also, while similar strain rates to those obtained in the solid and hollow bar techniques are achieved for the 20 psi and 40 psi trials, the strain rates seen in the 60 psi trials are significantly lower. In fact, the rates for the 60 psi trials of this approach are only slightly higher than those of the 40 psi trials. Both of these phenomenon can be accounted for by the fact that the PMMA set-up described here employs a significantly shorter striker bar than that of the previous aluminum bar set-ups (19"). A second contributing factor to the differences encountered between the respective techniques is that the decreased density of the incident bar (PMMA instead of aluminum) meant that less energy was available for transfer to the sample. Consequently, for the same striker bar pressures, lower strains and strain rates are achieved. These shortcomings were partially rectified in the next subsection by employing a longer, 8" striker bar.

The average trends for each of the striker bar pressures employed is summarized in Figure 4-30. The results match well with those of the hollow bar technique and show the same apparent correlation to strain rate, but the curves are noticeably shortened because of the smaller striker bar employed in this technique. In this case, as with all the others, not enough samples were recoverable to allow for a meaningful investigation on the effect of apparent density.

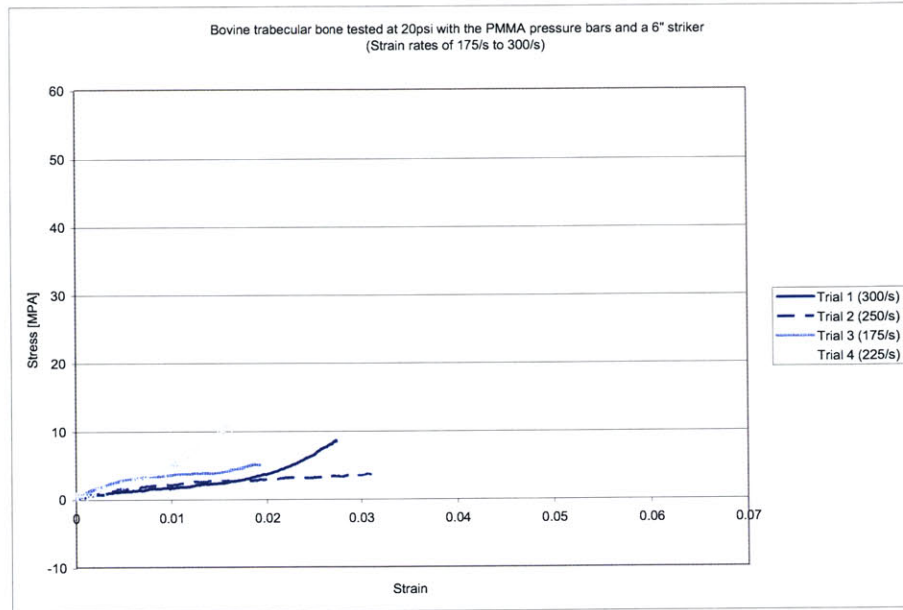


Figure 4-27: Bovine trabecular bone specimens tested at 20 psi with the PMMA SHPB set-up and a 6" striker.

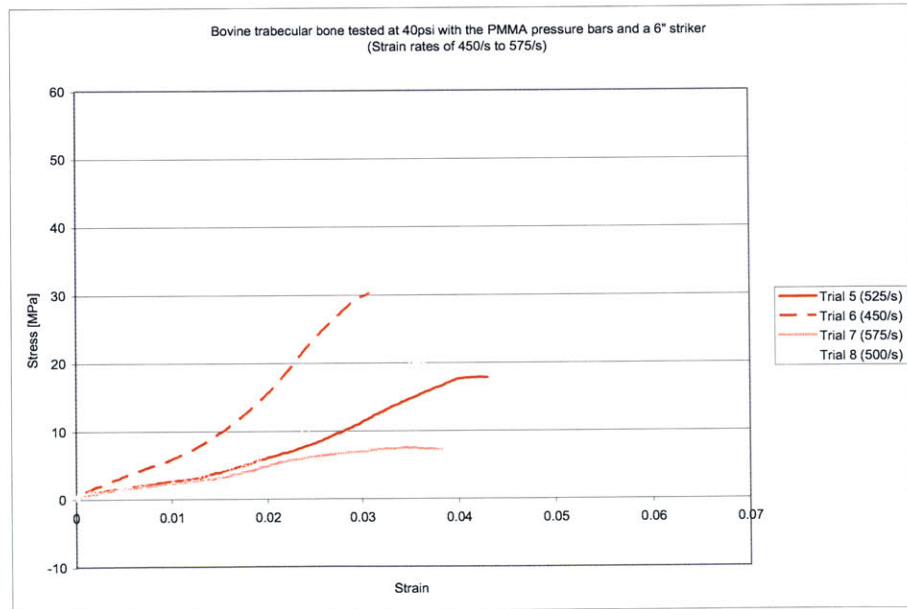


Figure 4-28: Bovine trabecular bone specimens tested at 40 psi with the PMMA SHPB set-up and a 6" striker.

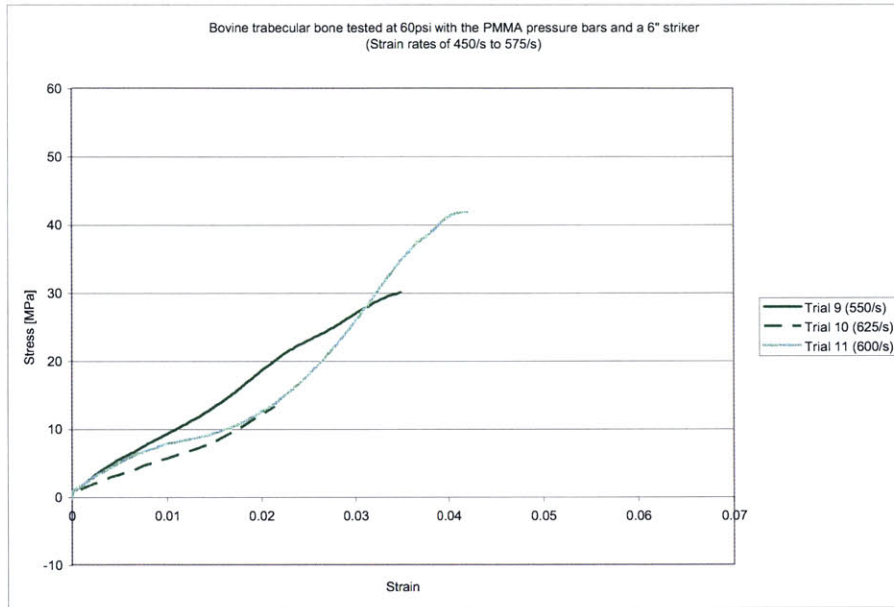


Figure 4-29: Bovine trabecular bone specimens tested at 60 psi with the PMMA SHPB set-up and a 6" striker.

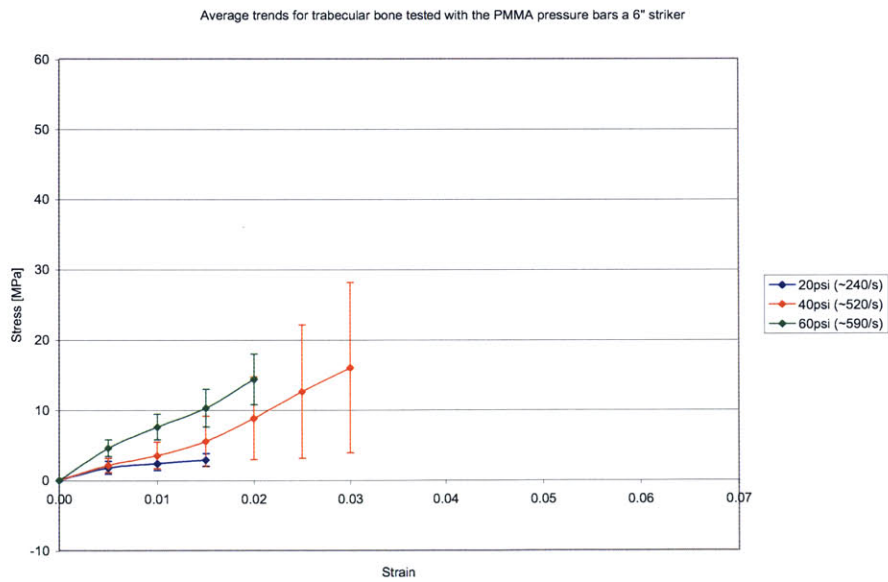


Figure 4-30: Average trends for bovine trabecular bone specimens tested with the PMMA SHPB set-up and a 6" striker.

Trial #	Approx. Strain Rate	Striker Bar Pressure	Specimen Length	Specimen Diameter	Initial Density	Apparent Density
1	300s <sup>-1</sup>	20 psi	6.23 mm	8.05 mm	1249 kg/m <sup>3</sup>	929 kg/m <sup>3</sup>
2	250 s <sup>-1</sup>	20 psi	6.02 mm	8.02 mm	1473 kg/m <sup>3</sup>	931 kg/m <sup>3</sup>
3	175 s <sup>-1</sup>	20 psi	8.05 mm	8.03 mm	1417 kg/m <sup>3</sup>	1106 kg/m <sup>3</sup>
4*	225 s <sup>-1</sup>	20 psi	7.16 mm	8.08 mm	1304 kg/m <sup>3</sup>	845 kg/m <sup>3</sup>
5	525 s <sup>-1</sup>	40 psi	6.40 mm	8.05 mm	1255 kg/m <sup>3</sup>	766 kg/m <sup>3</sup>
6	450 s <sup>-1</sup>	40 psi	7.01 mm	8.07 mm	1341 kg/m <sup>3</sup>	1006 kg/m <sup>3</sup>
7	575 s <sup>-1</sup>	40 psi	6.60 mm	8.08 mm	1213 kg/m <sup>3</sup>	629 kg/m <sup>3</sup>
8*	500 s <sup>-1</sup>	40 psi	7.38 mm	8.09 mm	1301 kg/m <sup>3</sup>	968 kg/m <sup>3</sup>
9	550 s <sup>-1</sup>	60 psi	7.00 mm	8.04 mm	1342 kg/m <sup>3</sup>	898 kg/m <sup>3</sup>
10	625 s <sup>-1</sup>	60 psi	7.30 mm	8.08 mm	1208 kg/m <sup>3</sup>	N/A
11	600 s <sup>-1</sup>	60 psi	7.27 mm	8.08 mm	1376 kg/m <sup>3</sup>	918 kg/m <sup>3</sup>
12*	N/A <sup>I</sup>	60 psi	6.47 mm	8.07 mm	1173 kg/m <sup>3</sup>	N/A
<b>Average</b>			6.91 mm	8.06 mm	1301 kg/m <sup>3</sup>	900 kg/m <sup>3</sup>
<b>Standard Deviation</b>			0.58 mm	0.02 mm	84.5 kg/m <sup>3</sup>	369.8 kg/m <sup>3</sup>
* Trial employing high speed photography (not included in the average trends).						
<sup>I</sup> Incident pulse not captured correctly (truncated).						

Table 4.8: Bovine trabecular bone samples tested with the PMMA SHPB set-up and a 6" striker.



Trial #	Approx. Strain Rate	Striker Bar Pressure	Specimen Length	Specimen Diameter	Initial Density	Apparent Density
13	240 s <sup>-1</sup>	20 psi	6.80 mm	8.08 mm	1362 kg/m <sup>3</sup>	1011 kg/m <sup>3</sup>
14	225 s <sup>-1</sup>	20 psi	8.38 mm	8.07 mm	1145 kg/m <sup>3</sup>	691 kg/m <sup>3</sup>
15	225 s <sup>-1</sup>	20 psi	7.63 mm	8.06 mm	1208 kg/m <sup>3</sup>	702 kg/m <sup>3</sup>
16*	250 s <sup>-1</sup>	20 psi	6.94 mm	8.05 mm	1274 kg/m <sup>3</sup>	782 kg/m <sup>3</sup>
17	550 s <sup>-1</sup>	40 psi	5.87 mm	8.08 mm	1296 kg/m <sup>3</sup>	961 kg/m <sup>3</sup>
18	450 s <sup>-1</sup>	40 psi	7.07 mm	8.08 mm	1405 kg/m <sup>3</sup>	1138 kg/m <sup>3</sup>
19	600 s <sup>-1</sup>	40 psi	5.60 mm	8.05 mm	1276 kg/m <sup>3</sup>	797 kg/m <sup>3</sup>
20*	500 s <sup>-1</sup>	40 psi	5.78 mm	8.06 mm	1411 kg/m <sup>3</sup>	985 kg/m <sup>3</sup>
21	600 s <sup>-1</sup>	60 psi	8.50 mm	8.01 mm	1246 kg/m <sup>3</sup>	N/A
22	500 s <sup>-1</sup>	60 psi	7.99 mm	8.05 mm	1310 kg/m <sup>3</sup>	780 kg/m <sup>3</sup>
23	525 s <sup>-1</sup>	60 psi	7.78 mm	8.01 mm	1462 kg/m <sup>3</sup>	1150 kg/m <sup>3</sup>
24*	N/A <sup>R</sup>	60 psi	6.13 mm	8.08 mm	1388 kg/m <sup>3</sup>	N/A
<b>Average</b>			7.04 mm	8.06 mm	1315 kg/m <sup>3</sup>	901 kg/m <sup>3</sup>
<b>Standard Deviation</b>			1.03 mm	0.02 mm	93.0 kg/m <sup>3</sup>	383.0 kg/m <sup>3</sup>
* Trial employing high speed photography (not included in the average trends).						
<sup>R</sup> Signal was not captured properly due to an improper trigger.						

Table 4.9: Bovine trabecular bone samples tested with the PMMA SHPB set-up and an 8" striker.

#### 4.2.4 PMMA Pressure Bars (8" Striker)

The final approach employed to study the high rate properties of trabecular bone was again a PMMA SHPB technique, but this time employing a slightly longer 8 " striker bar. As demonstrated with the preliminary trials on PU, this was the limit for the current polymer configuration at MIT because for longer strikers interference between the pulses becomes problematic. The results from this last PMMA SHPB approach are shown in Figure 4-31, Figure 4-32, and Figure 4-33. These curves are again noticeably shorter than those of the aluminum bar techniques, but still an improvement from the previous PMMA SHPB technique. The strain rates for the 60 psi trials are again lower than those encountered in the aluminum bar trials, but as seen in Figure 4-34, which summarizes the average trends for each of the striker bar pressures employed, the results match well with those of the hollow bar technique and show the same apparent correlation with strain rate. Finally, as in the other techniques, not enough samples were recoverable to allow investigation into the effect of apparent density on high strain rate mechanical properties.

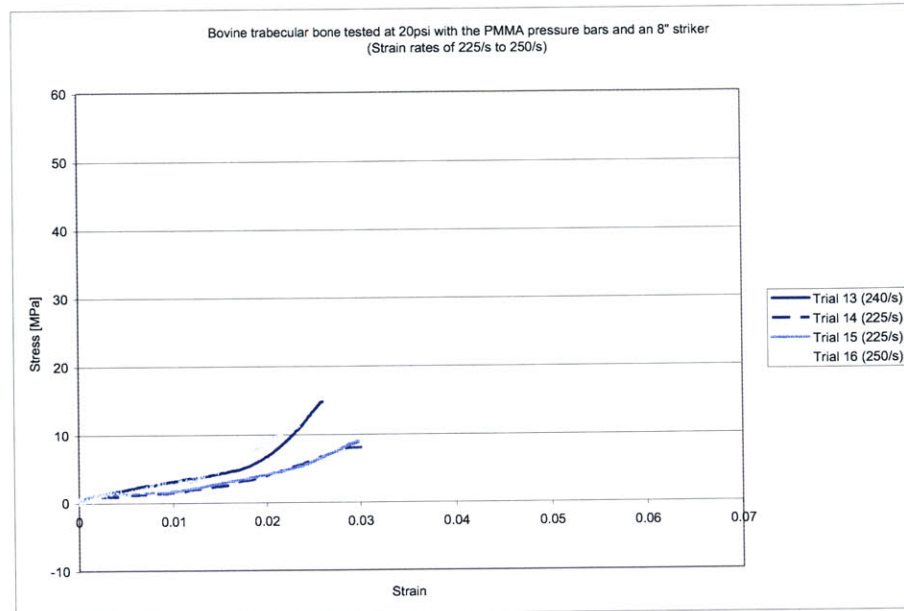


Figure 4-31: Bovine trabecular bone specimens tested at 20 psi with the PMMA SHPB set-up and an 8" striker.

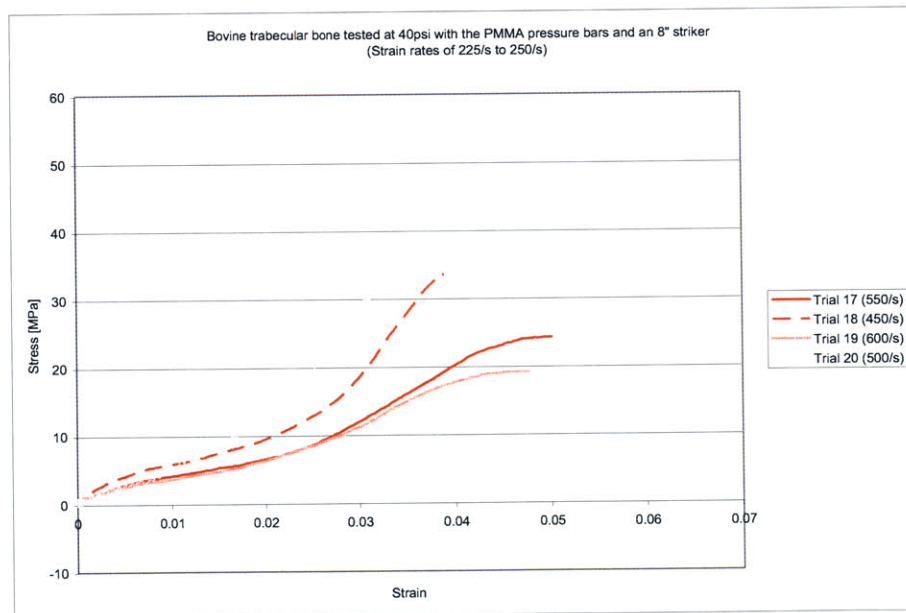


Figure 4-32: Bovine trabecular bone specimens tested at 40 psi with the PMMA SHPB set-up and an 8" striker.

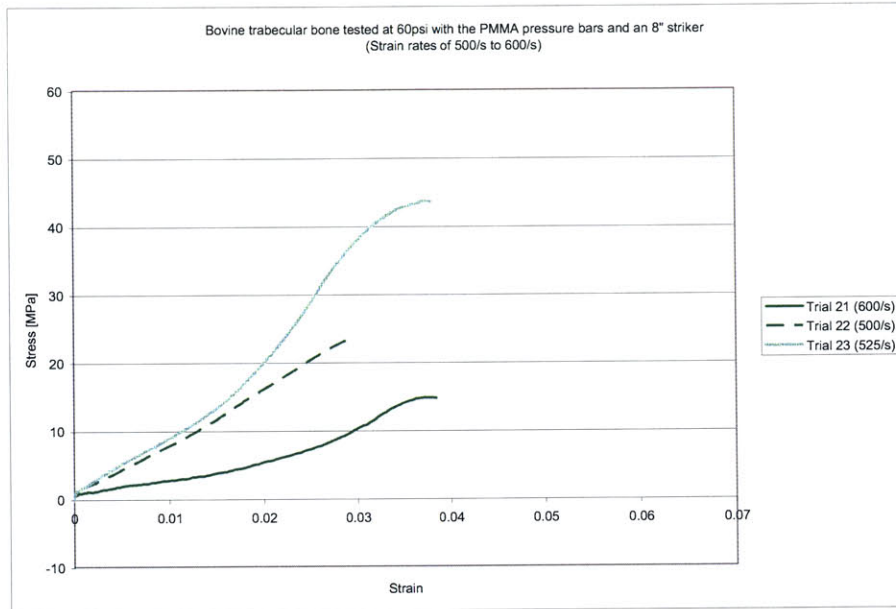


Figure 4-33: Bovine trabecular bone specimens tested at 60 psi with the PMMA SHPB set-up and an 8" striker.

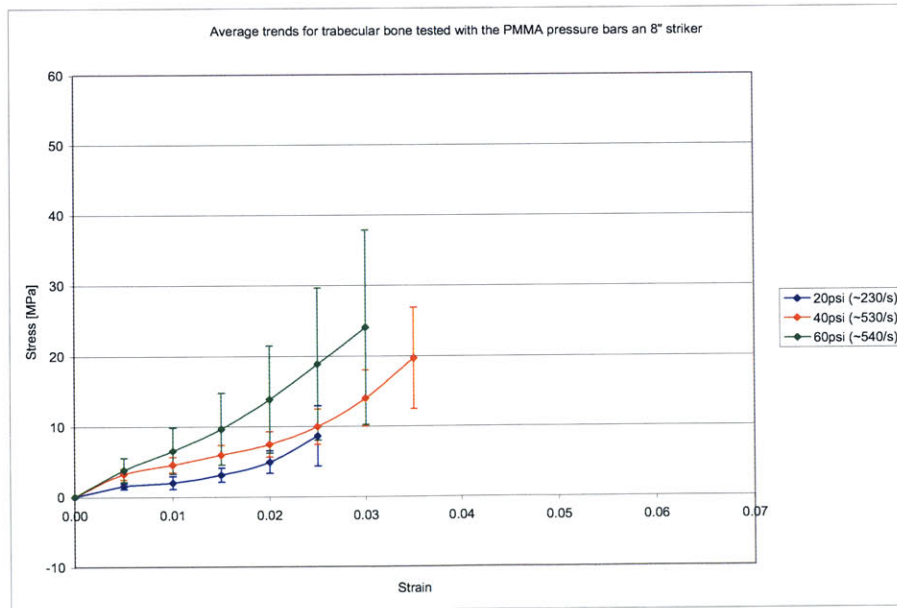


Figure 4-34: Average trends for bovine trabecular bone specimens tested with the PMMA SHPB set-up and an 8" striker.

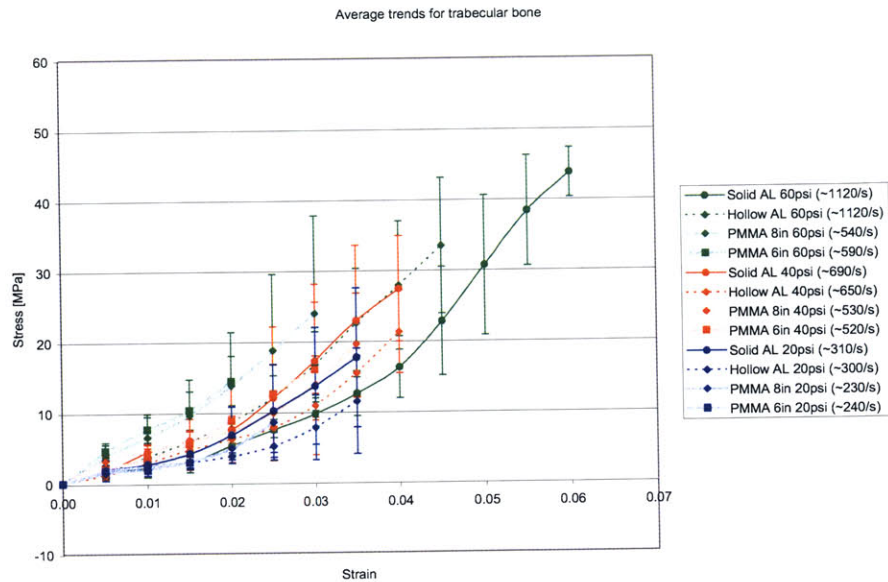


Figure 4-35: Summary of all trabecular bone results.

#### 4.2.5 Trabecular Bone Analysis Summary

Finally, to show that all of the techniques employed in this study do indeed provide comparable results, the average trends for each have been plotted overlying one another in Figure 4-35. The error bars for each curve in this figure are representative of one standard deviation. While the curves do overlap one another and show the same general trend, it is immediately apparent from this figure that there is significantly more scatter than in the case of the preliminary PU study. This may simply be due to the fact that biological tissues are less consistent than synthetic ones, but may also be a consequence of not weighting the curves with their relative apparent densities. The reasons for not being able to conduct this analysis were mentioned and possible solutions will be discussed in Chapter 5.

## Chapter 5

# Conclusions and Recommendations for Future Work

The primary goal of this study was to lay the foundation for bridging the gap between the current abilities of the split-Hopkinson pressure bar technique and those capabilities that will be necessary to characterize the materials of interest for simulation of behind-armour effects of ballistic threats. Historically, the main obstacle to applying the SHPB technique to the study of such materials has been that a large impedance mismatch exists between standard pressure bars and softer, biological specimens. With this in mind, trabecular bone, because of its relatively high stiffness, was selected to be the first biological material to be examined under the auspices of ISN Project 6.9.

To begin the process, a comprehensive literature search was conducted to see what milestones had been previously reached in the understanding of this complicated biological material. While a large number of studies pertinent to bone's low rate behavior were found, surprising little was encountered for rates above  $10 \text{ s}^{-1}$ . This sparsity of information solidified our interest in trabecular bone's characterization, but before testing could begin we needed to obtain an understanding of the techniques available to us and which of these could be employed most effectively in our studies of biological tissues. This understanding was achieved through an extensive literature search, the fruits of which were presented to the reader in Chapter 2. After reviewing the potential candidates, three techniques were chosen for implementation: the solid

aluminum, the hollow aluminum, and the PMMA split-Hopkinson pressure bar techniques. To augment our understanding of each, and because there has been some dissension within the split-Hopkinson community as to the validity of the last two, a comprehensive series of experiments was conducted on a polyurea blend to assess the capabilities of each technique. These trials also allowed us to evaluate the effect of pulse shaping for the hollow bar case, ultimately showing it to be an unnecessary complication for this application. The results of all three techniques showed good correlation to one another. Noteworthy, however, was the low signal-to-noise ratio of the solid aluminum bar set-up and the importance of selecting an appropriate striker bar length, especially when employing polymer pressure bars.

With the techniques having passed the validation trials, they were ready for application to the material of primary concern to us - trabecular bone. Overall, the various methods employed were quite successful at characterizing trabecular bone's high strain rate properties. The rates obtained were satisfactory and the curve trends corresponding to strain rate generally matched those of previous low rate studies. There were, however, several areas where significant improvements could still be made. First, signal alignment in the case of both aluminum bar set-ups should be improved. Second, it would be extremely helpful to further extend the range of our curves to higher levels of strain (while still obtaining the same strain rates). Finally, a new, more reliable, method needs to be developed for measuring the apparent density of the samples, if this factor is to be included in future studies.

In nearly half of the aluminum bar trials analyzed the initial ALSHPB.m assessment showed noticeable misalignment between the incident and reflected pulses. It seems a better algorithm is needed for this process because error from this type of mistake is easily propagated throughout the entire series of stress and strain calculations. While this type of error is easily recognized by the presence of two inverse spikes in the force equilibrium plot, and can be corrected manually from within the code, its correction is nevertheless an unreliable and time consuming process. One potential solution is to align the pulses by initial slopes, rather than by their initial deviation from the baseline. This solution has been implemented in earlier codes, such as hoppy.m, developed by Veli-Tapani Kuokkala and Taina Vuoristo at Sandia National Laboratories. A more precise solution, however, would be to implement the PMMASHPB.m algorithm on the aluminum SHPB system. This could easily be accomplished by running a set of characterization

trials, identical in nature to those already conducted on the PMMA bars, on the aluminum set-up. The advantage of employing this technique is that time keeping, which is ultimately the underlying cause of poor signal alignment, is automatically accounted for by the transfer function. The benefit of this approach is easily recognized by comparing the excellent force balance shown for the PMMA trials (see Figure E-3) to that of the inferior aluminum bar trials (see Figures A-4 and A-5).

With regards to increasing the strain levels achieved during the tests there is a simple, straightforward solution: increase the length of the striker bars employed. The problem then becomes how to increase the length of the striker bars without running into the problem of signal interference, the importance of which was already demonstrated during the PU trials. The long term solution would be to simply obtain longer incident and transmission bars so that the strain gauges could be placed well away from the sample and allow for the use of longer striker bars without the problem of pulses overlapping. A more immediate and economical solution, however, would be to place new strain gauges on the current bars further away from the test specimens. The optimization of this approach would be to place the gauges exactly in the middle of the bars (any further away and interference from waves reflecting off the far end of the bar would become a problem). By changing strain gauge location from its current position (30" from the specimen end) to the middle of the bar (45" from the specimen end) we would be able to employ striker bars that were approximately 50% longer. This would increase the total attainable strain levels by roughly the same amount. Finally, in addition to using longer striker bars, slightly shorter samples could be employed to further augment the strain levels achieved. Care should be taken when implementing this solution, however, to assure that the adjustment in specimen size does not violate the continuum assumption of the material.

Finally, there is substantial room for improvement in the measurement of apparent density. Here the problem was that many of the specimens were only partially recovered after having been seriously damaged during the experimental trials. A simple solution to this problem would be to remachine the remaining portion of the specimens into regular shapes before following the demarrowing procedure set forth in Chapter 3, Section 3. Unfortunately, there was not time during this study to implement this new procedure, but samples from the project are still in storage at -20°C in a 0.1 M saline solution so further analysis is possible and would be of

interest.

Looking forward, beyond just achieving higher strains in trabecular bone, this laboratory is committed to accurately characterizing the high rate behavior of a wide variety of biological tissues and related soft materials. Preliminary trials have been conducted on soft tissue simulants, such as Ordinance 250A Ballistic Gelatin and RTV6166 Silicon Gel (see Figure H-2), but even with the low impedance polymer bars in place no measurable strain is transferred through to the transmission bar. This indicates that the calculation of these materials' properties still lie far beyond the capabilities of the techniques employed within this study and the current abilities of the SHPB community as a whole.

One proposed solution would be to employ large diameter hollow pressure bars composed of PMMA. Using a hollow PMMA bars would allow us to further decrease their impedance, while the larger diameter would allow for increasing the diameter of the specimen, thereby increasing its impedance. This combined benefit may bring the impedance mismatch within a measurable range. It should be noted, however, that because of the slow wave speed seen in many soft materials the specimens would have to be made thinner in order to allow them to quickly reach a state of dynamic equilibrium. This, in combination with the increased diameter, would unfortunately go against previous recommendations that specimens maintain a 0.5 length-to-diameter ratio. In this scenario, however, we feel that the benefits would far outweigh the consequences. Furthermore, the effects of this change in geometry could be estimated and corrected for with the use of finite element analysis.

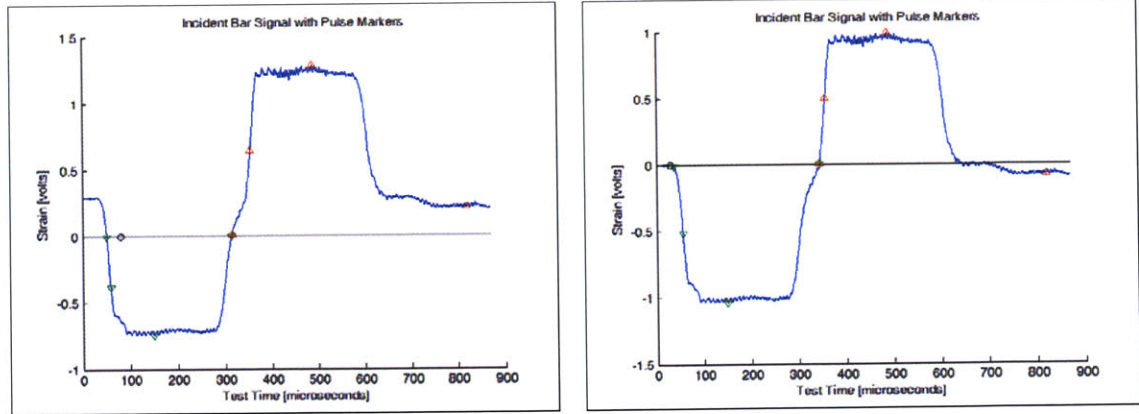


## Appendix A

# ALSHPB.m Procedure

In analyzing the data, the ALSHPB.m code prompts the user for the dimensions of the cylindrical specimen tested. Once these values have been loaded, the wave speed, Young's modulus, and diameter of the bar are defined. Also, the internal diameter of the transmission bar is established. If the solid transmission bar was used this value is simply set to zero. Next, cross sectional areas of the incident and transmission bars are calculated and the parameters for zeroing and isolating the pulse are established. The number of data points used to establish the zero strain baseline for the incident and transmission bars are stored in the variables "inciLeading" and "transLeading". The importance of these parameters will be demonstrated later. The values for "inciSlope," "reflSlope," and "transSlope," which determine the location of the reference point in the pulse isolating algorithm, are then set to 0.5, or half of the maximum amplitude of the pulse to which they are applied. Finally, the percent deviation from zero for the trigger is defined, the number of smoothing points used to find the start of the transmission pulse for weak signals is established, the conditioner frequency range is set, and the overall number of data points used for the signal processing is defined.

Next, ALSHPB.m loads the data file corresponding to the incident bar signal as specified by the user. This data is first translated into microseconds and volts for the subsequent calculations. Next, the time portion of each signal is zeroed, and a baseline for the voltage is established. The accurate calculation of this baseline depends on specifying an ample pretrigger delay during the experimental setup. If the leading section of the incident signal is too short, the number of sample points, "inciLeading" (or "transLeading" in the transmission bar case),



(a) Poor baseline calculations can result from either a short experimental pretrigger delay or sampling too many initial points during the analysis.

(b) A more reliable baseline can be obtained by adjusting the number of initial data points used in calculating the baseline.

Figure A-1: Establishing a reliable baseline is essential to accurately isolating pulses.

requires manual adjustment to assure that an appropriate baseline is found (Figure A-1). Once an appropriate incident baseline has been established, the signal is zeroed relative to it. The signal is then plotted in blue along with the baseline in black (Figure A-1). Next, the minimum strain value of the incident signal is found and its location marked on the previous plot with a green triangle. Working backwards from this minimum strain value, a reference point, whose strain value is half the magnitude of the minimum's, is established and plotted with a second green marker. From the reference point the code continues working stepwise back in time, searching for the first point that has a magnitude less than a certain percentage ("percentTrigger") of incident signal's minimum. This point is then recorded as the start of the incident pulse and its position is plotted with another green marker. Finally, the end of the incident pulse is found by working forward in time and marking the first non-negative point with a fourth and final green marker (Figure A-1). Once the incident pulse has been isolated it is recorded in two different formats. The first being with the time information zeroed to coincide with the start of the individual pulse, and the second with the original time scale of the experiment.

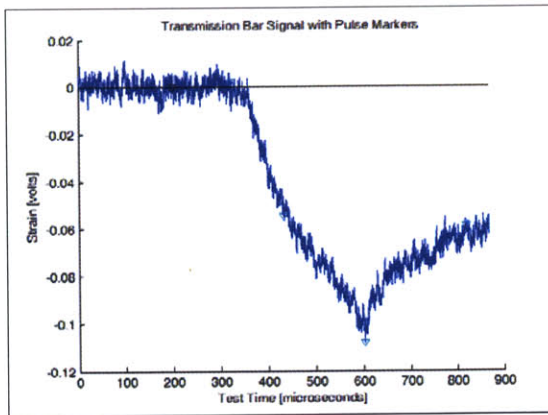
With the incident pulse information recorded, ALSHPB.m continues on to find the reference points and starting point of the reflected pulse (indicated by the red markers in Figure A-1). This is accomplished in a similar manner to that of the incident pulse, but using the maximum

of the incident bar signal rather than the minimum. Also, the end of the reflected pulse is selected manually by the user in order to assure accurate capture of the specimen's unloading behavior.

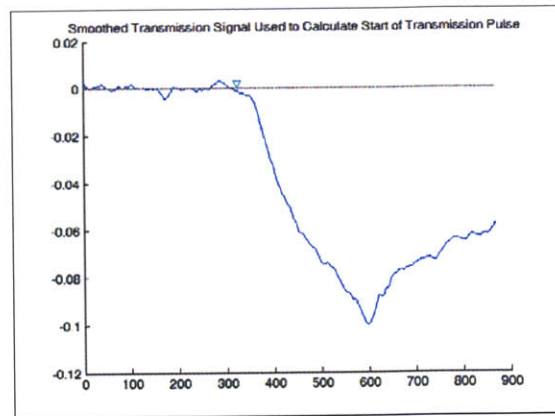
Next, the transmission bar signal is specified by the user and loaded into the program. This pulse is handled in a similar manner to that of the incident and reflected pulses but with markers being plotted in cyan (Figure A-2). Calculating the start of the pulse, however, can be unreliable when testing soft specimens because the pulses tend to have a very low signal-to-noise ratios (especially those acquired with the solid aluminum transmission bar). To help overcome this complication, a smoothing function is used to find the point where the moving average's value becomes greater than the transmission bar's percent trigger value. This smoothed function is then plotted in conjunction with the original transmission signal so the user can check that an appropriate starting point was chosen (see again Figure A-2). As an additional check on the start and end point selections, all three pulses are plotted together both in the unshifted and shifted time frames (Figure A-3). If it is clear from these plots that the starting points of the pulses are not being isolated accurately, the user can now opt to terminate the program and activate the manual override point selection from within the code. It should be noted, however, that it is normal for the unshifted transmission pulse to appear to lag slightly behind the reflected pulse. This is due to the extra time it takes for the signal to pass through the length of the specimen. More important is whether or not the pulses appear to line up correctly in the shifted pulse time frame.

Next, the Fourier transform of each signal is taken and the frequency power spectrum is calculated and plotted. The purpose of this exercise was two fold: one, to practice the technique so it could be more easily implemented in subsequent viscoelastic codes; and two, so that the frequency components of the signal can be checked against the capabilities of the signal conditioner used to acquire the data (see Figure C-1 for an example of the frequency power spectrum plots).

Continuing on in ALSHPB.m, the calibration factor for the strain gauges used is calculated and multiplied by each individual strain signal to convert it from volts to percent strain. All strain signal vectors are then defined to be the same length, the ends of the shorter signals being padded with zeros. Next, the forces are calculated by implementing equations (2.6)

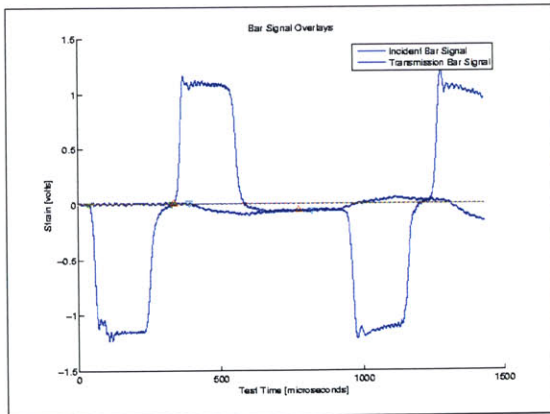


(a) The low signal-to-noise ratio in the solid transmission bar's signal for soft specimens makes it difficult to decipher the start of the pulse

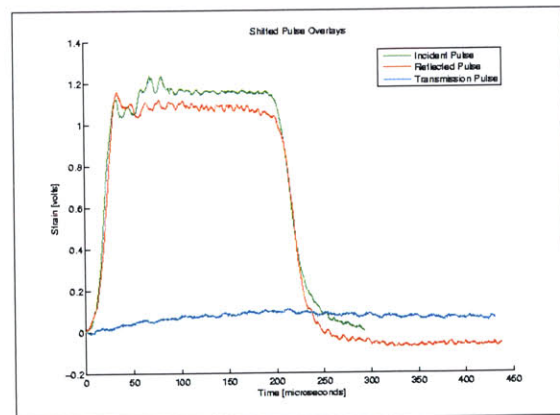


(b) The smoothed transmission bar signal is used to more effectively calculate the pulse start and is plotted for visual verification by the user.

Figure A-2: A smoothing function is used to assist in finding the start of the transmission pulse.

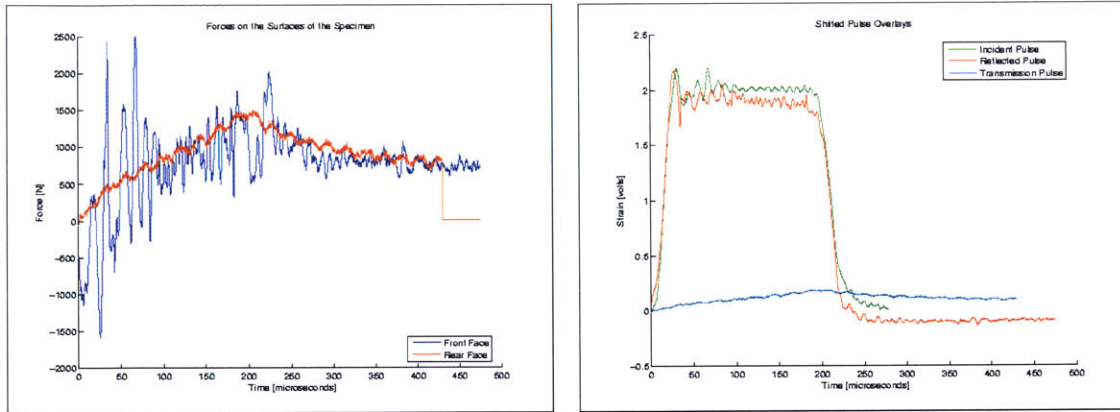


(a) Unshifted time frame.



(b) Shifted time frame.

Figure A-3: Overlapping pulse plots with visual markers allow the user to verify the selection of starting and ending points.



(a) A force diagram showing good force balance between the front and rear face of the specimen.

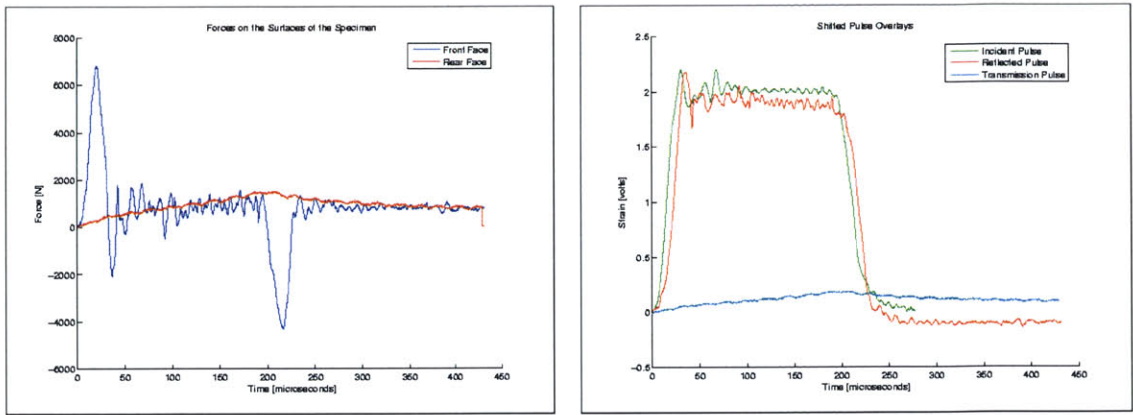
(b) The shifted time frame corresponding to good force balance: the incident and reflected signal overlap one another.

Figure A-4: Good force balance obtained for a PU specimen tested on the solid aluminum bar by manually adjusting the selection time.

and (2.12). These forces are then plotted, allowing user to check the validity of the dynamic equilibrium assumption (Figure A-4 and Figure A-5). Because the front face force is calculated using the difference of two pulses, it is consistently noisier than the calculated rear face force. It should, however, oscillated equally above and below the calculated rear face force (Figure A-4). If the two plots do not overlap one another, dynamic equilibrium was not achieved and any subsequent calculations of stress and strain would be invalid. If it is observed that there is a large spike at the beginning of the force overlay, and equally large inverse spike at the moment of peak stress (Figure A-5), either the incident or reflected signal may have not been properly isolated and therefore slightly shifted relative to the other. This can be easily remedied using the manual override selection mentioned earlier. Once the forces are plotted, the program will prompt the user to find where force balance is first achieved. This point will be marked on subsequent stress, strain, and strain rate plots with an open dot. Finally, the user is prompted to determine where force balance ends. The point chosen may either be the end of force balance or, if the user does not wish to see the unloading behavior of the material, it may simply be the point of maximum force. Either way, the program will only carry subsequent calculations up to this reference time.

With the forces calculated and validated, the three wave stress analysis method (equations (2.4) and (2.8)) is implemented to determine the engineering stress, strain rate, and strain





(a) A force diagram showing poor force balance between the front and rear face of the specimen.

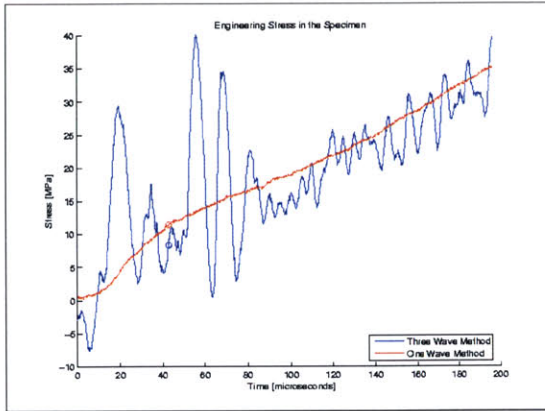
(b) The shifted time frame corresponding to improper force balance: the incident and reflected signals do not overlap.

Figure A-5: The force balance for the same solid aluminum PU trial prior to manual adjustment.

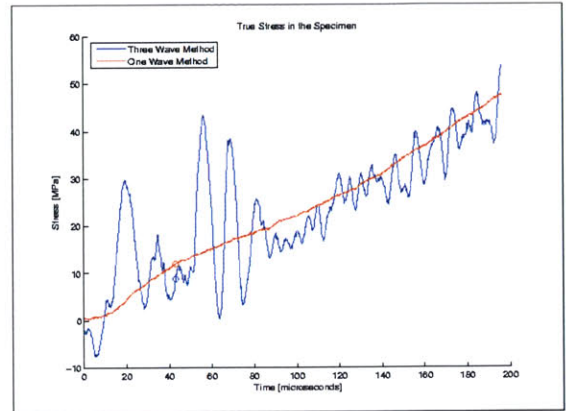
(calculated using MATLAB's cumtrapz function to integrate strain rate). Next, the true strain for the three wave analysis is calculated from the engineering strain, and the true stress is approximated by multiplying engineering stress by one plus the engineering strain (this formulation, however, is valid only if the specimen tested is incompressible). Moving forward under the assumption of dynamic equilibrium within the specimen, the one wave stress analysis (equations (2.10) and (2.11)) is then implemented and used to calculate the same parameters as described in the three wave analysis. In addition, true strain rate is calculated for both the one wave and the three wave methods by dividing the change in calculated true strain by the time interval between data points.

With all the calculations completed, the engineering stress is then plotted for both the one wave and three wave analyses, as are the approximated true stress, engineering strain, true strain, engineering strain rate, and true strain rate (Figure A-6, Figure A-7, and Figure A-8). Finally the engineering stress vs. engineering strain and approximated true stress vs. true strain are plotted (Figure A-9). In all of these plots blue is used for the three wave method and red is used for the one wave method to allow for easy comparison of the results. The results are then saved into two \*.txt files so they can be easily accessed for further analysis at a later date. Of these two files, the "OneWave.txt" file the contains the engineering strain, engineering strain rate, engineering stress, true strain, true strain rate, and approximated true

stress data for the one wave calculations, while "ThreeWave.txt" is written in the same order but with the data for the three wave calculations.

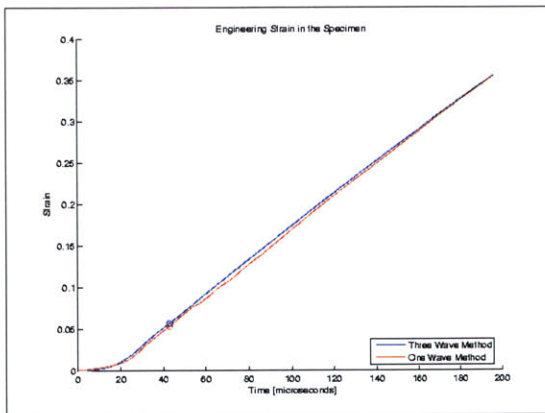


(a) Engineering stress vs. time.

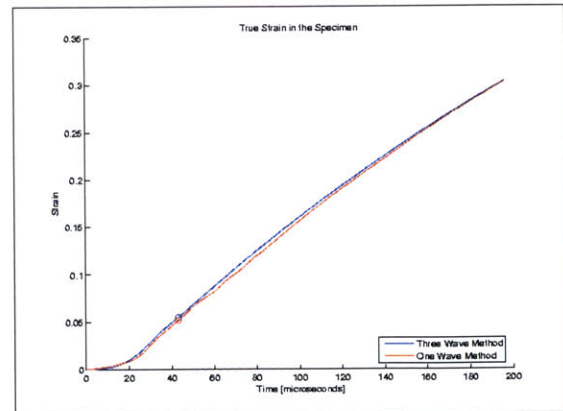


(b) True stress vs. time.

Figure A-6: Examples of the stress plots generated for a PU sample tested on the hollow aluminum bars.



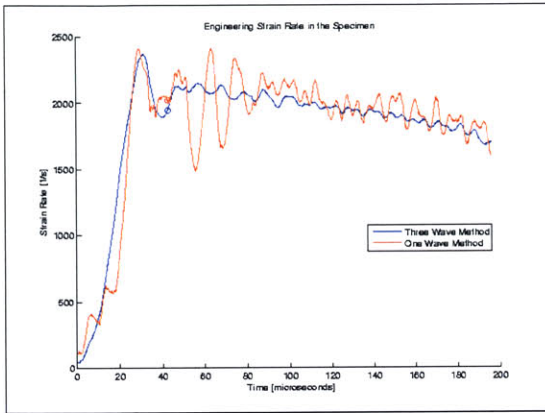
(a) Engineering strain vs. time.



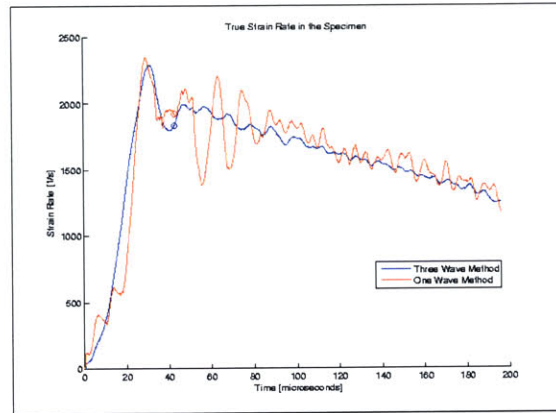
(b) True strain vs. time.

Figure A-7: Examples of the strain plots for a PU sample tested on the hollow aluminum bars.



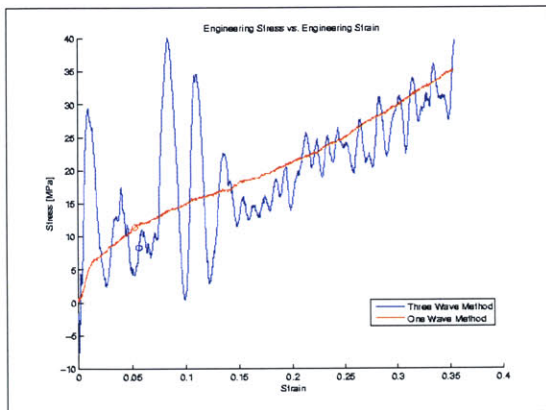


(a) Engineering strain rate vs. time.

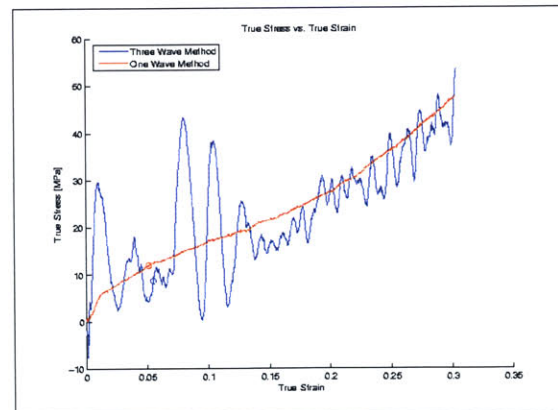


(b) True strain rate vs. time.

Figure A-8: Examples of the strain rate plots for a PU sample tested on the hollow aluminum bars.



(a) Engineering stress vs. engineering strain.



(b) True stress vs. true strain.

Figure A-9: Examples of the stress vs. strain plots for a PU sample tested on the hollow aluminum bars.



## Appendix B

### ALSHPB.m Code

```
% ALSHPB.m
% Timothy P. M. Johnson
% Institute for Soldier Nanotechnologies
% Massachusetts Institute of Technology
% June 2005
% NOTE SIGN CONVENTION: Compression is Positive

clear all
close all

% SPECIMEN PARAMETERS
Dsmm=input('What is the diameter of the specimen in millimeters? ');
Ds=Dsmm*10^-3;      % Diameter of the specimen in [m]\quad
Lsmm=input('What is the length of the specimen in millimeters? ');
Ls=Lsmm*10^-3;     % Length of specimen in [m]
Aspec=pi*(Ds/2)^2; % Cross sectional area of the specimen in [m^2]

% BAR PARAMETERS
CO=5091;           % Wave speed [m/s]
E=72000;          % Modulus [N/mm^2 == MPa]
```

```

Dbar=0.01905;      % Bar Diameter [m]
Dhole=Dbar-(3e-3); % Diameter of hollow core in trasmission bar
Abar=pi*(Dbar/2)^2; % Cross sectional area of the bar
Atrans=Abar-pi*(Dhole/2)^2;

% PARAMETERS FOR ZEROING AND ISOLATING THE PULSE
inciLeading=150;    % Number of initial points used to calculate incident
baseline
transLeading=650;   % Number of initial points used to calculate transmission
baseline
inciSlope=0.5;     % Location of reference point on incident slope, as a
fraction of signal minimum
reflSlope=0.5;     % Location of reference point on reflected slope, as a
fraction of signal maximum
transSlope=0.25;   % Location of reference point on transmission slope, as a
fraction of signal minimum
percentTrigger=0.005;% Percent deviation from zero that signals the start of a
pulse
smoothingPts=100; % Number of points used in the moving average smoothing
function to detect the start of the transmission pulse for low
signal-to-noise ratio transmission signals

% SIGNAL PROCESSING PARAMETERS
conditionerRange = 50000; % Frequency range of the data acquisition hardware
signalSize = 2^12;      % Size of signal after padding

% CAPTURING INCIDENT AND REFLECTED PULSES
[fname, fpath]=uigetfile('*.asc','Select Incident Bar Signal'); % Read the
incident bar pulses; the data is time (seconds) vs. strain (in volts!)
cd(fpath)

```

```

channel1=load([fpath fname]);
tim=channel1(:,1);
dt=(tim(end)-tim(1))/(length(tim)-1); % dt is the time interval between
points in seconds
tim=tim*10^6; % Changes time from seconds to microseconds
tim=tim-tim(1); % Zero the time
EPS=channel1(:,2);
sampleFreq=((tim(2)-tim(1))*1E-6)^-1;

% INCIDENT BAR SIGNAL AND PULSE MARKERS
figure('name','Incident Bar Signal')
hold on
title('Incident Bar Signal with Pulse Markers');
xlabel('Test Time [microseconds]');
ylabel('Strain [volts]');

% Calculate incident pulse baseline, for zeroeing
flatBaseline=polyfit(tim(1:inciLeading),EPS(1:inciLeading),0); % Using y =
constant method
EPS=EPS-flatBaseline(1); % Zeros the strain
plot(tim,EPS)
plot(tim,0,'k') % Plots black baseline
plot(tim(inciLeading),0,'ko') % Places black 'o' marker at last point used
in calculating baseline (allows user to see if larger inciLeading should be used)

% Locate reference point on incident slope
[minimum,centerIncidentIndex]=min(EPS);
plot(tim(centerIncidentIndex),minimum,'gv')
lim1=inciSlope*minimum;
ind=1;

```

```

while EPS(ind)>lim1
    ind=ind+1;
end
ipoint=ind;
plot(tim(ipoint),EPS(ipoint),'gv')
% Back up to find exact start of incident pulse
ind=ipoint;
while EPS(ind)<percentTrigger*minimum
    ind=ind-1;
end
startIncident=ind;
% MANUAL OVERRIDE FOR POINT SELECTION:
%startIncident=dsearchn(tim,ENTER TIME);
plot(tim(startIncident),EPS(startIncident),'gv')
% Move up to find finish of incident pulse
ind=ipoint;
while EPS(ind)<0
    ind=ind+1;
end
endIncident=ind;
% MANUAL OVERRIDE FOR POINT SELECTION:
%endIncident=dsearchn(tim,ENTER TIME);
plot(tim(endIncident),EPS(endIncident),'gv')

iTime=tim(startIncident:endIncident)-tim(startIncident);
onlyIncident=-EPS(startIncident:endIncident); % NOTE NEGATIVE SIGN: MAKES
COMPRESSION SIGNALS POSITIVE
incident=zeros(signalSize,1);
incident(startIncident:endIncident)=onlyIncident;

```

```

% Locate reference point on reflected slope
[maximum,centerReflectedIndex]=max(EPS);
plot(tim(centerReflectedIndex),maximum,'r^')
lim1=reflSlope*maximum;
ind=ipoint;
while EPS(ind)<lim1
    ind=ind+1;
end
rpoint=ind;
plot(tim(rpoint),EPS(rpoint),'r^')
% Back up to find the start of the reflected pulse
ind=rpoint;
while EPS(ind)>percentTrigger*maximum
    ind=ind-1;
end
startReflected=ind;
% MANUAL OVERRIDE FOR POINT SELECTION:
%startReflected=dsearchn(tim,ENTER TIME);
plot(tim(startReflected),EPS(startReflected),'r^')
% Move up to find finish of reflected pulse
%ind=rpoint;
%while EPS(ind)>0
%    ind=ind+1;
%end
%endReflected=ind;
% Manually input end of reflected pulse
disp('Choose the end point of the reflected pulse: ')
position=ginput(1);
endReflected=dsearchn(tim,position(1));
if endReflected>signalSize

```

```

        endReflected=signalSize;
    end
    plot(tim(endReflected),EPS(endReflected),'r^')

    rTime=tim(startReflected:endReflected)-tim(startReflected);
    onlyReflected=-EPS(startReflected:endReflected);    % NOTE NEGATIVE SIGN:
    MAKES TENSILE SIGNAL NEGATIVE
    reflected=zeros(signalSize,1);
    reflected(startReflected:endReflected)=onlyReflected;

    print -dbmp16m Incident_Bar_Signal

    % CAPTURING TRANSMITTED PULSE
    [fname, fpath]=uigetfile('*.asc','Select Transmission Bar Signal'); % Read
    the transmission bar pulse; the data is time (seconds) vs. strain (in volts!)
    channel2=load([fpath fname]);
    timT=channel2(:,1);
    dtT=(timT(end)-timT(1))/(length(timT)-1); % dtT is the time interval between
    points in seconds for the transmission bar
    timT=timT*10^6; % Changes time from seconds to microseconds
    timT=timT-timT(1); % Zero the time
    EPST=channel2(:,2);
    sampleFreqT=((timT(2)-timT(1))*1E-6)^-1;

    % TRANSMISSION BAR SIGNAL AND PULSE MARKERS
    figure('name','Transmission Bar Signal')
    hold on
    title('Transmission Bar Signal with Pulse Markers');
    xlabel('Test Time [microseconds]');
    ylabel('Strain [volts]');

```



```

% Calculate transmission pulse baseline, for zeroeing
flatBaselineT=polyfit(timT(1:transLeading),EPST(1:transLeading),0); % Using
y = constant method
EPST=EPST-flatBaselineT(1); % Zeros the strain
plot(timT,EPST)
plot(timT,0,'k') % Plots black baseline
plot(timT(transLeading),0,'ko') % Places black 'o' marker at last point used
in calculating baseline (allows user to see if larger transLeading should be
used)

% Locate reference point on transmission slope
[minimumT,centerTransmissionIndex]=min(EPST);
plot(timT(centerTransmissionIndex),minimumT,'cv')
lim2=transSlope*minimumT;
ind=1;
while EPST(ind)>lim2
    ind=ind+1;
end
tpoint=ind;
plot(timT(tpoint),EPST(tpoint),'cv')
% Back up to find exact start of transmission pulse
smoothEPST=smooth(EPST,smoothingPts); % added to handle low signal to noise
ration transmission pulses
ind=tpoint;
while smoothEPST(ind)<percentTrigger*minimumT
    ind=ind-1;
end
startTransmission=ind;
% MANUAL OVERRIDE FOR POINT SELECTION:

```

```

%startTransmission=dsearchn(timT,ENTER TIME);
plot(timT(startTransmission),EPST(startTransmission),'cv')
% Move up to find finish of transmission pulse
ind=tpoint;
    while EPST(ind)<0 & ind<signalSize
        ind=ind+1;
    end
endTransmission=ind;
% MANUAL OVERRIDE FOR POINT SELECTION:
%endTransmission=dsearchn(timT,ENTER TIME);
plot(timT(endTransmission),EPST(endTransmission),'cv')

tTime=timT(startTransmission:endTransmission)-timT(startTransmission);
onlyTransmission=-EPST(startTransmission:endTransmission); % NOTE NEGATIVE
SIGN: MAKES COMPRESSION SIGNALS POSITIVE
transmission=zeros(signalSize,1);
transmission(startTransmission:endTransmission)=onlyTransmission;

print -dbmp16m Transmission_Bar_Signal

figure('name','Smoothed Transmission Signal')
title('Smoothed Transmission Signal Used to Calculate Start of Transmission
Pulse')
hold on
plot(timT,smoothEPST)
plot(timT,0)
plot(timT(startTransmission),EPST(startTransmission),'cv')

print -dbmp16m Smoothed_Transmission_Signal

```

```

% COMPARITIVE OVERLAYS
figure('name','Raw Signal Overlays')
hold on
plot(tim,EPS)
plot(timT,EPST)
plot(tim,0)
plot(tim(startIncident),EPS(startIncident),'gv')
plot(tim(endIncident),EPS(endIncident),'gv')
plot(tim(startReflected),EPS(startReflected),'r^')
plot(tim(endReflected),EPS(endReflected),'r^')
plot(timT(startTransmission),EPST(startTransmission),'cv')
plot(timT(endTransmission),EPST(endTransmission),'cv')
title('Bar Signal Overlays')
xlabel('Test Time [microseconds]')
ylabel('Strain [volts]')
legend('Incident Bar Signal','Transmission Bar Signal')

print -dbmp16m Raw_Signal_Overlays

figure('name','Shifted Pulse Overlays')
hold on
plot(iTime,onlyIncident,'g')
plot(rTime,-onlyReflected,'r')
plot(tTime,onlyTransmission,'c')
title('Shifted Pulse Overlays');
xlabel('Time [microseconds]');
ylabel('Strain [volts]');
legend('Incident Pulse','Reflected Pulse','Transmission Pulse','location',
'best')

```

```

print -dbmp16m Shifted_Pulse_Overlays

% FOURIER TRANSFORM OF INCIDENT SIGNAL
figure('name','Incident Transform')
IFourier=fft(incident);
iFourier=fftshift(IFourier);
Npts=length(iFourier);
% Handling folding frequency based on C. Bacon's fftfrequencies.m
Nshanon=ceil(Npts/2);
T=(tim(end)-tim(1))*10^-6;
df=1/T;
for q=1:Nshanon
\qqquad freq(q,1)=(q-1)*df;
end
for q=Nshanon+1:Npts
\qqquad freq(q,1)=(q-1-Npts)*df;
end
freq=fftshift(freq);
iFreq=freq(find(freq>=0));
iFourier=iFourier(find(freq>=0));
iPower=abs(iFourier).^2;
plot(iFreq,iPower)
title('Frequency Spectrum of the Incident Signal');
xlabel('Frequency (Hz)');
ylabel('Power Index');
axis([0 conditionerRange/2 0 1E4]);

freqz=iFreq;

print -dbmp16m Incident_Transform

```

```

% FOURIER TRANSFORM OF REFLECTED SIGNAL
figure('name','Reflected Transform')
RFourier=fft(reflected);
rFourier=fftshift(RFourier);
rFreq=freq(find(freq>=0));
rFourier=rFourier(find(freq>=0));
rPower=abs(rFourier).^2;
plot(rFreq,rPower)
title('Frequency Spectrum of the Reflected Signal');
xlabel('Frequency (Hz)');
ylabel('Power Index');
axis([0 conditionerRange/2 0 1E4]);

print -dbmp16m Reflected_Transform

% FOURIER TRANSFORM OF TRANSMISSION SIGNAL
figure('name','Transmission Transform')
TFourier=fft(transmission);
tFourier=fftshift(TFourier);
tFreq=freq(find(freq>=0)); % freq is the same for transmission signal because
signals are the same size and period is the same size
tFourier=tFourier(find(freq>=0));
tPower=abs(tFourier).^2;
plot(tFreq,tPower)
title('Frequency Spectrum of the Transmission Signal');
xlabel('Frequency (Hz)');
ylabel('Power Index');
axis([0 conditionerRange/2 0 1E4]);

```

```

print -dbmp16m Transmission_Transform

% CONVERTING TO STRAIN FROM VOLTS
calibrationValue_incident=0.37471*10(-3); % 1V = _____ strain (if 1000
microstrain, its 1e-3)
bridgeType=1; % if half-bridge, put 0.5: must
divide the strain by 2. quarter-bridge, put 1
calibrationValue_transmit=0.37471*10(-3); % 1V = _____ strain (if 1000
microstrain, its 1e-3)

scalingFactor_incident=calibrationValue_incident*bridgeType;
scalingFactor_transmit=calibrationValue_transmit*bridgeType;

ei=onlyIncident*scalingFactor_incident;
er=onlyReflected*scalingFactor_incident;
et=onlyTransmission*scalingFactor_transmit;

analysisTime=[0:(dt*1e6):max([iTime(end) rTime(end) tTime(end)])];
analysisDuration=max([length(ei) length(er) length(et)]);
Ei=zeros(analysisDuration,1);
Er=zeros(analysisDuration,1);
Et=zeros(analysisDuration,1);
Ei(1:size(ei))=ei;
Er(1:size(er))=er;
Et(1:size(et))=et;

% CALCULATE SURFACE FORCES [MPA]
F1=E*Abar*(Ei+Er)*106;
F2=E*Atrans*Et*106;

```

```

figure('name','Forces on Specimen Faces')
hold on
plot(analysisTime,F1,'b')
plot(analysisTime,F2,'r')
title('Forces on the Surfaces of the Specimen')
xlabel('Time [microseconds]')
ylabel ('Force [N]')
legend('Front Face','Rear Face','location','best')

print -dbmp16m Forces_on_Specimen_Faces

% Find force balance reference
disp('Indicate approximately where force balance begins (This point will be
used future plots as a reference): ')
position2=ginput(1);
forceRef=dsearchn(tim,position2(1));
% Shorten analysis duration to reduce noise at end of stress vs. strain curve
disp('Indicate where force balance ends (This will be the time up to which
stress and strain are calculated): ')
position3=ginput(1);
endAnalysis=dsearchn(tim,position3(1));

% THREE WAVE CALCULATIONS
threeWaveStress=E*(Abar*(Ei+Er)+Atrans*Et)/(2*Aspec);
threeWaveStrainRate=C0*(Ei-Er-Et)/Ls;
threeWaveStrain=C0/Ls*cumtrapz(Ei-Er-Et)*dt;
threeWaveTrueStrain=log(1+threeWaveStrain);
threeWaveTrueStress=threeWaveStress.*(1+(threeWaveStrain));

% ONE WAVE CALCULATIONS

```

```

oneWaveStress=(E*Atrans/Aspec*Et);
oneWaveStrainRate=C0/Ls*(Ei*(1-Abar/Atrans)-Er*(1+Abar/Atrans));
oneWaveStrain=C0/Ls*cumtrapz((Ei*(1-Abar/Atrans)-Er*(1+Abar/Atrans)))*dt;
oneWaveTrueStrain=log(1+oneWaveStrain);
oneWaveTrueStress=oneWaveStress.*(1+(oneWaveStrain));

% APPROXIMATE TRUE STRAIN RATES
M=analysisDuration;
for index = 2:M(1)
    threeWaveTrueStrainRate(index,1)=(abs(threeWaveTrueStrain(index))-
abs(threeWaveTrueStrain(index-1)))/dt;
    oneWaveTrueStrainRate(index,1)=(abs(oneWaveTrueStrain(index))-
abs(oneWaveTrueStrain(index-1)))/dt;
end

% PLOT THE VARIOUS STRESS, STRAIN, AND STRAIN RATE RELATIONSHIPS
figure('name','Engineering Stress')
hold on
plot(analysisTime(1:endAnalysis),(threeWaveStress(1:endAnalysis)),'b')
plot(analysisTime(1:endAnalysis),(oneWaveStress(1:endAnalysis)),'r')
plot(analysisTime(forceRef),(threeWaveStress(forceRef)),'bo')
plot(analysisTime(forceRef),(oneWaveStress(forceRef)),'ro')
title('Engineering Stress in the Specimen')
legend('Three Wave Method','One Wave Method','location','best')
xlabel('Time [microseconds]')
ylabel('Stress [MPa]')
print -dbmp16m Engineering_Stress

figure('name','True Stress')
hold on

```



```

plot(analysisTime(1:endAnalysis),(threeWaveTrueStress(1:endAnalysis)), 'b')
plot(analysisTime(1:endAnalysis),(oneWaveTrueStress(1:endAnalysis)), 'r')
plot(analysisTime(forceRef),(threeWaveTrueStress(forceRef)), 'bo')
plot(analysisTime(forceRef),(oneWaveTrueStress(forceRef)), 'ro')
title('True Stress in the Specimen')
legend('Three Wave Method','One Wave Method','location','best')
xlabel('Time [microseconds]')
ylabel ('Stress [MPa]')
print -dbmp16m True_Stress

```

```

figure('name','Engineering Strain')
hold on
plot(analysisTime(1:endAnalysis),(threeWaveStrain(1:endAnalysis)), 'b')
plot(analysisTime(1:endAnalysis),(oneWaveStrain(1:endAnalysis)), 'r')
plot(analysisTime(forceRef),(threeWaveStrain(forceRef)), 'bo')
plot(analysisTime(forceRef),(oneWaveStrain(forceRef)), 'ro')
title('Engineering Strain in the Specimen')
legend('Three Wave Method','One Wave Method','location','best')
xlabel('Time [microseconds]')
ylabel ('Strain')
print -dbmp16m Engineering_Strain

```

```

figure('name','True Strain')
hold on
plot(analysisTime(1:endAnalysis),(threeWaveTrueStrain(1:endAnalysis)), 'b')
plot(analysisTime(1:endAnalysis),(oneWaveTrueStrain(1:endAnalysis)), 'r')
plot(analysisTime(forceRef),(threeWaveTrueStrain(forceRef)), 'bo')
plot(analysisTime(forceRef),(oneWaveTrueStrain(forceRef)), 'ro')
legend('Three Wave Method','One Wave Method','location','best')
title('True Strain in the Specimen')

```

```

xlabel('Time [microseconds]');
ylabel ('Strain');
print -dbmp16m True_Strain

figure('name','Engineering Strain Rate')
hold on
plot(analysisTime(1:endAnalysis),(threeWaveStrainRate(1:endAnalysis)),'b')
plot(analysisTime(1:endAnalysis),(oneWaveStrainRate(1:endAnalysis)),'r')
plot(analysisTime(forceRef),(threeWaveStrainRate(forceRef)),'bo')
plot(analysisTime(forceRef),(oneWaveStrainRate(forceRef)),'ro')
title('Engineering Strain Rate in the Specimen')
legend('Three Wave Method','One Wave Method','location','best')
xlabel('Time [microseconds]');
ylabel ('Strain Rate [1/s]')
print -dbmp16m Engineering_Strain_Rate

figure('name','True Strain Rate')
hold on
plot(analysisTime(1:endAnalysis),(threeWaveTrueStrainRate(1:endAnalysis)),'b')
plot(analysisTime(1:endAnalysis),(oneWaveTrueStrainRate(1:endAnalysis)),'r')
plot(analysisTime(forceRef),(threeWaveTrueStrainRate(forceRef)),'bo')
plot(analysisTime(forceRef),(oneWaveTrueStrainRate(forceRef)),'ro')
title('True Strain Rate in the Specimen')
legend('Three Wave Method','One Wave Method','location','best')
xlabel('Time [microseconds]');
ylabel ('Strain Rate [1/s]')
print -dbmp16m True_Strain_Rate

figure('name','Engineering Stress Vs. Engineering Strain')
hold on

```

```

plot((threeWaveStrain(1:endAnalysis)),(threeWaveStress(1:endAnalysis)),'b')
plot((oneWaveStrain(1:endAnalysis)),(oneWaveStress(1:endAnalysis)),'r')
plot((threeWaveStrain(forceRef)),(threeWaveStress(forceRef)),'bo')
plot((oneWaveStrain(forceRef)),(oneWaveStress(forceRef)),'ro')
title('Engineering Stress vs. Engineering Strain')
legend('Three Wave Method','One Wave Method','location','best')
xlabel('Strain');
ylabel ('Stress [MPa]')
print -dbmp16m Engineering_Stress_Vs_Engineering_Strain

figure('name','True Stress vs. True Strain')
hold on
plot((threeWaveTrueStrain(1:endAnalysis)),(threeWaveTrueStress(1:endAnalysis)),
'b')
plot((oneWaveTrueStrain(1:endAnalysis)),(oneWaveTrueStress(1:endAnalysis)),'r')
plot((threeWaveTrueStrain(forceRef)),(threeWaveTrueStress(forceRef)),'bo')
plot((oneWaveTrueStrain(forceRef)),(oneWaveTrueStress(forceRef)),'ro')
title('True Stress vs. True Strain')
xlabel('True Strain');
ylabel ('True Stress [MPa]')
legend('Three Wave Method','One Wave Method','location','best')
print -dbmp16m True_Stress_Vs_True_Strain

% Create .txt files in work folder containing the one wave and three wave
results
oneWave = [oneWaveStrain(1:endAnalysis) oneWaveStrainRate(1:endAnalysis)
oneWaveStress(1:endAnalysis) oneWaveTrueStrain(1:endAnalysis)
oneWaveTrueStrainRate(1:endAnalysis) oneWaveTrueStress(1:endAnalysis)];
threeWave = [threeWaveStrain(1:endAnalysis) threeWaveStrainRate(1:endAnalysis)
threeWaveStress(1:endAnalysis) threeWaveTrueStrain(1:endAnalysis)

```

```
threeWaveTrueStrainRate(1:endAnalysis) threeWaveTrueStress(1:endAnalysis)];  
combination = [threeWaveStrain(1:endAnalysis) threeWaveStrainRate(1:endAnalysis)  
oneWaveStress(1:endAnalysis) threeWaveTrueStrain(1:endAnalysis)  
threeWaveTrueStrainRate(1:endAnalysis) oneWaveTrueStress(1:endAnalysis)];  
save OneWaveB.txt oneWave -ASCII -TABS  
save ThreeWaveB.txt threeWave -ASCII -TABS  
save CombinationB.txt combination -ASCII -TABS
```

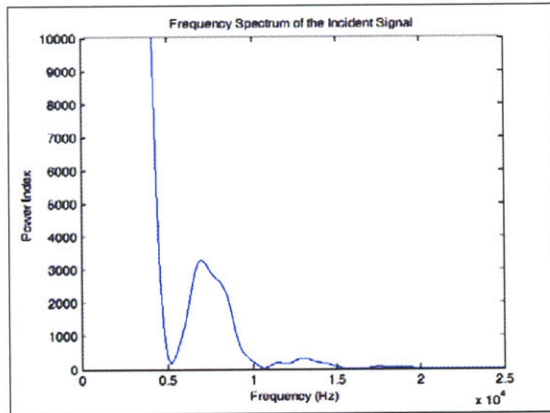
## Appendix C

# CHARACTERIZE.m Procedure

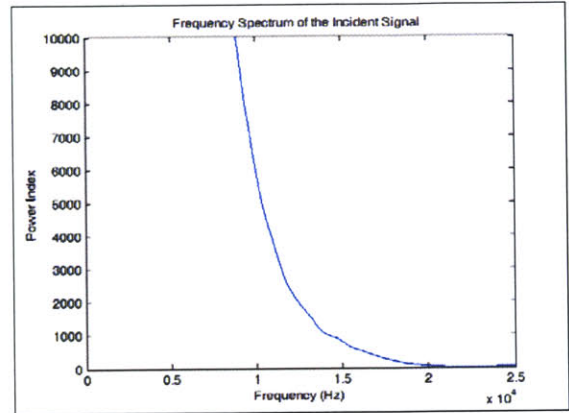
The first step in the CHARACTERIZE.m code is to clear all variables in MATLAB of any possible residual definitions and to close all previous plots. Next, the length scales of the bar, including strain gauge placement and length of the bar are established. Parameters for zeroing the baseline and isolating the pulses are then defined utilizing the same method employed in ALSHPB.m. Next, the response range of the signal conditioner used for the trials is defined. This value is later used to determine what frequencies the calculations are valid up to and where the calculations should be capped. The vector length of the signal after being padded with zeroes is then defined to be "signalSize". It is important that this value match up to the value used in the PMMASHPB.m code because it, in conjunction with the signal's time duration, determines the frequencies for which  $\gamma(\omega)$  is calculated.

With these parameters in place, the characterization trial to be examined is then selected by the user and loaded into the program. The selection of an appropriate trial is very important in obtaining accurate  $\gamma(\omega)$  values. Trials using long striker bars are characterized by a lack of higher frequency components (Figure C-1) which in turn results in calculations of  $\gamma(\omega)$  that are valid for a smaller frequency range than those calculations which utilize the signals from the smaller striker bars (Figure C-2).

Once the appropriate trial has been loaded, the time portion of the signal is changed into microseconds and zeroed, the time interval between samples is determined, and the strain portion signal is zeroed and plotted in the same way described for the ALSHPB.m code. Next, the first 5000 microseconds of the signal are resampled to occupy a vector that is "signalSize"

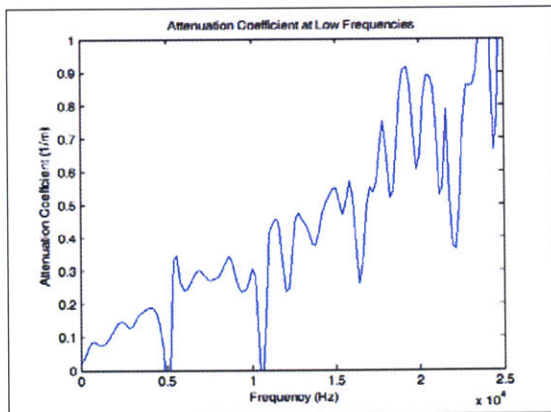


(a) Frequency power spectrum of the incident pulse using an 8" (0.2032 m) PMMA striker bar.

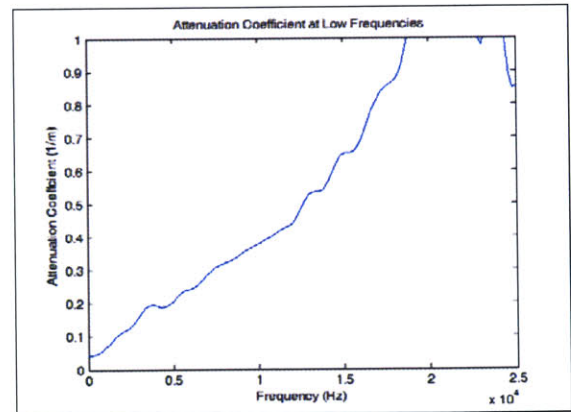


(b) Frequency power spectrum of the incident pulse using an 2" (0.0504 m) striker bar.

Figure C-1: Shorter striker bars allow for a more complete frequency spectrum.

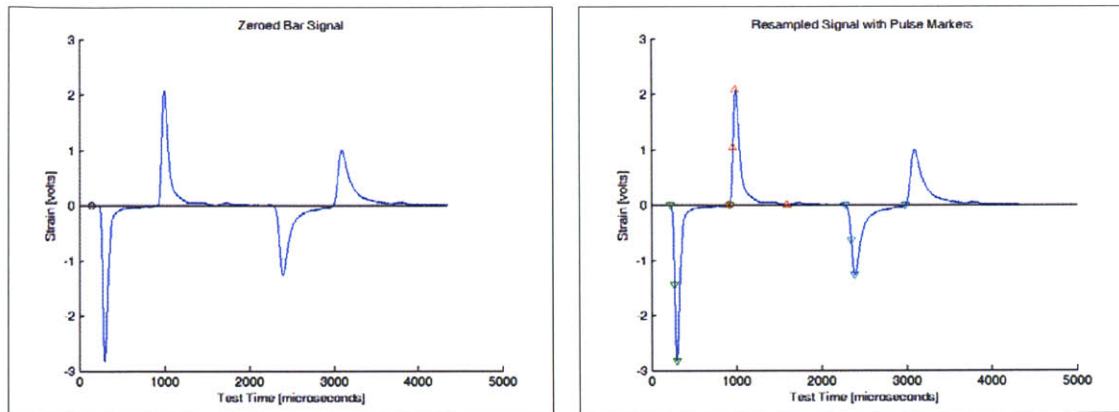


(a) Alpha, the real component of the propagation coefficient, calculated using an 8" (0.2032 m) PMMA striker bar.



(b) Alpha, the real component of the propagation coefficient, calculated using a 2" (0.0504 m) PMMA striker bar.

Figure C-2: A more complete frequency spectrum allows for more accurate calculation of the propagation coefficient gamma.

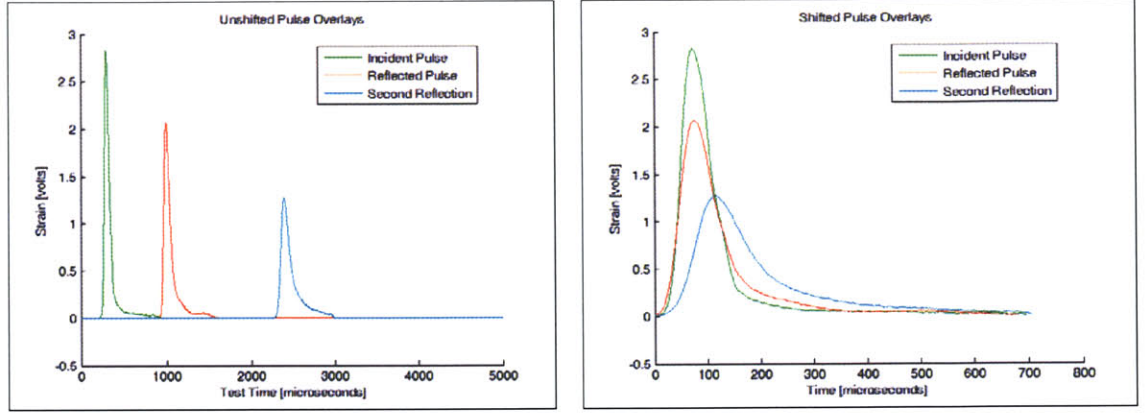


(a) The original signal from the oscilloscope as plotted by MATLAB. (b) The resampled signal after padding with zeros up to the 5000 microseconds mark.

Figure C-3: The original and resampled signals are plotted side-by-side to assure they match.

in length. This is achieved using an interpolation function called out as `ValAtTime`. This function, along with two others utilized further on, was personally furnished by Bacon and can be found in Appendix G. It should be noted that if the original signal is not 5000 microseconds in duration the end of the vector is padded with zeros up to the 5000 microsecond mark. In addition, the resampled signal is plotted so that the user may visually check that it is a match to the original (Figure C-3). The incident, reflected, and second reflection pulses are then isolated utilizing the same algorithm employed in the `ALSHPB.m` code. Each of these pulses is separated and stored in two distinct formats. One format with the time information being zeroed to the start of the individual pulse, and the other with the time information being stored as that of the original experimental scale. These shifted and unshifted pulses are then plotted for the user to visually verify (Figure C-4).

The next step in the algorithm is to take the Fourier transform of the unshifted incident and reflected pulses. These transforms are then `fftshifted`, and the corresponding frequencies are calculated using a simple algorithm adopted from Bacon's method. Next, the non-negative frequencies, and the corresponding portions of the Fourier transforms, are isolated and saved. From this value the frequency power spectrums are then calculated by squaring the magnitude of the transform and plotting the result against the corresponding non-negative frequencies (see Figure C-1). At this point it is important that the user inspect the frequency power spectrums to assure that frequency components are safely situated away from the conditioner's maximum



(a) Unshifted pulse overlays.

(b) Shifted pulse overlays.

Figure C-4: Pulse overlays are plotted for the user to check visually.

frequency response. If the frequency components are still of a significant magnitude near the maximum frequency response of the signal conditioner, it may mean that a meaningful portion of the signal is not being properly recorded.

If the frequency spectrum is appropriate, the transfer function,  $H^*(\omega)$ , is then calculated in accordance with equation (2.29): by dividing the negative of the reflected pulse's Fourier transform by the Fourier transform of the incident pulse. To avoid errors due to fftshifting, this calculation is only carried out for the portions of the transform corresponding to non-negative frequencies. In addition, to avoid errors due to division by zero during the calculation of  $H^*(\omega)$ , all relevant zeroes are set to the smallest nonzero value available in MATLAB.

Using a combination of equations (2.22) and (2.29), we then calculate the attenuation coefficients,  $\alpha(\omega)$ , by taking the negative natural log of  $H^*(\omega)$  and dividing it by the distance the pulse has traveled; namely twice the distance from the strain gauge to the end of the bar off which the pulse will be reflected:

$$\alpha(\omega) = -\frac{\ln(|H^*(\omega)|)}{2d} \quad (\text{C.1})$$

Similarly, the wave number,  $k(\omega)$ , can be calculated by dividing the transfer function's angle by twice the distance from the strain gauge to the sample:

$$k(\omega) = \frac{\arg(H^*(\omega))}{2d} \quad (\text{C.2})$$



Before implementing this calculation, however, it is necessary to numerically unwrap the angle of  $H^*(\omega)$  in order to assure that there are no absolute jumps between consecutive entries which are greater than  $\pi$  radians. This is necessary due to MATLAB's assumption when calculating the angle that the value will always be between  $-\pi$  and  $\pi$ .

The wave speed,  $c(\omega)$ , is then obtained by dividing the angular frequency by the wave number:

$$c(\omega) = \frac{\omega}{k(\omega)} \quad (\text{C.3})$$

where the angular frequency,  $\omega$ , is calculated by multiplying  $2\pi$  by the non-negative frequencies, isolated earlier.

Next, because the  $\alpha(\omega)$ ,  $k(\omega)$ , and  $c(\omega)$  values just calculated are only valid for the non-negative frequencies, they must be properly reflected onto the full frequency spectrum. This is done by applying `MakeEven.m` to  $\alpha(\omega)$  and  $c(\omega)$ , and `MakeOdd.m` to  $k(\omega)$  and the unwrapped angle of the transfer function. `MakeEven.m` and `MakeOdd.m` are two simple functions provided by Bacon which calculate the values for the negative frequencies by assuming the function to be either even or odd respectively. The code for both of these functions can be found in Appendix G. Once the negative frequency values for these parameters have been calculated, the unwrapped angle, the phase velocity, the attenuation coefficient, and the wave number are all fftshifted and plotted against the full frequency spectrum to verify that they have been properly matched to the appropriate frequencies (Figure C-5, Figure C-7 (a), Figure C-8 (a), and Figure C-9 (a)).

Because the characterization trials for PMMA rarely, if ever, contain significant frequency components above 25 kHz, the resulting Fourier transforms are generally very small in magnitude at the higher level frequencies. Consequently, the transfer function, which is a ratio of two of these transforms, can be very noisy at the higher frequencies. This results in unreliable calculations for the attenuation coefficient, wave number, and phase velocity at high frequencies (note this behavior above 25 kHz in Figure C-6, Figure C-7 (a), Figure C-8 (a), and Figure C-9 (a)). Bearing this in mind it was decided that the values of  $c(\omega)$  and  $\alpha(\omega)$  would be kept constant for frequencies above a threshold value equal to half of the signal conditioner's maximum response range (Figure C-7 (b) and Figure C-8 (b)) and assigned their original values for frequencies less than the threshold frequency (Figure C-10). In addition, the wave number values

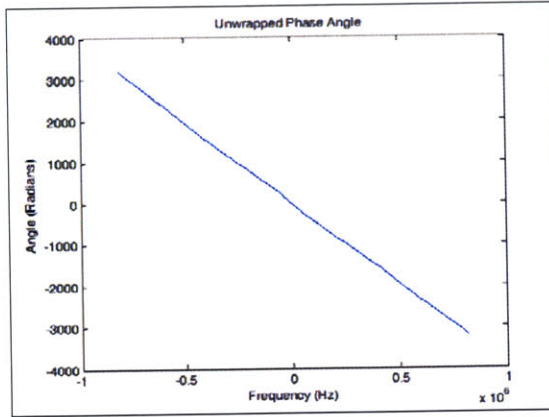
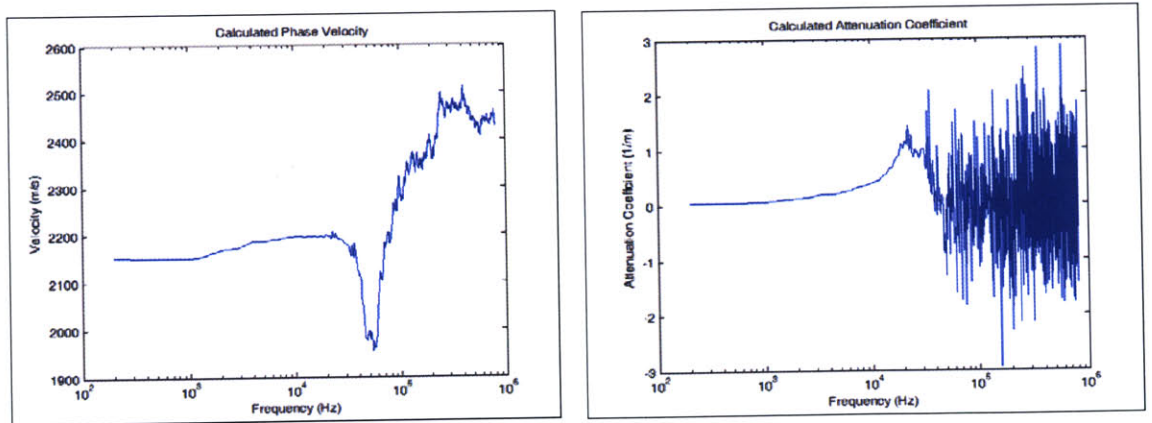
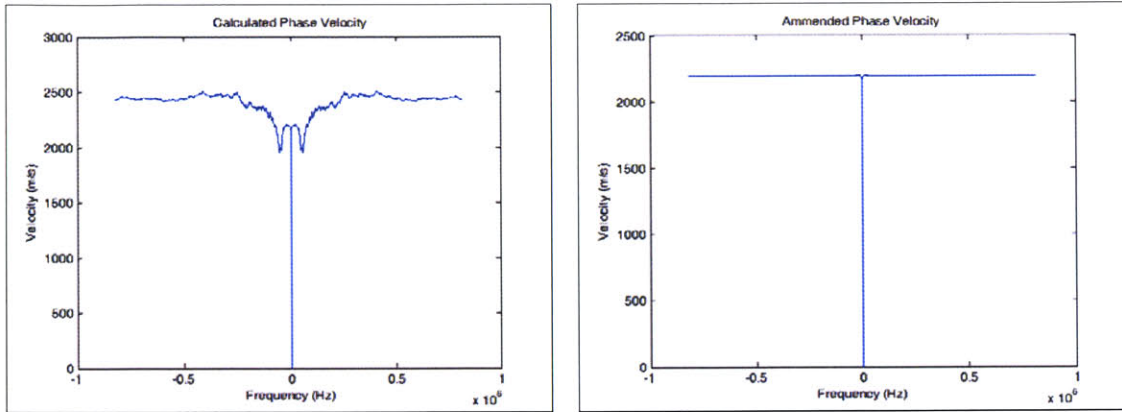


Figure C-5: The phase angle of the transfer function after numerical unwrapping.



(a) Phase velocities in the higher frequency range. (b) Attenuation coefficients in the higher frequency range.

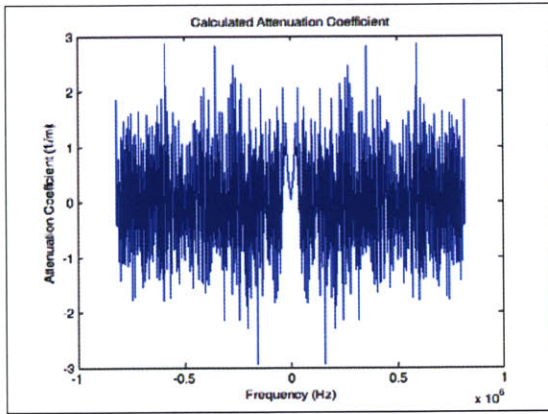
Figure C-6: The calculated components of gamma become extremely unreliable at high frequencies.



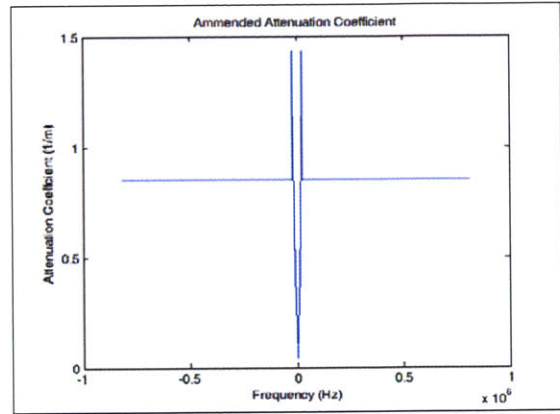
(a) The calculated phase velocity is extremely noisy at high frequencies. (b) The ammended phase velocity removes this noise above the threshold frequency of 25 kHz.

Figure C-7: Ammendment of the high frequency phase velocities.

were also updated to match the amended phase velocities (Figure C-9(b)). This approach was found to be particularly effective at eliminating the unrealistic amplification of high frequencies associated with using the negative attenuation coefficients found in the original calculations. The result is a much more reliable and less noisy prediction of strain within the bar (Figure C-11).

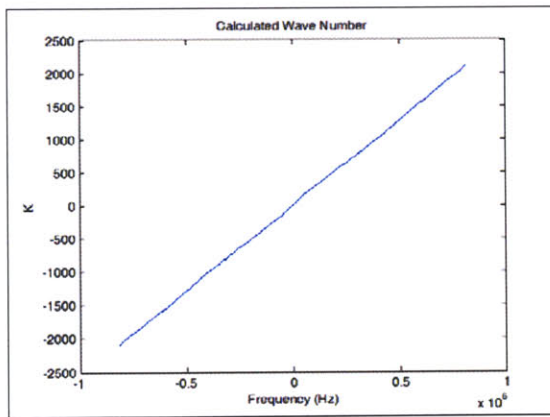


(a) The calculated attenuation coefficient is extremely noisy at high frequencies.

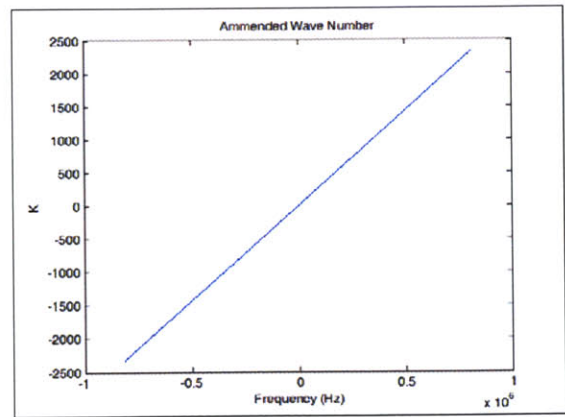


(b) The ammended attenuation coefficient removes this noise above the threshold frequency of 25 kHz.

Figure C-8: Ammendment of the high frequency attenuation coefficients.

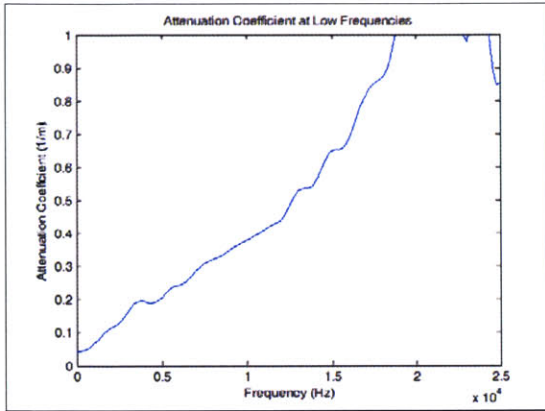


(a) The original calculations for wave number.

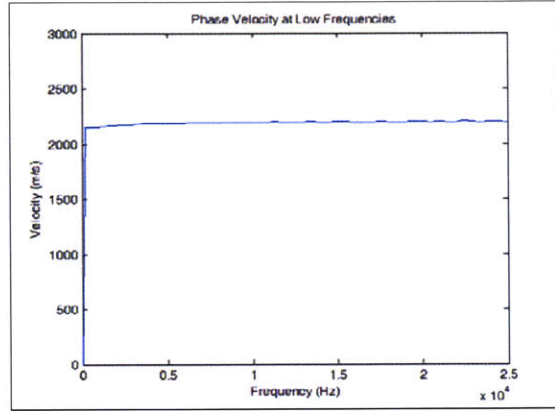


(b) The updated wave number after taking into account the ammended phase velocities.

Figure C-9: The wave number is also updated in accordance with the ammended phase velocities.

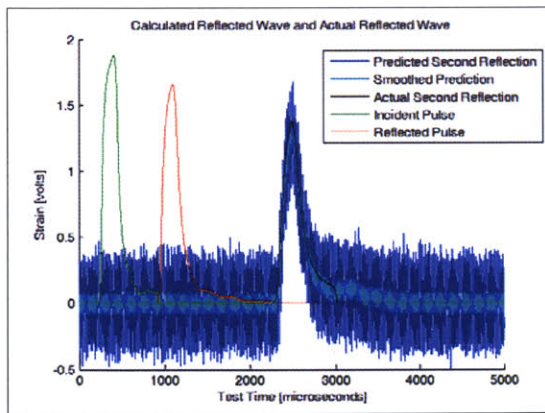


(a) Low frequency attenuation coefficients.

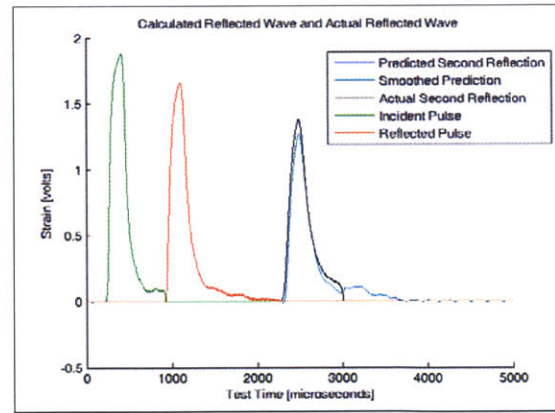


(b) Low frequency phase velocities.

Figure C-10: Coefficients for frequencies below the threshold frequency of 25 kHz.



(a) Original prediction without the threshold frequency cap.



(b) Prediction after implementing a threshold frequency cap.

Figure C-11: Employing a threshold frequency dramatically increases accuracy of the propagation predictions.

As this demonstrates, the final check for the entire characterization process is whether or not the calculated parameters can be employed to accurately predict a strain wave that has propagated down the bar for several reflections. To do this,  $\gamma(\omega)$  is constructed by using  $\alpha(\omega)$  as the real part and  $k(\omega)$  as the imaginary part. Next,  $\gamma(\omega)$  is fftshifted so that it's indices coincide with those of the full Fourier transforms. A new transfer function for the predicted wave,  $H_2^*(\omega)$ , is then defined as follows:

$$H_2^*(\omega) = e^{-\gamma x} \quad (\text{C.4})$$

where the value of  $x$  is two times the total length of the bars. Multiplying this new transfer function by the full Fourier transform of the incident pulse gives the Fourier transform of the strain after two reflections. Taking the inverse transform of this quantity and plotting the result relative to the original pulses then gives the user an excellent indication of how accurate the characterization parameters are in predicting the dispersion and attenuation in the bar (Figure C-12).

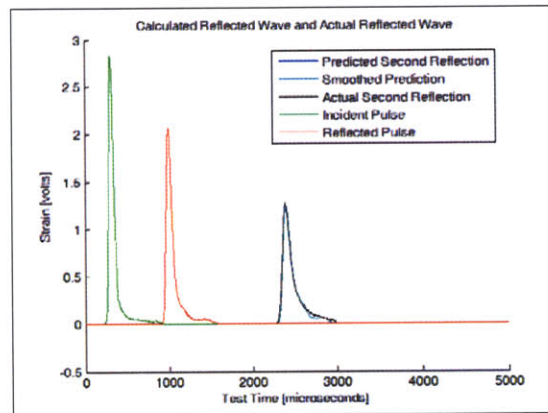


Figure C-12: The final check on the characterization parameters is their ability to accurately predict a strain wave after travelling the length of the PMMA bar twice. This prediction was obtained using the coefficients from a 2" striker bar characterization trial.

The final step for CHARACTERIZE.m is to save the frequency and  $\alpha(\omega)$  vectors to the file "alpha\_.m"; the frequency and  $k(\omega)$  vectors to the file "kappa\_.m"; and the frequency,  $\text{Re}(\gamma(\omega))$ , and  $\text{Im}(\gamma(\omega))$  vectors to the file "gamma\_.m"; where ' \_ ' is I2 or T2 for the incident

and transmission bars respectively.





## Appendix D

# CHARACTERIZE.m Code

```
% CHARACTERIZE.m
% Timothy P. M. Johnson
% Institute for Soldier Nanotechnologies
% Massachusetts Institute of Technology
% June 2005

clear all
close all

d = 0.7620; % Distance from strain gauge to the sample in meters
l = 2.2828; % Total bar length in meters
x = 2*l;    % Distance travelled to the cross section of interest in meters

% PARAMETERS FOR ZEROING THE PULSE
inciLeading=150;    % Number of initial points used to calculate incident
baseline
inciSlope=0.5;     % Location of reference point on incident slope, as a
fraction of signal minimum
reflSlope=0.5;     % Location of reference point on reflected slope, as a
fraction of signal maximum
```

```

percentTrigger=0.00;% Percent deviation from zero that signals the start of a
pulse

% SIGNAL PROCESSING PARAMETERS
conditionerRange = 50000; % Frequency range of the data acquisition hardware
signalSize = 2^13; % Size of signal after padding
smoothingPts=25; % Number of points used in the moving average
smoothing function

% CAPTURING INCIDENT AND REFLECTED PULSES
[fname, fpath]=uigetfile('*.asc'); % Read the incident bar pulses; the data is
time (seconds) vs. strain (in volts!)
channel1=load([fpath fname]);
tim=channel1(:,1);
dt=(tim(end)-tim(1))/(length(tim)-1); % dt is the time interval between points
in seconds
tim=tim-tim(1); % Zero the time
tim=tim*10^6;\quad % Changes time from seconds to microseconds
EPS=channel1(:,2);

% BAR SIGNAL AND PULSE MARKERS
figure('name','Zeroed Bar Signal')
hold on
title('Zeroed Bar Signal');
xlabel('Test Time [microseconds]');
ylabel('Strain [volts]');

% Calculate incident pulse baseline, for zeroeing
flatBaseline=polyfit(tim(1:inciLeading),EPS(1:inciLeading),0); % Using
y = constant method

```

```

EPS=EPS-flatBaseline(1);          % Zeros the strain
plot(tim,EPS)
plot(tim,0,'k')                  % Plots black baseline
plot(tim(inciLeading),0,'ko')    % Places black 'o' marker at last point used
in calculating baseline (allows user to see if larger inciLeading should be
used)

% RESAMPLE PULSE TO BE 5000 MICROSECONDS IN DURATION AND HAVE
"SIGNALSIZE" POINTS
newdt=(5000E-6)/(signalSize-1);
newtim=transpose(0:newdt:5000E-6);
% ValAtTime function courtesy of C. Bacon:
newEPS=ValAtTime(EPS(1:dsearchn(tim,5000)),dt,newtim);
newtim=newtim*10^6; % Changes newtim to microseconds
tim=newtim;
EPS=newEPS;
figure('name','Resampled Signal with Pulse Markers')
hold on
plot(newtim,newEPS)
plot(newtim,0,'k')
title('Resampled Signal with Pulse Markers')
xlabel('Test Time [microseconds]');
ylabel('Strain [volts]');

% Locate reference point on incident slope
[minimum,centerIncidentIndex]=min(EPS);
plot(tim(centerIncidentIndex),minimum,'gv')
lim1=inciSlope*minimum;
ind=1;
while EPS(ind)>lim1

```

```

    ind=ind+1;
end
ipoint=ind;
plot(tim(ipoint),EPS(ipoint),'gv')
% Back up to find exact start of incident pulse
ind=ipoint;
while EPS(ind)<percentTrigger*minimum
    ind=ind-1;
end
startIncident=ind;
plot(tim(startIncident),EPS(startIncident),'gv')
% Move up to find finish of incident pulse
ind=ipoint;
while EPS(ind)<0
    ind=ind+1;
end
endIncident=ind;
plot(tim(endIncident),EPS(endIncident),'gv')

iTime=tim(startIncident:endIncident)-tim(startIncident);
onlyIncident=EPS(startIncident:endIncident);
incident=zeros(signalSize,1);
incident(startIncident:endIncident)=onlyIncident;

% Locate reference point on reflected slope
[maximum,centerReflectedIndex]=max(EPS);
plot(tim(centerReflectedIndex),maximum,'r^')
lim1=reflSlope*maximum;
ind=ipoint;
while EPS(ind)<lim1

```

```

    ind=ind+1;
end
rpoint=ind;
plot(tim(rpoint),EPS(rpoint),'r^')
% Back up to find the start of the reflected pulse
ind=rpoint;
while EPS(ind)>percentTrigger*maximum
    ind=ind-1;
end
startReflected=ind;
plot(tim(startReflected),EPS(startReflected),'r^')
% Move up to find finish of reflected pulse
ind=rpoint;
while EPS(ind)>0
    ind=ind+1;
end
endReflected=ind;
plot(tim(endReflected),EPS(endReflected),'r^')

rTime=tim(startReflected:endReflected)-tim(startReflected);
onlyReflected=EPS(startReflected:endReflected);
reflected=zeros(signalSize,1);
reflected(startReflected:endReflected)=onlyReflected;

% Find second negative pulse (after pulse is reflected twice)
flatEPS=EPS;
flatEPS(startIncident:endIncident)=0;
[minimum2,centerIncidentIndex2]=min(flatEPS);
plot(tim(centerIncidentIndex2),minimum2,'cv')
lim1=inciSlope*minimum2;

```

```

ind=1;
while flatEPS(ind)>lim1
    ind=ind+1;
end
ipoint=ind;
plot(tim(ipoint),EPS(ipoint),'cv')

ind=ipoint;
while flatEPS(ind)<percentTrigger*minimum
    ind=ind-1;
end
startIncident2=ind;
plot(tim(startIncident2),EPS(startIncident2),'cv')

ind=ipoint;
while flatEPS(ind)<0
    ind=ind+1;
end
endIncident2=ind;
plot(tim(endIncident2),EPS(endIncident2),'cv')

iTime2=tim(startIncident2:endIncident2)-tim(startIncident2);
onlyIncident2=EPS(startIncident2:endIncident2);
incident2=zeros(signalSize,1);
incident2(startIncident2:endIncident2)=onlyIncident2;

% UNSHIFTED PULSE OVERLAYS
figure('name','Unshifted Pulse Overlays')
hold on
plot(tim(1:signalSize),-incident,'g')

```

```

plot(TIM(1:signalSize),reflected,'r')
plot(TIM(1:signalSize),-incident2,'c')
title('Unshifted Pulse Overlays')
xlabel('Test Time [microseconds]')
ylabel('Strain [volts]')
legend('Incident Pulse','Reflected Pulse','Second Reflection','location','best')

% SHIFTED PULSE OVERLAYS
figure('name','Shifted Pulse Overlays')
hold on
plot(iTime,-onlyIncident,'g')
plot(rTime,onlyReflected,'r')
plot(iTime2,-onlyIncident2,'c')
title('Shifted Pulse Overlays')
xlabel('Time [microseconds]')
ylabel('Strain [volts]')
legend('Incident Pulse','Reflected Pulse','Second Reflection','location','best')

% FOURIER TRANSFORM OF INCIDENT SIGNAL
figure('name','Incident Transform')
IFourier=fft(incident);
iFourier=fftshift(IFourier);
Npts=length(iFourier);
% Handling folding frequency based on C. Bacon's fftfrequencies.m
Nshanon=ceil(Npts/2);
T=(TIM(end)-TIM(1))*10^-6;
df=1/T;
for q=1:Nshanon
\quad freq(q,1)=(q-1)*df;
end

```

```

for q=Nshanon+1:Npts
\quad freq(q,1)=(q-1-Npts)*df;
end
freq=fftshift(freq);
iFreq=freq(find(freq>=0));
iFourier=iFourier(find(freq>=0));
iPower=abs(iFourier).^2;
plot(iFreq,iPower)
title('Frequency Spectrum of the Incident Signal');
xlabel('Frequency (Hz)');
ylabel('Power Index');
axis([0 conditionerRange/2 0 1E4]);

freqz=iFreq;

% FOURIER TRANSFORM OF REFLECTED SIGNAL
figure('name','Reflected Transform')
RFourier=fft(reflected);
rFourier=fftshift(RFourier);
rFreq=freq(find(freq>=0));
rFourier=rFourier(find(freq>=0));
rPower=abs(rFourier).^2;
plot(rFreq,rPower)
title('Frequency Spectrum of the Reflected Signal');
xlabel('Frequency (Hz)');
ylabel('Power Index');
axis([0 conditionerRange/2 0 1E4]);

% CALCULATE DISPERSION AND ATTENUATION COEFFICIENTS USING BACON'S METHOD
iFourier(find(iFourier==0))=eps;

```



```

transferFunctionH=-rFourier./iFourier;
transferFunctionH(find(transferFunctionH==0))=eps;

alpha=-log(abs(transferFunctionH))/(2*d);
unwrappedAngle=unwrap(angle(transferFunctionH));
k=-(unwrappedAngle)./(2*d);
k(find(k==0))=eps;
c=2*pi*freqz./k;

% MakeEven and MakeOdd Functions were courtesy of C. Bacon
alpha=fftshift(MakeEven(alpha));
c=fftshift(MakeEven(c));
unwrappedAngle=fftshift(MakeOdd(unwrappedAngle));
k=fftshift(MakeOdd(k));

% UNWRAPPED ANGLE
figure('name','Phase Angle')
plot(freq,unwrappedAngle)
title('Unwrapped Phase Angle');
xlabel('Frequency (Hz)');
ylabel('Angle (Radians)');

% PHASE VELOCITY
figure('name','Calculated C')
plot(freq,c)
title('Calculated Phase Velocity')
xlabel('Frequency (Hz)')
ylabel('Velocity (m/s)')

% Assign values of C artificially above the Nyquist Frequency:

```

```

c(find(abs(freq)>=conditionerRange/2))=c(dsearchn(freq,conditionerRange/2));
figure('name','Ammended C')
plot(freq,c)
title('Ammended Phase Velocity')
xlabel('Frequency (Hz)')
ylabel('Velocity (m/s)')

figure('name','C')
plot(freq,c)
title('Phase Velocity at Low Frequencies');
xlabel('Frequency (Hz)');
ylabel('Velocity (m/s)')
axis([0 conditionerRange/2 0 3000])

% ATTENUATION COEFFICIENT
figure('name','Calculated Alpha')
plot(freq,alpha)
title('Calculated Attenuation Coefficient')
xlabel('Frequency (Hz)')
ylabel('Attenuation Coefficient (1/m)')

% Assign values of alpha artificially above the Nyquist Frequency:
alpha(find(abs(freq)>=conditionerRange/2))=
alpha(dsearchn(freq,conditionerRange/2));
figure('name','Ammended Alpha')
plot(freq,alpha)
title('Ammended Attenuation Coefficient')
xlabel('Frequency (Hz)')
ylabel('Attenuation Coefficient (1/m)')

```

```

figure('name','Alpha')
plot(freq,alpha)
title('Attenuation Coefficient at Low Frequencies');
xlabel('Frequency (Hz)');
ylabel('Attenuation Coefficient (1/m)');
axis([0 conditionerRange/2 0 1])

% WAVE NUMBER
figure('name','Calculated Wave Number')
plot(freq,k)
title('Calculated Wave Number')
xlabel('Frequency (Hz)')
ylabel('K')

c(find(c==0))=eps;
k=2*pi*freq./c;
figure('name','Ammended Wave Number')
plot(freq,k)
title('Ammended Wave Number')
xlabel('Frequency (Hz)')
ylabel('K')

gamma=ifftshift(complex(alpha,k));
xTransferFunctionH=exp(-gamma*x);

% MOVING SIGNAL AND TAKING THE INVERSE TRANSFORM
fourierStrain=IFourier.*(xTransferFunctionH);
strainAtX=(ifft(fourierStrain));

figure('name','Comparison')

```

```

hold on
plot(tim(1:signalSize),-strainAtX)
plot(tim(1:signalSize),-smooth(strainAtX,smoothingPts),'c')
plot(tim(1:signalSize),-incident2,'k')
plot(tim(1:signalSize),-incident,'g')
plot(tim(1:signalSize),reflected,'r')
title('Calculated Reflected Wave and Actual Reflected Wave')
xlabel('Test Time [microseconds]')
ylabel('Strain [volts]')
legend('Predicted Second Reflection','Smoothed Prediction','Actual Second
Reflection', 'Incident Pulse', 'Reflected Pulse','location','best')

% Create .txt files in work folder containing parameters
cd(fpath)
A = [ifftshift(freq) ifftshift(alpha)];
K = [ifftshift(freq) ifftshift(k)];
G = [ifftshift(freq) real(gamma) imag(gamma)];
save alpha.txt A -ASCII -TABS
save kappa.txt K -ASCII -TABS
save gamma.txt G -ASCII -TABS

```

## Appendix E

# PMMASHPB.m Procedure

Once the appropriate propagation coefficients have been calculated and saved for both the incident and transmission bars, the values are then used in evaluating the data for actual specimen trials conducted on the PMMA pressure bars. The trials are saved in ASCII format and analyzed using the PMMASHPB.m code described here. A full transcript of PMMASHPB.m is found in Appendix F.

Similar to the ALSHPB.m code, PMMASHPB.m first clears all previous plots and variables before prompting the user to enter the diameter and length of the specimen being evaluated. Once entered, these values are converted to SI units and the cross sectional area is calculated. Next, the placement of the strain gauge, diameter of the bar, cross sectional area of the bar, and density of bar are established within the code. At this point the user is then prompted to load the proper propagation coefficients for the incident bar. Having loaded this file, the values of frequency,  $\alpha(\omega)$ , and  $k(\omega)$  are assigned to vectors and fftshifted so that they are arranged linearly with the values corresponding to the largest magnitude negative frequencies first and those corresponding to the largest magnitude positive frequency last. Next, in accordance with the method outlined in section 2.5, the transfer functions corresponding to the forward moving pulse transform,  $\tilde{P}(\omega)$ , and backwards moving pulse transform,  $\tilde{N}(\omega)$ , are defined to be  $e^{-\gamma d}$  and  $e^{\gamma d}$ , respectively. Here  $d$  is again the distance from the stain gauge to the sample interface.

The values of  $\gamma^2$  are then calculated by squaring the values in the vector  $\gamma$  and ifftshifting the result. Similarly,  $\omega$  is calculated by multiply the frequency vector by  $2\pi$  and ifftshifting the result. Finally,  $\omega^2$  is then calculated by repeating this calculation and squaring the entries of

the vector. The purpose of ifftshifting these three vectors is to provide a convolution when they are later multiplied, in either the form of a complex Young's modulus or a velocity coefficient, with the "transferred" Fourier strains.

Next, the complex Young's modulus is calculated:

$$E^* = -\frac{\rho\omega^2}{\gamma^2} \quad (\text{E.1})$$

As is "V1Coef", the velocity coefficient:

$$V1Coef = -\frac{i\omega}{\gamma} \quad (\text{E.2})$$

where in this case the  $\gamma$  values used are ifftshifted to match the indicial format of  $\omega$ .

To assure that all of the vectors have been saved corresponding to the proper frequency components, the results are then plotted. First, the frequency vector is plotted against its indices (Figure E-1). Next, the  $\omega^2$  values are plotted relative to the frequencies with which they correspond (Figure E-2). And finally the attenuation coefficients,  $\alpha(\omega)$ , and phase velocities,  $c(\omega)$ , are plotted relative to the frequencies to which they correspond (see Figure C-8(b) and Figure C-7(b) for an example). These last two plots enable the user to check that the correct coefficient file was loaded and that it is being handled properly. Once this is complete the user specifies the second set of propagation coefficients and the process is repeated for the case of the transmission bar.

With the characteristics of the bar defined, PMMASHPB.m now establishes the parameters for zeroing the pulses in the same manner used for the ALSHPB.m code. Next, the conditioner's maximum frequency response range and the signal size after padding is defined. The user is then prompted to select the incident pulse file to be analyzed. Once the data has been loaded, the time is zeroed and changed to microseconds. Next, the strain signal is zeroed and resampled using Bacon's ValAtTime function. The resulting vector is to be 5000 microseconds in duration and consist of many data points as defined by the "signalSize" variable. This approach is to ensure that the data matches the format used in the files previously generated by CHARACTERIZE.m. Working on this new strain vector and employing the same algorithm as the ALSHPB.m code, the start, end, and reference points are found for both the incident

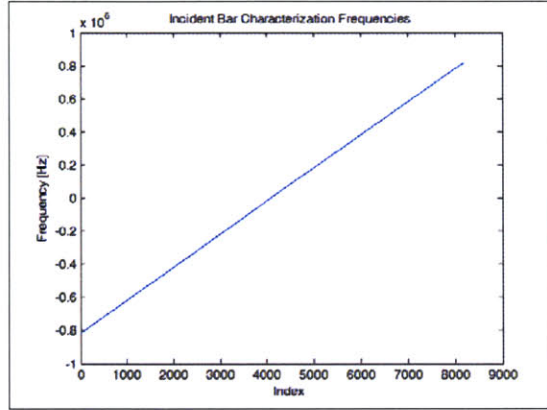


Figure E-1: The frequency vector is plotted for the user to visually check.

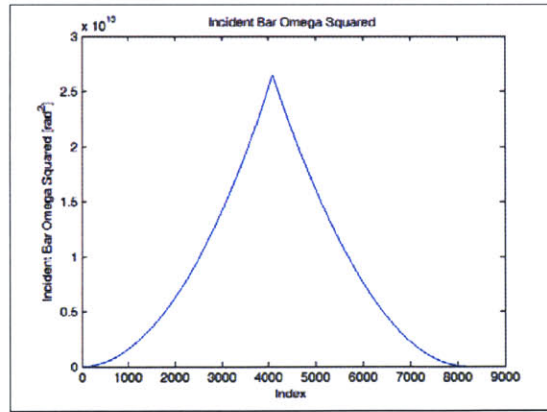


Figure E-2: The omega squared values are also plotted for the user to visually check.

and reflected pulses. The technique is then repeated on the user specified transmission file to isolate the transmission pulse.

To verify that the incident, reflected, and transmission pulses were captured correctly, they are plotted in the same format employed in the ALSHPB.m code (see Figure A-3). Assuming they were accurately isolated, the unshifted pulses are then transformed into the frequency domain using an algorithm identical to the one in CHARACTERIZE.m. Next, to make sure the signal's components fall within the response range of both the signal conditioner and the propagation coefficients, the frequency power spectrum of each transforms is plotted (see Figure C-1 for an example).

With the full Fourier transforms having just been calculated, the incident transform,  $\tilde{P}(\omega)$ , and reflected transform,  $\tilde{N}(\omega)$ , are then multiplied by their respective transfer functions and summed (see equation (2.26) where  $x$  is the positive distance from the strain gauge to the specimen). This value is then multiplied by the cross sectional area and complex Young's modulus of the incident bar, both of which were calculated earlier. The result is the fftshifted Fourier transform of the force at the incident bar-specimen interface. The inverse Fourier transform of this vector after it has been ifftshifted is calculated and then plotted to show the forces on the front face of the specimen (Figure E-3). The Fourier transform of the transmission pulse is used in a similar manner to calculate the forces on the rear face of the specimen and the results are also shown on the previous plot. It is worth noting, however, that in conducting the transmission bar calculations, the  $\tilde{P}(\omega)$  pulse is taken to be zero and  $x$  is taken as the negative distance from the strain gauge to the specimen. Finally, the user is requested to examine the plot and choose where force balance begins and ends. The beginning of force balance will be marked in subsequent plots by an open dot, and the stress, strain, and strain rate calculations will only be conducted up to the selected end point.

At this point in the code a similar technique is used to calculate the velocities for the front and rear faces of the specimen. The two differences are that "V1Coef" and "V2Coef" are used in place of the complex Young's modulus times area and that the "transferred" Fourier strains are subtracted from one another rather than added (see equation 2.25). From this point the inverse Fourier transform of the ifftshifted results are again calculated, this time yielding the velocities. Similar to the force balance calculation, the results for both faces are plotted



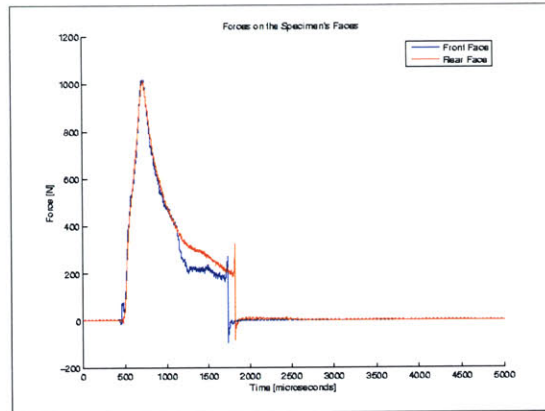


Figure E-3: The calculated front and rear forces on the specimen are plotted for the user to verify dynamic equilibrium.

together on one figure (Figure E-4).

Next, utilizing equations (2.3) and (2.5), the engineering strain rate and stress within the specimen are calculated. Engineering strain is then calculated by integrating the strain rate with MATLAB's cumtrapz function. The true strain, true strain rate, and true stress are then calculated from the engineering values in the same way as in ALSHPB.m. The results for strain, strain rate, and stress are plotted against time in three separate figures with "engineering" quantities being shown in blue and the "true" quantities being shown in red (Figures E-5, E-6, and E-7). For the final two charts, the engineering stress vs. engineering strain is plotted in blue and the approximated true stress vs. true strain is shown on a separate figure in red. The vector results are then saved to a \*.txt file with engineering strain followed by engineering strain rate, engineering stress, true strain, true strain rate, and finally the approximated true stress.

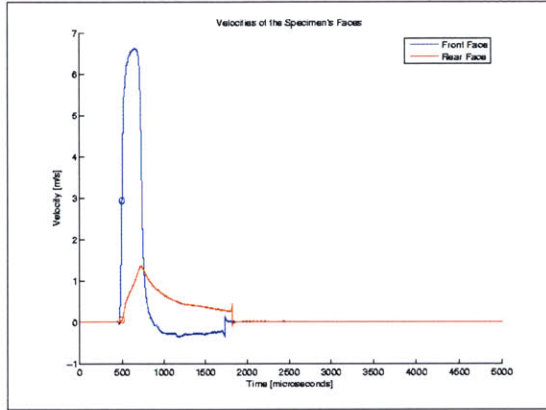


Figure E-4: The calculated front and rear face velocities are plotted for inspection.

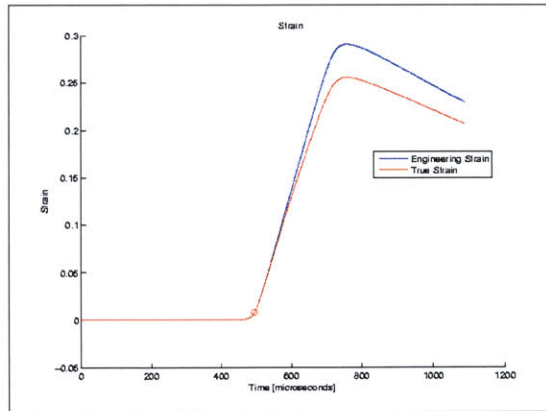


Figure E-5: The engineering and true strains are plotted side by side against time.

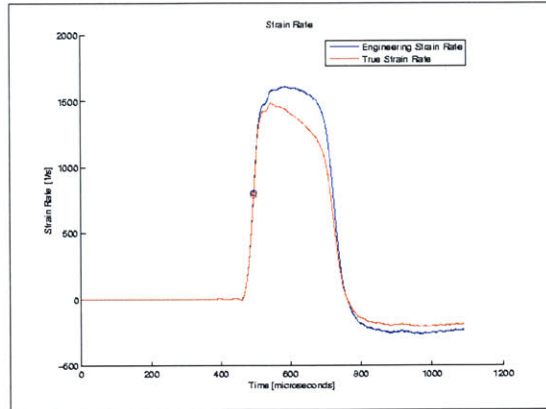


Figure E-6: The engineering and true strain rates are plotted side by side against time.

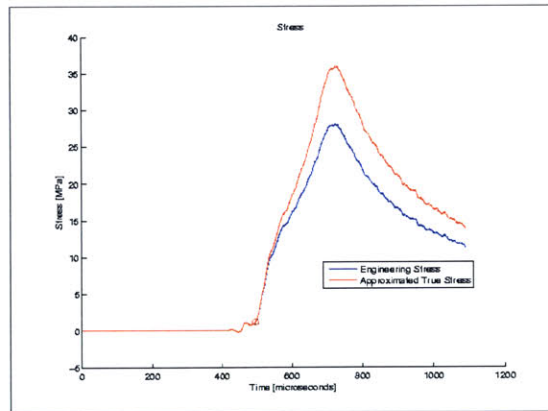


Figure E-7: The engineering and approximated true stresses are plotted side by side against time.

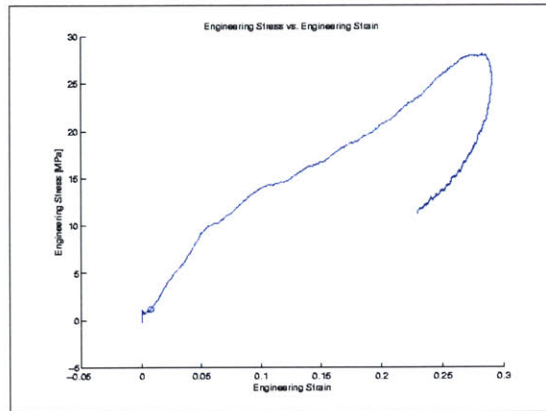


Figure E-8: Engineering stress vs. engineering strain as calculated by PMMASHPB.m for a trial on a PU specimen.

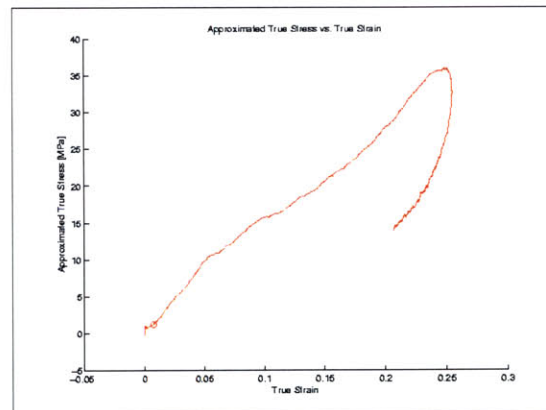


Figure E-9: Approximated true stress vs. true strain as calculated by PMMASHPB.m for the same PU trial.

## Appendix F

### PMMASHPB.m Code

```
% PMMASHPB.m
% Timothy P. M. Johnson
% Institute for Soldier Nanotechnologies
% Massachusetts Institute of Technology
% June 2005
% NOTE SIGN CONVENTION: Compression is Positive

clear all
close all

% SPECIMEN PARAMETERS
Dsmm=input('What is the diameter of the specimen in millimeters? ');
Ds=Dsmm*10^-3;      % Diameter of the specimen in [m]\quad
Lsmm=input('What is the length of the specimen in millimeters? ');
Ls=Lsmm*10^-3;     % Length of specimen in [m]
Aspec=pi*(Ds/2)^2; % Cross sectional area of the specimen in [m^2]

% BAR PARAMETERS
d = 0.7620;        % Distance from strain gauge to the sample [m]
Dbar=0.01905;     % Bar Diameter [m]
```

```

Abar=pi*(Dbar/2)^2; % Cross sectional area of the bar [m^2]
density = 1200;      % [kg/m^3]

% LOAD INCIDENT BAR PROPERTIES
[fname, fpathProperties]=uigetfile('*.txt','Select Incident Bar Gamma Function');
incidentBarGamma=load([fpathProperties fname]);
igFreq=fftshift(incidentBarGamma(:,1));
igAlpha=fftshift(incidentBarGamma(:,2));
igKappa=fftshift(incidentBarGamma(:,3));
igGamma=(complex(igAlpha,igKappa));

iPosTransferFunctionH=(exp(igGamma*d));
iNegTransferFunctionH=(exp(-igGamma*d));
igGamma2=ifftshift(igGamma.^2);
iw=ifftshift(2*pi*igFreq);
iw2=ifftshift((2*pi*igFreq).^2);
iEstar=-density*iw2./igGamma2;
V1Coef=-i*iw./ifftshift(igGamma);

% LOAD TRANSMISSION BAR PROPERTIES
[fname, fpathProperties]=uigetfile('*.txt','Select Transmission Bar Gamma
Function'); % Loads gamma for the transmission bar
transmissionBarGamma=load([fpathProperties fname]);
tgFreq=fftshift(transmissionBarGamma(:,1));
tgAlpha=fftshift(transmissionBarGamma(:,2));
tgKappa=fftshift(transmissionBarGamma(:,3));
tgGamma=(complex(tgAlpha,tgKappa));

tPosTransferFunctionH=(exp(tgGamma*d));
tgGamma2=ifftshift(tgGamma.^2);

```

```

tw=ifftshift(2*pi*tgFreq);
tw2=ifftshift((2*pi*tgFreq).^2);
tEstar=-density*tw2./tgGamma2;
V2Coef=-i*tw./ifftshift(tgGamma);

% PARAMETERS FOR ZEROING THE PULSES
inciLeading=150;    % Number of initial points used to calculate incident
baseline
transLeading=1000; % Number of initial points used to calculate transmission
baseline
inciSlope=0.5;    % Location of reference point on incident slope, as a
fraction of signal minimum
reflSlope=0.5;    % Location of reference point on reflected slope, as a
fraction of signal maximum
transSlope=0.5;   % Location of reference point on transmission slope, as a
fraction of signal minimum
percentTrigger=0.01;% Percent deviation from zero that signals the start of a
pulse

% SIGNAL PROCESSING PARAMETERS
conditionerRange = 50000; % Frequency range of the data acquisition hardware
signalSize = 2^13;      % Size of signal after padding

% CAPTURING INCIDENT AND REFLECTED PULSES
[fname, fpath]=uigetfile('*.asc','Select Incident Bar Signal'); % Read the
incident bar pulses; the data is time (seconds) vs. strain (in volts!)
cd(fpath)
channel1=load([fpath fname]);
tim=channel1(:,1);
dt=(tim(end)-tim(1))/(length(tim)-1); % dt is the time interval between

```

```

points in seconds
tim=tim*10^6; % Changes time from seconds to microseconds
tim=tim-tim(1); % Zero the time
EPS=channel1(:,2);

figure('name','Incident Bar Characterization Frequencies')
plot(igFreq)
title('Incident Bar Characterization Frequencies')
xlabel('Index')
ylabel('Frequency [Hz]')
print -dbmp16m Incident_Bar_Characterization_Frequencies

figure('name','Incident Bar Omega Squared')
plot(iw2)
title('Incident Bar Omega Squared')
xlabel('Index')
ylabel('Incident Bar Omega Squared [rad^2]')
print -dbmp16m Incident_Bar_Omega_Squared

figure('name','Incident Bar Alpha')
plot(igFreq,igAlpha)
title('Incident Bar Alpha')
xlabel('Frequency [Hz]')
ylabel('Incident Bar Alpha')
print -dbmp16m Incident_Bar_Alpha

figure('name','Incident Bar Phase Speed')
plot(igFreq, 2*pi*igFreq./igKappa)
title('Incident Bar Wave Speed')
xlabel('Frequency [Hz]')

```



```

ylabel('Incident Bar Phase Speed')
print -dbmp16m Incident_Bar_Phase_Speed

figure('name','Transmission Bar Characterization Frequencies')
plot(tgFreq)
title('Transmission Bar Characterization Frequencies')
xlabel('Index')
ylabel('Frequency [Hz]')
print -dbmp16m Transmission_Bar_Characterization_Frequencies

figure('name','Transmission Bar Omega Squared')
plot(tw2)
title('Transmission Bar Omega Squared')
xlabel('Index')
ylabel('Transmission Bar Omega Squared [rad^2]')
print -dbmp16m Transmission_Bar_Omega_Squared

figure('name','Transmission Bar Alpha')
plot(tgFreq,tgAlpha)
title('Transmission Bar Alpha')
xlabel('Frequency [Hz]')
ylabel('Transmission Bar Alpha')
print -dbmp16m Transmission_Bar_Alpha

figure('name','Transmission Bar Phase Speed')
plot(tgFreq, 2*pi*tgFreq./tgKappa)
title('Transmission Bar Wave Speed')
xlabel('Frequency [Hz]')
ylabel('Transmission Bar Phase Speed')
print -dbmp16m Transmission_Bar_Phase_Speed

```

```

% INCIDENT BAR SIGNAL AND PULSE MARKERS
figure('name','Zeroed Incident Bar Signal')
hold on
title('Zeroed Incident Bar Signal');
xlabel('Test Time [microseconds]');
ylabel('Strain [volts]');

% Calculate incident pulse baseline, for zeroeing
flatBaseline=polyfit(tim(1:inciLeading),EPS(1:inciLeading),0); % Using
y = constant method
EPS=EPS-flatBaseline(1); % Zeros the strain
plot(tim,EPS)
plot(tim,0,'k') % Plots black baseline
plot(tim(inciLeading),0,'ko') % Places black 'o' marker at last point used
in calculating baseline (allows user to see if larger inciLeading should be
used)
print -dbmp16m Zeroed_Incident_Bar_Signal

% RESAMPLE INCIDENT BAR SIGNAL TO BE 5000 MICROSECONDS IN DURATION AND HAVE
"SIGNALSIZE" POINTS
cd(fpathProperties)
newdt=(5000E-6)/(signalSize-1);
newtim=transpose(0:newdt:5000E-6);
% ValAtTime function courtesy of C. Bacon:
newEPS=ValAtTime(EPS(1:dsearchn(tim,5000)),dt,newtim);
newtim=newtim*10^6; % Changes newtim to microseconds
cd(fpath)
tim=newtim;
EPS=newEPS;

```

```

figure('name','Resampled Incident Bar Signal with Pulse Markers')
hold on
plot(newtim,newEPS)
plot(newtim,0,'k')
title('Resampled Incident Bar Signal with Pulse Markers')
xlabel('Test Time [microseconds]');
ylabel('Strain [volts]');

% Locate reference point on incident slope
[minimum,centerIncidentIndex]=min(EPS);
plot(tim(centerIncidentIndex),minimum,'gv')
lim1=inciSlope*minimum;
ind=1;
while EPS(ind)>lim1
    ind=ind+1;
end
ipoint=ind;
plot(tim(ipoint),EPS(ipoint),'gv')
% Back up to find exact start of incident pulse
ind=ipoint;
while EPS(ind)<percentTrigger*minimum
    ind=ind-1;
end
startIncident=ind;
plot(tim(startIncident),EPS(startIncident),'gv')
% Move up to find finish of incident pulse
ind=ipoint;
while EPS(ind)<0
    ind=ind+1;
end

```

```

endIncident=ind;
plot(tim(endIncident),EPS(endIncident),'gv')

iTime=tim(startIncident:endIncident)-tim(startIncident);
onlyIncident=-EPS(startIncident:endIncident); % NOTE NEGATIVE SIGN: MAKES
COMPRESSION SIGNALS POSITIVE
incident=zeros(signalSize,1);
incident(startIncident:endIncident)=onlyIncident;

% Locate reference point on reflected slope
[maximum,centerReflectedIndex]=max(EPS);
plot(tim(centerReflectedIndex),maximum,'r^')
lim1=reflSlope*maximum;
ind=ipoint;
while EPS(ind)<lim1
    ind=ind+1;
end
rpoint=ind;
plot(tim(rpoint),EPS(rpoint),'r^')
% Back up to find the start of the reflected pulse
ind=rpoint;
while EPS(ind)>percentTrigger*maximum
    ind=ind-1;
end
startReflected=ind;
plot(tim(startReflected),EPS(startReflected),'r^')
% Move up to find finish of reflected pulse
%ind=rpoint;
%while EPS(ind)>0
%    ind=ind+1;

```

```

%end
%endReflected=ind;
% Manually input end of reflected pulse
disp('Choose the end point of the reflected pulse: ')
position=ginput(1);
endReflected=dsearchn(tim,position(1));
if endReflected>signalSize
    endReflected=signalSize;
end
plot(tim(endReflected),EPS(endReflected),'r^')

rTime=tim(startReflected:endReflected)-tim(startReflected);
onlyReflected=-EPS(startReflected:endReflected);    % NOTE NEGATIVE SIGN:
MAKES TENSILE SIGNAL NEGATIVE
reflected=zeros(signalSize,1);
reflected(startReflected:endReflected)=onlyReflected;

print -dbmp16m Resampled_Incident_Bar_Signal_with_Pulse_Markers

% CAPTURING TRANSMITTED PULSE
[fname, fpath]=uigetfile('*.asc','Select Transmission Bar Signal'); % Read the
transmission bar pulse; the data is time (seconds) vs. strain (in volts!)
channel2=load([fpath fname]);
timT=channel2(:,1);
dtT=(timT(end)-timT(1))/(length(timT)-1);    % dtT is the time interval between
points in seconds for the transmission bar
timT=timT*10^6;    % Changes time from seconds to microseconds
timT=timT-timT(1); % Zero the time
EPST=channel2(:,2);

```

```

% TRANSMISSION BAR SIGNAL AND PULSE MARKERS
figure('name','Zeroed Transmission Bar Signal')
hold on
title('Zeroed Transmission Bar Signal')
xlabel('Test Time [microseconds]')
ylabel('Strain [volts]')

% Calculate transmission pulse baseline, for zeroeing
flatBaselineT=polyfit(TIMT(1:transLeading),EPST(1:transLeading),0); % Using
y = constant method
EPST=EPST-flatBaselineT(1); % Zeros the strain
plot(TIMT,EPST)
plot(TIMT,0,'k') % Plots black baseline
plot(TIMT(transLeading),0,'ko') % Places black 'o' marker at last point used
in calculating baseline (allows user to see if larger transLeading should be used)

print -dbmp16m Zeroed_Transmission_Bar_Signal

% RESAMPLE TRANSMISSION BAR SIGNAL TO BE 5000 MICROSECONDS IN DURATION AND HAVE
"SIGNALSIZE" POINTS
cd(fpathProperties)
newdtT=(5000E-6)/(signalSize-1);
newtimT=transpose(0:newdtT:5000E-6);
% ValAtTime function courtesy of C. Bacon:
newEPST=ValAtTime(EPST(1:dsearchn(TIMT,5000)),dtT,newtimT);
newtimT=newtimT*10^6; % Changes newtim to microseconds
cd(fpath)
TIMT=newtimT;
EPST=newEPST;
figure('name','Resampled Transmission Bar Signal with Pulse Markers')

```

```

hold on
plot(newtimT,newEPST)
plot(newtimT,0,'k')
title('Resampled Transmission Bar Signal with Pulse Markers')
xlabel('Test Time [microseconds]')
ylabel('Strain [volts]')

% Locate reference point on transmission slope
[minimumT,centerTransmissionIndex]=min(EPST);
plot(timT(centerTransmissionIndex),minimumT,'cv')
lim2=transSlope*minimumT;
ind=1;
while EPST(ind)>lim2
    ind=ind+1;
end
tpoint=ind;
plot(timT(tpoint),EPST(tpoint),'cv')
% Back up to find exact start of transmission pulse
ind=tpoint;
while EPST(ind)<percentTrigger*minimumT
    ind=ind-1;
end
startTransmission=ind;
plot(timT(startTransmission),EPST(startTransmission),'cv')
% Move up to find finish of transmission pulse
ind=tpoint;
while EPST(ind)<0 & ind<signalSize
    ind=ind+1;
end
endTransmission=ind;

```

```

plot(timT(endTransmission),EPST(endTransmission),'cv')

tTime=timT(startTransmission:endTransmission)-timT(startTransmission);
onlyTransmission=-EPST(startTransmission:endTransmission); % NOTE NEGATIVE
SIGN: MAKES COMPRESSION SIGNALS POSITIVE
transmission=zeros(signalSize,1);
transmission(startTransmission:endTransmission)=onlyTransmission;

print -dbmp16m Resampled_Transmission_Bar_Signal_with_Pulse_Markers

% PULSE OVERLAYS
figure('name','Unshifted Pulse Overlays')
hold on
plot(tim,incident,'g')
plot(tim,reflected,'r')
plot(timT,transmission,'c')
plot(timT,0,'k')
title('Unshifted Pulse Overlays');
xlabel('Time [microseconds]');
ylabel('Strain [volts]');
legend('Incident Pulse','Reflected Pulse','Transmission Pulse','location','best')
print -dbmp16m Unshifted_Pulse_Overlays

figure('name','Shifted Pulse Overlays')
hold on
plot(iTime,onlyIncident,'g')
plot(rTime,-onlyReflected,'r')
plot(tTime,onlyTransmission,'c')
plot(timT,0,'k')
title('Shifted Pulse Overlays');

```



```

xlabel('Time [microseconds]');
ylabel('Strain [volts]');
legend('Incident Pulse','Reflected Pulse','Transmission Pulse','location','best')
print -dbmp16m Shifted_Pulse_Overlays

% CONVERTING TO STRAIN FROM VOLTS
calibrationValue_incident=0.37471*10^(-3); % 1V = _____ strain (if 1000
microstrain, its 1e-3)
bridgeType=1; % if half-bridge, put 0.5: must
divide the strain by 2. quarter-bridge, put 1
calibrationValue_transmit=0.37471*10^(-3); % 1V = _____ strain (if 1000
microstrain, its 1e-3)

scalingFactor_incident=calibrationValue_incident*bridgeType;
scalingFactor_transmit=calibrationValue_transmit*bridgeType;

Ei=incident*scalingFactor_incident;
Er=reflected*scalingFactor_incident;
Et=transmission*scalingFactor_transmit;

% FOURIER TRANSFORM OF INCIDENT SIGNAL
figure('name','Incident Transform')
IFourier=fft(Ei);
iFourier=fftshift(fft(incident));
Npts=length(iFourier);
% Handling folding frequency based on C. Bacon's fftfrequencies.m
Nshanon=ceil(Npts/2);
T=(tim(end)-tim(1))*10^-6;
df=1/T;
for q=1:Nshanon

```

```

\quad freq(q,1)=(q-1)*df;
end
for q=Nshanon+1:Npts
\quad freq(q,1)=(q-1-Npts)*df;
end
freq=fftshift(freq);
iFreq=freq(find(freq>=0));
iFourier=iFourier(find(freq>=0));
iPower=abs(iFourier).^2;
plot(iFreq,iPower)
title('Frequency Spectrum of the Incident Signal');
xlabel('Frequency (Hz)');
ylabel('Power Index');
axis([0 conditionerRange/2 0 1E4]);
print -dbmp16m Incident_Transform

freqz=iFreq;

% FOURIER TRANSFORM OF REFLECTED SIGNAL
figure('name','Reflected Transform')
RFourier=fft(Er);
rFourier=fftshift(fft(reflected));
rFreq=freq(find(freq>=0));
rFourier=rFourier(find(freq>=0));
rPower=abs(rFourier).^2;
plot(rFreq,rPower)
title('Frequency Spectrum of the Reflected Signal');
xlabel('Frequency (Hz)');
ylabel('Power Index');
axis([0 conditionerRange/2 0 1E4]);

```

```

print -dbmp16m Reflected_Transform

% FOURIER TRANSFORM OF TRANSMISSION SIGNAL
figure('name','Transmission Transform')
TFourier=fft(Et);
tFourier=fftshift(fft(transmission));
tFreq=freq(find(freq>=0)); % freq is the same for transmission signal because
signals are the same size and period is the same size
tFourier=tFourier(find(freq>=0));
tPower=abs(tFourier).^2;
plot(tFreq,tPower)
title('Frequency Spectrum of the Transmission Signal');
xlabel('Frequency (Hz)');
ylabel('Power Index');
axis([0 conditionerRange/2 0 1E4]);
print -dbmp16m Transmission_Transform

iA=fftshift(IFourier).*iNegTransferFunctionH;
iB=fftshift(RFourier).*iPosTransferFunctionH;
iSum=(iA+iB);
F1Fourier=Abar*iEstar.*iSum;
iDiff=(iA-iB);
V1Fourier=V1Coef.*iDiff;

tSum=fftshift(TFourier).*tPosTransferFunctionH;
tDiff=tSum;
F2Fourier=Abar*tEstar.*tSum;
V2Fourier=V2Coef.*tDiff;

% CALCULATE SURFACE FORCES [MPA]

```

```

F1=ifft(iffshift(F1Fourier));
F2=ifft(iffshift(F2Fourier));

V1=-ifft(iffshift(V1Fourier));
V2=-ifft(iffshift(V2Fourier));

figure('name','Forces on Specimen Faces')
hold on
plot(tim,F1,'b')
plot(timT,F2,'r')
title('Forces on the Specimen''s Faces')
xlabel('Time [microseconds]')
ylabel ('Force [N]')
legend('Front Face','Rear Face','location','best')
print -dbmp16m Forces_on_Specimen_Faces

% Find force balance reference
disp('Indicate approximately where force balance begins (This point will be
used future plots as a reference): ')
position2=ginput(1);
forceRef=dsearchn(tim,position2(1));
% Shorten analysis duration to reduce noise at end of stress vs. strain curve
disp('Indicate where force balance ends (This will be the time up to which
stress and strain are calculated): ')
position3=ginput(1);
endAnalysis=dsearchn(tim,position3(1));

figure('name','Velocities of Specimen Faces')
hold on

```

```

plot(tim,V1,'b')
plot(timT,V2,'r')
title('Velocities of the Specimen''s Faces')
xlabel('Time [microseconds]')
ylabel('Velocity [m/s]')
legend('Front Face','Rear Face','location','best')
plot(tim(forceRef),(V1(forceRef)),'bo')
plot(timT(forceRef),(V2(forceRef)),'ro')
print -dbmp16m Velocities_of_Specimen_Faces

% CALCULATE STRAINRATE, STRAIN, AND STRESS
strainRate=(V1-V2)/Ls;
strain=cumtrapz(V1-V2)*dt/Ls;
stress=(F1+F2)/(2*Aspec*10^6); % in MPa

% CALCULATE/APPROXIMATE TRUE VALUES
trueStrain=log(1+strain);
trueStrainRate=zeros(signalSize,1);
for index = 2:signalSize
    trueStrainRate(index,1)=(trueStrain(index)-trueStrain(index-1))/dt;
end
trueStressApproximation=stress.*(ones(signalSize,1)+(strain));

figure('name','Strain')
hold on
plot(tim(1:endAnalysis),strain(1:endAnalysis))
plot(tim(1:endAnalysis),trueStrain(1:endAnalysis),'r')
plot(tim(forceRef),(strain(forceRef)),'bo')
plot(timT(forceRef),(trueStrain(forceRef)),'ro')

```

```

title('Strain')
xlabel('Time [microseconds]')
ylabel('Strain')
legend('Engineering Strain','True Strain','location','best')
print -dbmp16m Strain

figure('name','Strain Rate')
hold on
plot(TIM(1:ENDANALYSIS),STRAINRATE(1:ENDANALYSIS))
plot(TIM(1:ENDANALYSIS),TRUESTRAINRATE(1:ENDANALYSIS),'r')
plot(TIM(FORCEREf),(STRAINRATE(FORCEREf)),'bo')
plot(TIMT(FORCEREf),(TRUESTRAINRATE(FORCEREf)),'ro')
title('Strain Rate')
xlabel('Time [microseconds]')
ylabel('Strain Rate [1/s]')
legend('Engineering Strain Rate','True Strain Rate','location','best')
print -dbmp16m Strain_Rate

figure('name','Stress')
hold on
plot(TIM(1:ENDANALYSIS),STRESS(1:ENDANALYSIS))
plot(TIM(1:ENDANALYSIS),TRUESTRESSAPPROXIMATION(1:ENDANALYSIS),'r')
plot(TIM(FORCEREf),(STRESS(FORCEREf)),'bo')
plot(TIMT(FORCEREf),(TRUESTRESSAPPROXIMATION(FORCEREf)),'ro')
title('Stress')
xlabel('Time [microseconds]')
ylabel('Stress [MPa]')
legend('Engineering Stress','Approximated True Stress','location','best')
print -dbmp16m Stress

```

```

figure('name','Engineering Stress vs. Engineering Strain')
hold on
plot(strain(1:endAnalysis),stress(1:endAnalysis))
plot(strain(forceRef),(stress(forceRef)),'bo')
title('Engineering Stress vs. Engineering Strain')
xlabel('Engineering Strain')
ylabel('Engineering Stress [MPa]')
print -dbmp16m Engineering_Stress_Vs_Engineering_Strain

figure('name','Approximated Stress vs. True Strain')
hold on
plot(trueStrain(1:endAnalysis),trueStressApproximation(1:endAnalysis))
plot(trueStrain(forceRef),(trueStressApproximation(forceRef)),'bo')
title('Approximated True Stress vs. True Strain')
xlabel('True Strain')
ylabel('Approximated True Stress [MPa]')
print -dbmp16m Approximated_True_Stress_Vs_True_Strain

% Create .txt files in work folder containing the results
stressStrain = [strain(1:endAnalysis) strainRate(1:endAnalysis)
stress(1:endAnalysis) trueStrain(1:endAnalysis) trueStrainRate(1:endAnalysis)
trueStressApproximation(1:endAnalysis)];
save PMMAresults.txt stressStrain -ASCII -TABS

```





## Appendix G

# Functions Furnished by C. Bacon

### G.1 ValAtTime.m

```
function y=ValAtTime(Y,dt,t)
% \quad y=ValAtTime(Y,dt,t) determines the value of signal Y at time t.
% \quad dt is the sample time
NbrePts=length(Y);
y=zeros(size(t));
for j=1:length(t)
i=floor(t(j)/dt)+1;
if i<1
y(j)=0;
elseif t(j)==(NbrePts-1)*dt
y(j)=Y(NbrePts);
elseif i>=NbrePts
y(j)=0;
else
y(j)=Y(i)+(Y(i+1)-Y(i))/dt*(t(j)-(i-1)*dt);
end
end
```

## G.2 MakeEven.m

```
function y2=MakeEven(y1)
N=length(y1);
y2=y1;
y2(N+1)=y1(N);
y2(N+2:2*N)=y1(N:-1:2);
```

## G.3 MakeOdd.m

```
function y2=MakeOdd(y1)
N=length(y1);
y2=y1;
y2(N+1)=-y1(N);
y2(N+2:2*N)=-y1(N:-1:2);
```

## Appendix H

# Finding a Benchmark Synthetic Material

Given the large variance of the mechanical properties found in biological materials, as well as the novelty of the SHPB testing techniques utilized in their study, it was deemed necessary to find a more consistent synthetic material as a base for comparison. In this thesis a polyurea (PU) blend was used because its impedance was such that it could be studied on the PMMA SHPB as well as the hollow and solid aluminum SHPB set-ups. Unfortunately, this material, while convenient for validating the various SHPB testing techniques, does not accurately model the behavior or characteristics of any particular human tissues. As described in the introduction, one of the major goals of ISN Project 6.9 is to identify and characterize a wide range of suitable tissue simulants. Ideally, this Benchmark Synthetic Material (BSM) would be stable, exhibit minimal temperature dependence, and have a composition that could be varied in such a way as to synthesize its properties to approximately match those of various classes and types of biological tissue.

Currently, most ballistic evaluation techniques, including those of assessing armor solutions, are conducted utilizing a synthetic material known as Ordinance 250A Ballistic Gelatin. This material is little more than a denatured collagen gel, but has been the standard for comparison for decades. As we move towards the characterization of ever softer materials at high strain rates, understanding of the behavior of this ballistic gelatin is paramount to linking future

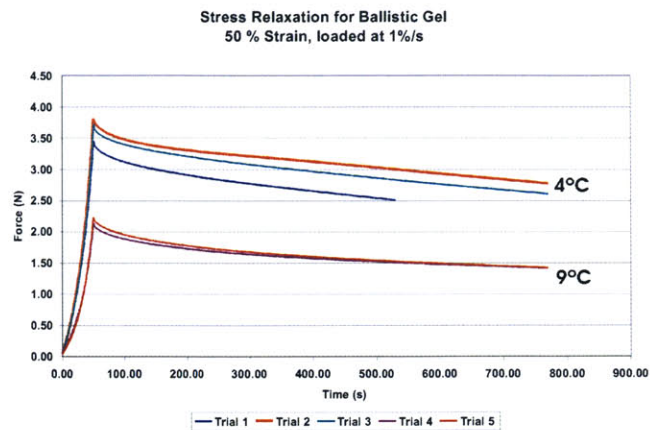


Figure H-1: Ordinance 250A Ballistic Gelatine, the current industry standard, is highly temperature dependent.

findings to previous studies. Through a series of low rate tests on our Zwick testing apparatus, however, it has already been determined that this material is extremely temperature dependent (Figure H-1). As such, while it is important to understand its high rate behavior, future ballistic protection studies should instead be conducted utilizing more stable, and hopefully more biofidelic, materials.

Work is currently underway to identify potential substitutes. Preliminary data seems to indicate that a two part GE silicon gel called RTV 6166 may provide the solution. The material is very stable, shows almost no temperature dependence, and its properties can be easily tailored by adjusting the ratio of its constituent parts. Other potential BSMs include various hydrated felts and open cell foams, as well as an oriented blend of Styrene-Isoprene-Styrene triblock copolymer mixed with varying amounts of mineral oil.

Rheometry, dynamic-mechanical analysis (DMA), and quasi-static tests are all currently underway to characterize these new simulants and assess each as a potential replacement for Ordinance 250A Ballistic Gelatin in future tests. Work is also being done to characterize these extremely soft materials at the high strain rates seen in this study for trabecular bone. Unfortunately, however, these new materials are still many times softer than our current limits of testing and work must be done to further increase the sensitivity of the SHPB technique (Figure H-2).

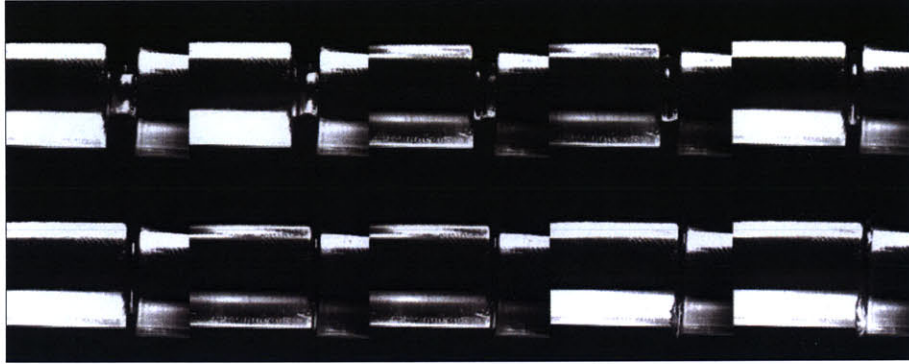


Figure H-2: Seen here during a low pressure PMMA SHPB trial, the potential tissue simulant RTV 6166 is too soft to accurately characterize with the current techniques.



# Appendix I

## Model Validation with Gas Gun Trials

Once the constitutive models for human tissues have been refined, and biofidelic BSMs have been identified, some form of experimental verification will be necessary to make sure that the models are able to accurately predict the complex interactions between the armor system and its wearer. Development of a technique to achieve this verification at the ISN gas gun facility was part of my initial Master's thesis work. The devised approach allows us to impact a large block of tissue simulant protected the armor system of interest. The tissue simulant is positioned directly behind the armor (Figure I-1) and is held in place by a clear support clamp developed during the course of this thesis (Figures I-2 through I-6). This set-up allows for high speed photography of the impact and resulting strain waves (Fig. I-7). To measure these waves, the plane of impact within the gel is imbedded with numerous tracking particles. Utilizing image correlation software from Correlated Solutions, we are then able to track the motion of these imbedded beads and calculate the resulting strain waves as they propagate through the simulant (Figure I-8). By comparing the speed and magnitude of these propagating waves to the finite element simulations of the same impact scenario, we will obtain an excellent understanding of how accurate the models' predictions are.

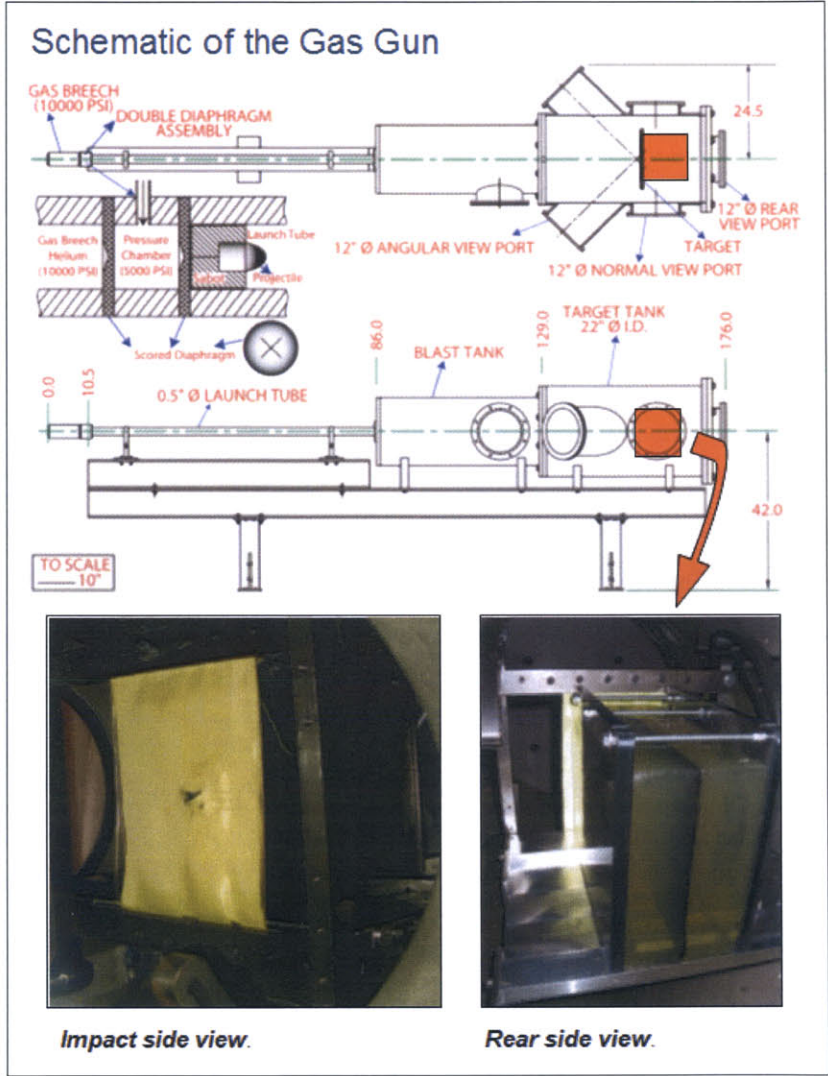


Figure I-1: Schematic representation of the gas gun facility used to evaluate the accuracy of predictions made by the computational models.



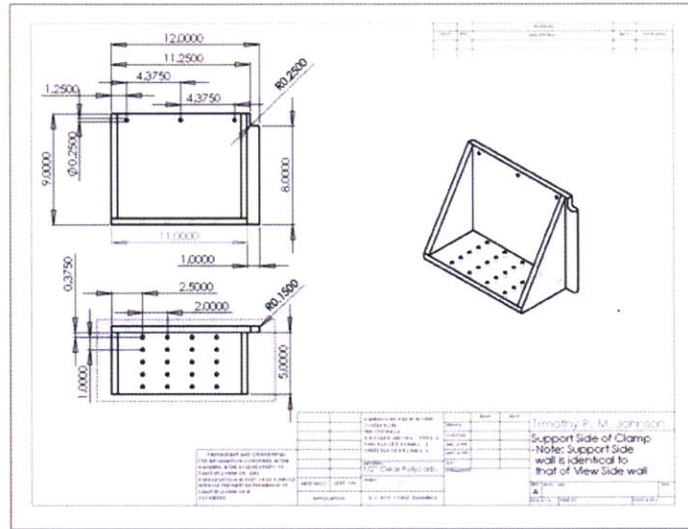


Figure I-2: CAD drawing of the gel clamp's support side.

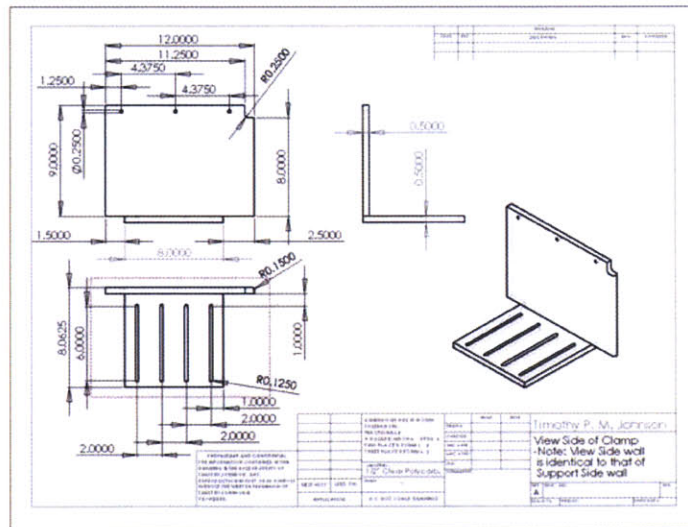


Figure I-3: CAD drawing of the gel clamp's view side.

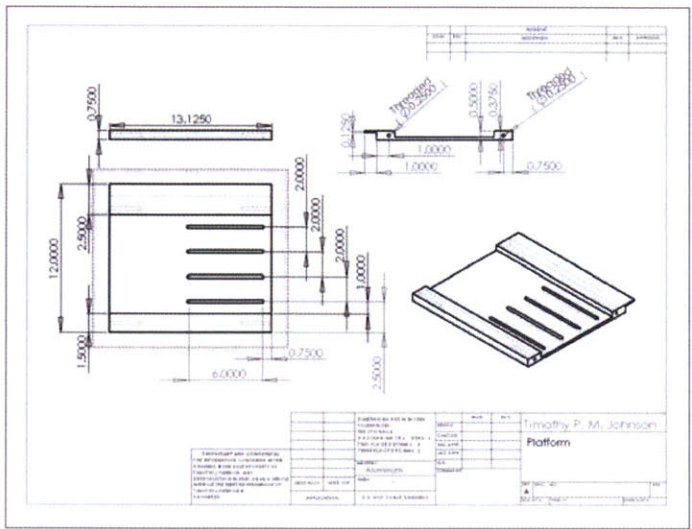


Figure I-4: CAD drawing of the gel clamp's platform.

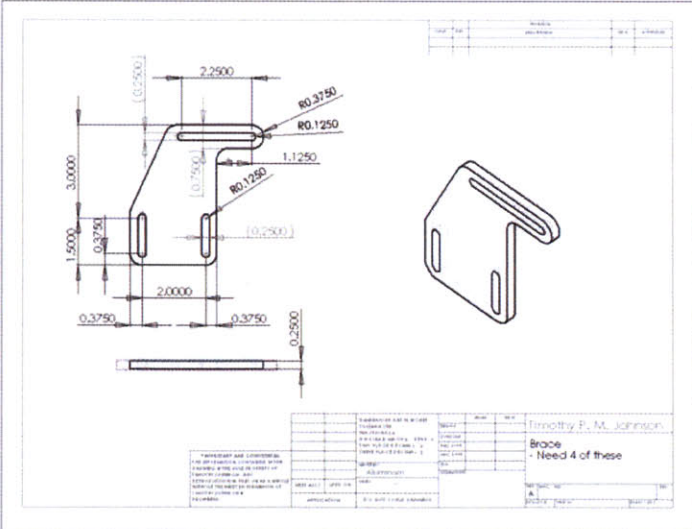


Figure I-5: CAD drawing of the gel clamp's supports.

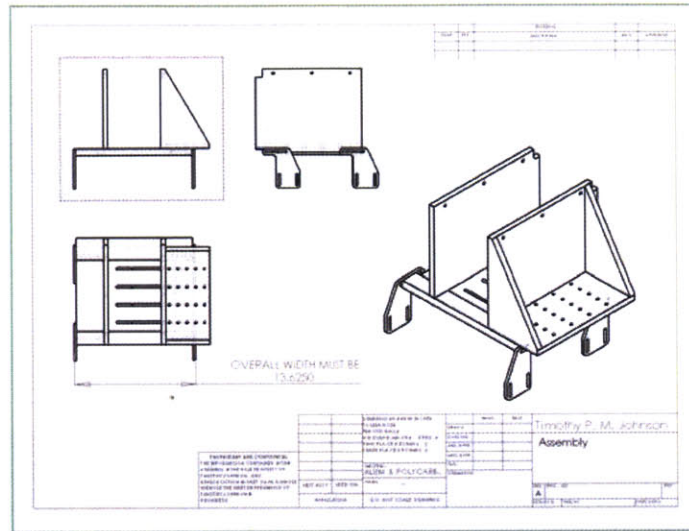


Figure I-6: CAD drawing of the assembled gel clamp.

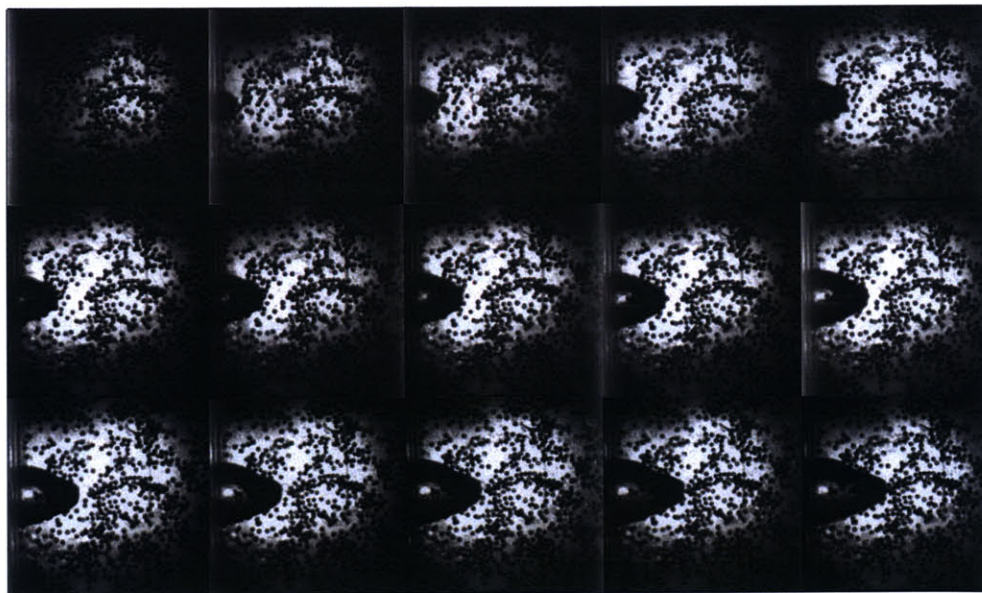
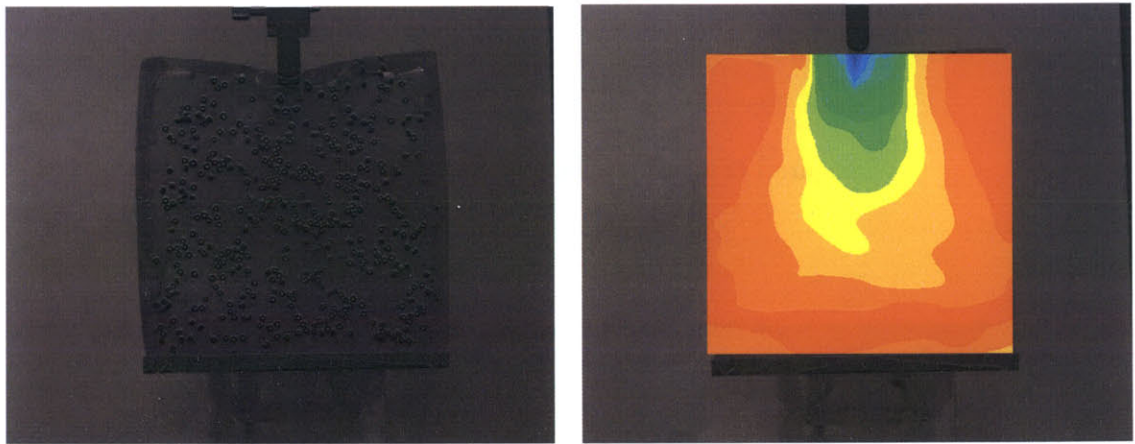


Figure I-7: Penetration of Ordnance 250A Ballistic Gellatin block with a 1/2" diameter polycarbonate projectile fired at approximately 500 m/s.



(a) Original image acquired during the mechanical testing.

(b) Graphical representation of the calculated strain field.

Figure I-8: Example of the image correlation technique applied a low rate mechanical test of Ordinance 250A Ballistic Gelatin.

# Bibliography

- [1] R. B. Ashman and J. Y. Rho. Elastic modulus of trabecular bone material. *Journal of Biomechanics*, 21(3):177–181, 1988.
- [2] J. S. Bensusan, D. T. Davy, K. G. Heiple, and P. J. Verdin. *19th Annual Orthopaedic Research Society Meeting*, 8:132, 1983.
- [3] D. R. Carter and W. C. Hayes. Bone compressive strength: The influence of density and strain rate. *Science*, 194(4270):1174–1176, December 1976.
- [4] D. R. Carter and W. C. Hayes. The compressive behavior of bone as a two-phase porous material. *Bone Joint Surg.*, 59:954–962, 1977.
- [5] D. R. Carter, G. H. Schwab, and D. M. Spengler. Tensile fracture of cancellous bone. *Acta Orthopaed. Scand.*, 51:733–741, 1980.
- [6] D. R. Carter and D. M. Spengler. Mechanical properties and composition of cortical bone. *Clin. Orthop. Rel. Res.*, 135:192–217, 1978.
- [7] W. Chen, B. Zhang, and M. J. Forrestal. A split hopkinson bar technique for low-impedance materials. *Experimental Mechanics*, 39(2):81–85, June 1999.
- [8] K. Choi, J. L. Kuhn, M. J. Ciarelli, and S. A. Goldstein. The elastic modulus of human subchondral trabecular and cortical bone tissue and the size dependence of cortical bone modulus. *Journal of Biomechanics*, 23:1103–1113, 1990.
- [9] H. D. Currey. *The Mechanical Adaptations of Bones*. Princeton University Press, Princeton, NJ, 1984.

- [10] J. D. Currey. The mechanical properties of bone. *Clin. Orthop. Rel. Res.*, 73:210–231, 1970.
- [11] E. Davies and S. Hunter. The dynamic compression testing of solids by the method of split hopkinson pressure bar. *Journal of the Mechanics and Physics of Solids*, 11:155–179, 1963.
- [12] R. M. Davies. A critical study of the hopkinson pressure bar. *Philisophical Transactions of the Royal Society of London. Series A, Mathematical and Physical Sciences*, 420(281):375–457, January 1948.
- [13] J. F. Doyle. *Wave Propagation in Structures*. Springer-Verlag, New York, 1989.
- [14] L. J. Gibson. The mechanical behaviour of cancellous bone. *Journal of Biomechanics*, 18:317–328, 1985.
- [15] L. J. Gibson and M. F. Ashby. *Cellular Solids: Structure and properties*. Cambride Solid State Science Series. Cambridge University Press, second edition, 1997.
- [16] T. P. Harrigan, M. Jasty, R. W. Mann, and W. H. Harris. Limitations on the continuity assumption in cancellous bone mechanics. In *Transactions of the 31st Annual Meeting of the Orthopedic Research Society*, page 353. Orthopedic Research Society, Chicago, 1985.
- [17] W. C. Hayes and D. R. Carter. Post-yield behavior of subchondral trabecular bone. *J. Biomed. Mat. Res.*, 7(537-544), 1976.
- [18] B. Hopkinson. A method of measuring the pressure produced in the detonation of high explosives or by the impact of bullets. *Philosophical Transactions of the Royal Society of London, Series A*, 213:437–456, 1914.
- [19] I. Hvid, S. M. Bentzen, F. Linde, L. Mosekilde, and B. Pongsoipetch. X-ray quantitative computed tomography: The relations to physical properties of proximal tibial trabecular bone specimens. *Journal of Biomechanics*, 22:837–844, 1989.
- [20] G. T. Gray III. *Sample Design and Preparation*, volume 8, chapter Classic Split-Hopkinson Pressure Bar Testing. ASM International, 2003.

- [21] T. S. Keller and M. Liebschner. *Mechanical Testing of Bone and the Bone Implant Interface*, chapter Tensile and Compressive Testing of Bone, pages 175–206. CRC Press, Boca Raton, FL, 1999.
- [22] H. Kolsky. An investigation of the mechanical properties of materials at very high rates of loading. *Proceedings of the Physical Society, Section B*, 62:676–700, 1949.
- [23] F. Linde, P. Norgaard, I. Hvid, A. Odgaard, and K. Soballe. Mechanical properties of trabecular bone: Dependency on strain rate. *Journal of Biomechanics*, 24(9):803–809, 1991.
- [24] J. H. McElhaney. Dynamic response of bone and muscle tissue. *Journal of Applied Physiology*, 21(4):1231–1236, July 1966.
- [25] E. F. Morgan, H. H. Bayraktar, and T. M. Keaveny. Trabecular bone modulus-density relationships depend on anatomical site. *Journal of Biomechanics*, 36(7):897–904, July 2003.
- [26] A. D. Mulliken. Low to high strain rate deformation of amorphous polymers: Experiments and modeling. Master’s thesis, Massachusetts Institute of Technology, June 2004.
- [27] D. T. Reilly and A. H. Burnstein. The mechanical properties of cortical bone. *Journal of Bone Joint Surgery*, 56:1001–1022, July 1974.
- [28] D. T. Reilly and A. H. Burnstein. The elastic and ultimate properties of compact bone tissue. *Journal of Biomechanics*, 8:393–396, 1975.
- [29] S. D. Ryan and J. L. Williams. Tensile testing of rodlike trabeculae excised from bovine femoral bone. *Journal of Biomechanics*, 22:351–355, 1989.
- [30] D. W. Thompson. *On Growth and Form*. Cambridge University Press, Cambridge, UK, 1961.
- [31] P. R. Townsend, R. M. Rose, and E. L. Radin. Buckling studies of single human trabeculae. *Journal of Biomechanics*, 8:199–201, 1975.

- [32] J. L. Williams and J. L. Lewis. Properties and an anisotropic model of cancellous bone from the proximal tibial epiphysis. *Journal of Biomechanics*, 104:50–56, 1982.
- [33] J. Wolff. Über die beneutung der architectur der spongiosen substanz für die frage vom knochenwachsthum. *Zentralblatt für die Medizinische Wissenschaft*, IV:223–234, 1869.
- [34] J. Yi, M. C. Boyce, G. F. Lee, and E. Balizer. Large deformation rate-dependent stress-strain behavior of polyurea and polyurethanes. *Polymer*, August 2005. Submitted.
- [35] P. K. Zysset, R. W. Goulet, and S. J. Hollister. A global relationship between trabecular bone morphology and homogenized elastic properties. *Journal of Biomechanical Engineering*, 120:640–646, 1998.